Integrated Devices for On-Chip Quantum Optics

by

Clinton Alexander Potts

A thesis submitted in partial fulfillment of the requirements for the degree of

Master of Science

Photonics and Plasmas

Department of Electrical and Computer Engineering

University of Alberta

Abstract

This thesis describes the fabrication and characterization of on-chip dome-shaped, Fabry-Perot microcavities for quantum-optics applications. Arrays of cavities were fabricated via a guided delamination buckling self-assembly process within SiO_2/Ta_2O_5 multilayers. This process results in highly symmetric cavities, which exhibit minimal geometrical defects and a morphology that is well-described by elastic buckling theory. Optical measurements revealed reflection-limited finesse of ~ 3500, suggesting these cavities have few defects and exhibit low surface roughness. Furthermore, these cavities preferentially supported Laguerre-Gaussian modes as a result of the high degree of cylindrical symmetry.

The viability of utilizing such cavities for cavity quantum electrodynamics applications was theoretically examined using the extracted parameters. As a result of the small mode volume, these cavities were predicted to exhibit an exceptionally high atom-cavity coupling rate, $g \approx 2\pi \times 1.1$ GHz. However, the strong-coupling parameter $g/\kappa \sim 0.2$ placed the as-fabricated cavities in the weakly coupled regime of cavity quantum electrodynamics. On the other hand, a single-atom cooperativity of ~ 30 was estimated, suggesting such cavities may be utilized to implement highly-efficient single-photon sources. Furthermore, the low mode-volume and potential for open-access suggests that these cavities have potential for diverse applications such as lab-on-chip sensing and implementation of dye-based lasers.

Acknowledgements

I would like to first thank my supervisors Dr. DeCorby and Dr. Davis for their endless support throughout my thesis. Your guidance was invaluable at every step during the course of my thesis, helping to develop the skills required for future success.

To Dr. LeBlanc and Dr. Maciejko, thank you for the countless hours of help, your office door was always open if I had questions.

To all the members of our lab groups, thank you for making it enjoyable to come in every day. Special thanks to Aaron Melnyk for his instruction on the fabrication process. Thanks to Mohammad Bitarafan for the countless hours spent with me sitting at the sputtering system. Thanks to Hugh Ramp for his endless assistance in the collection of data presented throughout this thesis. Finally, thank you to everyone else for your help over the past two years.

Thank you to all of the staff in the Nanofab, without your assistance this work would not have been possible.

To my family and friends, thank you for your endless support throughout my thesis. Your constant words of support were invaluable, and your kind words were greatly appreciated.

Finally, I would like to thank Natural Sciences and Engineering Research Council (NSERC), Alberta Innovates Technology Futures (AITF), and the University of Alberta for providing funding that made this work possible.

Contents

List of Tables

List of Figures

Chapter 1

Introduction

This thesis focuses on the development of an on-chip platform designed for quantum optics applications, but which might also have applications in diverse fields such as lab-on-a-chip sensing [1], dye-based lasers [2], and optofluidic systems [3]. The motivation for this work stems from a growing interest in utilizing the strangeness of quantum mechanics for practical applications, such as quantum computers and quantum communication networks. This chapter describes this motivation and explores recent advancements in quantum information sciences, focusing primarily on the field of cavity quantum electrodynamics.

1.1 Quantum Information Science

In the past decade, quantum science and technology has been a subject of great interest to the academic community, since it promises to revolutionize human understanding of the physical world [4, 5, 6, 7, 8]. Particular excitement has been directed towards the field of quantum information, which encompasses the fields of quantum computing and quantum communication.

Quantum computing indeed has the potential to cause a paradigm shift in our understanding of the natural world. This is due to the potential for the implementation

of quantum algorithms allowing previously unsolvable (in polynomial time) problems to be solved within realistic time scales. To date, D-Wave has successfully produced a quantum computer functioning via the process of quantum annealing [9, 10]. However, this computation scheme is limited in the scope of problems it is capable of solving, and has yet to show a significant speed advantage over classical algorithms [11]. The goal of many research groups is the development of a gate-based quantum computer with the capability of implementing any arbitrary quantum algorithm [4]. On an optimized quantum computer, well-known algorithms such as Shor's integer factorization algorithm [12, 13] or Grover's database search algorithm [14] could provide a significant increase in computing speed and power compared to their classical counterparts. Furthermore, being an inherently quantum system, a quantum computer has the potential to simulate complex many-body quantum systems; this could prove invaluable for biological and quantum chemistry research [15].

Quantum communication is the other well-known subsection of quantum information, focusing on the distribution of quantum information over large distances. The idea of a "quantum internet" [16] of distributed nodes connected via channels capable of sharing quantum information over large distances is a highly sought goal. Such a network would be vastly different than any classical network, exhibiting truly quantum properties such as entanglement between distant nodes. Furthermore, as the information is largely shared between nodes, the available state-space increases exponentially with the number of nodes, as opposed to linearly as in classical networks [17]. Individual small quantum networks could be connected, forming a single large computational unit. Such quantum connectivity also provides means to overcome scaling issues and error-correction problems that would limit the size of individual machines for quantum information processing [18]. An individual user could submit a private computation request to the large quantum network and utilize large remote quantum computers. Furthermore, the distribution of entanglement between distant

nodes would provide an unbreakable form of encryption for information sharing via quantum teleportation [19, 20] or quantum key distribution [21].

Unfortunately, the development of large scale quantum systems has been challenging. The main difficulty has been that individual quantum bits (qubits) must be largely decoupled from their environment to avoid decoherence. At the same time, deterministic, coherent, long-range interactions between qubits is required to efficiently scale to larger quantum systems. This trade-off has proven to be challenging, as these requirements are in a sense competing against each other. Despite these difficulties, quantum functionality has already been demonstrated in numerous systems [22, 23, 24, 25].

1.2 Current Quantum Systems

Diverse physical systems have been used to implement quantum information systems. Early demonstrations were performed using nuclear magnetic resonance systems [22], and trapped ion and neutral atoms in free space [23, 26]. More recently, there has been a large focus on superconducting circuits, such as the quantum annealing devices developed by D-Wave, or the numerous gate-based superconducting quantum systems [24, 27, 28]. Following this solid-state model, chip-based quantum systems utilizing spin states in quantum dots have also been studied [29]. Dopants such as phosphorous in silicon have demonstrated coherence times on the order of hours as a result of the weak interaction strength to their environment [25, 30]. See Figure 1.1 for some examples of these various systems.

While most of these applications have been focused on the development of a local single-chip quantum computer, the development of a distributed quantum network requires a system which satisfies the following criteria. First, the distribution of quantum information over long distances requires optical photons (preferably infrared

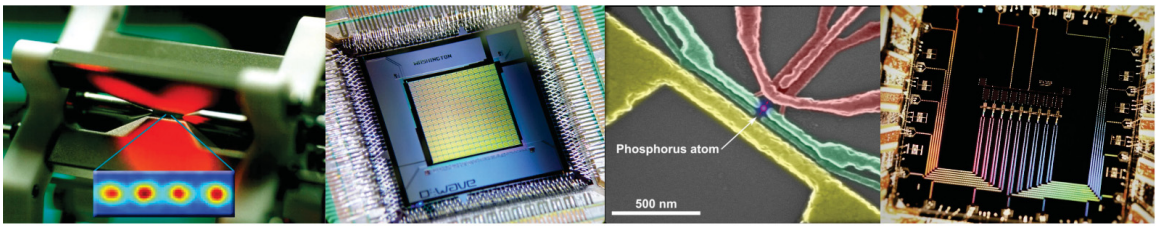

Figure 1.1: (a) Calcium ion trap utilized for the generation of entangled states, from [31]. (b) D-Wave's superconducting quantum computer, from [32], (c) Phosphorous qubit embedded within a silicon substrate, an early exploration of silicon based quantum computing technology, from [33]. (d) Quantum error correction circuit for superconducting gate based quantum computing, from [34].

photons) to allow distribution via existing telecommunication networks. Second, the individual quantum nodes must exhibit long-lived quantum states to avoid decoherence during the transit of photons between distant nodes. Third, the system needs to be robust to the loss of photons, since even the most efficient system will unfortunately suffer from some amount of photon loss. Finally, the interaction between the photon and the stationary node must be highly efficient to allow the deterministic transfer of quantum information between nodes in the system [17]. These requirements have motivated the use of single atoms trapped within high-finesse optical cavities as a hybrid quantum light-matter interface providing the nodes for a large distributed quantum network.

1.3 Quantum Electrodynamics in a Cavity

The canonical cavity quantum electrodynamics system consists of a single two-level atomic emitter trapped within a high-finesse Fabry-Perot cavity, as shown in Figure 1.2. As a result of the multiple passes that a photon within the cavity makes past the trapped atom, the interaction probability is greatly increased. Energy is transferred between the atom and the cavity at a rate $2g$, known as the vacuum Rabi

frequency. This system has several advantages over many other quantum interfaces for the development of a distributed quantum network. For example, single atoms may be well isolated from the environment and exhibit long-lived, well-defined quantum ground states [35]. Quantum information may be coherently transferred from the atom to a single photon, capable of being transported via optical fiber over great distances [36]. Furthermore, recent schemes have described a method in which infrared photons may be produced, allowing efficient transport down pre-existing fiber optic lines [37].

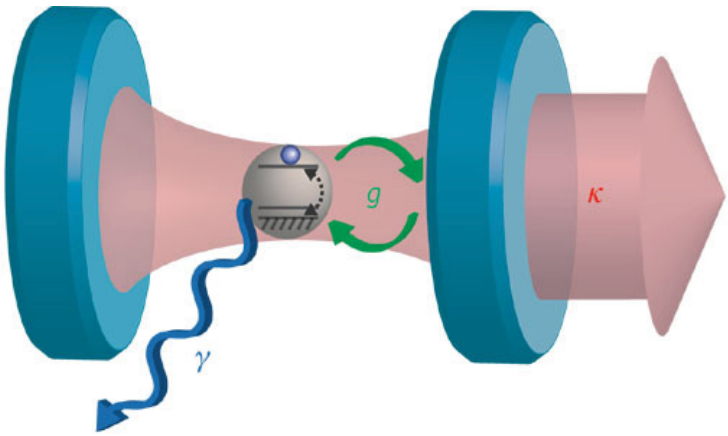

Figure 1.2: Canonical cavity quantum electrodynamics system, depicting the three governing field rates of the system. These include g (the atom-cavity coupling rate), κ (the cavity decay rate), and γ (the polarization decay rate of the atom), from [16].

Early demonstrations of cavity quantum electrodynamics involved cesium atoms falling through a macroscopic Fabry-Perot cavity [38, 39], and similar cavities are still used in many laboratories. Recent publications have developed fiber-based Fabry-Perot cavities [40], and microtoroid and bottle resonators have been utilized for coupling atoms to the evanescent field [41, 42]. Chip-based devices, including photonic crystals [43] and waveguides [44], allow the production of multiple devices on a single solid-state system. Examples of these different devices are shown in Figure 1.3.

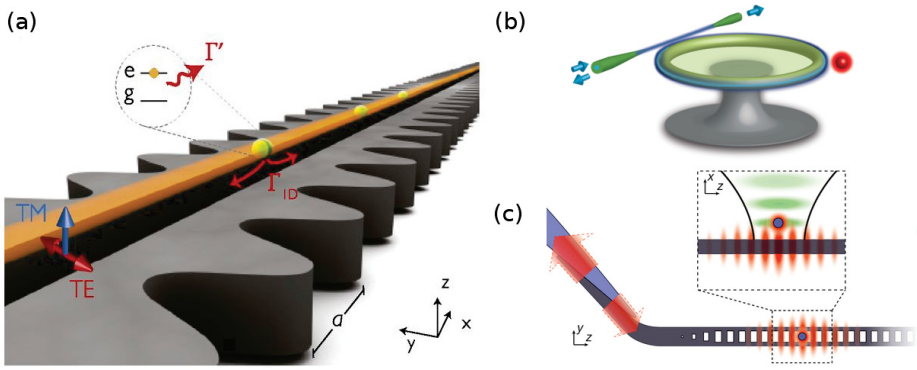

Figure 1.3: (a) Schematic of a waveguide cavity quantum electrodynamic systems; atoms (green spheres) are trapped within an optical dipole trap (orange cylinder), atoms are coupled to the fundamental TE waveguide mode, from [44]. (b) Schematic of a toroidal microresonators coupled to a single cesium atom, from [45]. (c) Schematic of a single rubidium atom trapped within a standing wave trap above a photonic crystal. Inset shows the standing wave dipole trap, from [43].

Since the observation of photon antibunching from the emission of sodium atoms [46] (arguably the earliest experimental observation of truly quantum behavior of light), many advances have been made in the field of cavity quantum electrodynamics. Some of the most notable include; the deterministic generation of single photons [47, 48], utilization of a single rubidum atom as a quantum memory [49], the coherent state transfer between an atom and a photon [36], the production of atom-photon and atom-atom entangled states [50], the demonstration of an elementary quantum network [51], and the implementation of a single photon quantum gate [52].

These early successes have motivated new research, with the eventual goal of a large scale distributed quantum network. Work demonstrating successful quantum teleportation over a municipal fiber line demonstrated difficulties that fluctuations in ambient conditions cause [53]. As a result of changing temperature and local fiber stress, the polarization slowly shifted throughout the day, such that constant feedback was required to correct this drift. Furthermore, current cavity setups are bulky and at most support a few cavities per optical setup. A true world-wide quantum network would require scaling to hundreds or thousands of devices per optical setup.

Work involving chip-based systems including waveguide quantum electrodynamics, has started to pursue this ambitions goal [54]. To that end, this thesis focuses on another potentially scalable solution, by utilizing a self-assembly procedure to produce many Fabry-Perot cavities on a single chip.

1.4 Current Fabry-Perot Cavities

As described above, Fabry-Perot cavities are the prototypical structure for cavity quantum electrodynamics. Thus, a focus in recent years has been on the development of new Fabry-Perot cavities suitable for this application [40, 55, 56]. These cavities should fulfill several key requirements. To facilitate the coupling of atomic species, open-access to the cavity mode is necessary. Furthermore, this open-access should allow the introduction of trapping fields such that atoms could be held stationary within the cavity mode. Moreover, the irreversible loss of photons must also be limited. Thus, cavities should exhibit high finesse, reducing the cavity decay rate κ. The mode-volume should be small in order to maximize the atom-cavity coupling rate g. These two rates should be comparable at minimum, and strong-coupling (i.e. $g > \kappa$) is highly sought. Finally, the cavity must be tunable to ensure the cavity may be brought into resonance with an atomic emitter. To fulfill all these requirements several approaches have been described in the literature.

The most commonly used Fabry-Perot cavities for cavity quantum electrodynamics are macroscopic cavities like the ones described in Ref. [57], shown in Figure 1.4a. These cavities have been shown to exhibit exceptionally high finesse ($\sim$ 500 000) and are easily tunable using piezo stages. Unfortunately, these cavities are relatively large, limiting the scalability to the large arrays of cavities needed for a global quantum-network [16]. Recently, fiber based cavities utilizing two mirrored fibers [40, 58, 60], or a single fiber and a planar mirror [61] have been demonstrated, as shown in Fig-

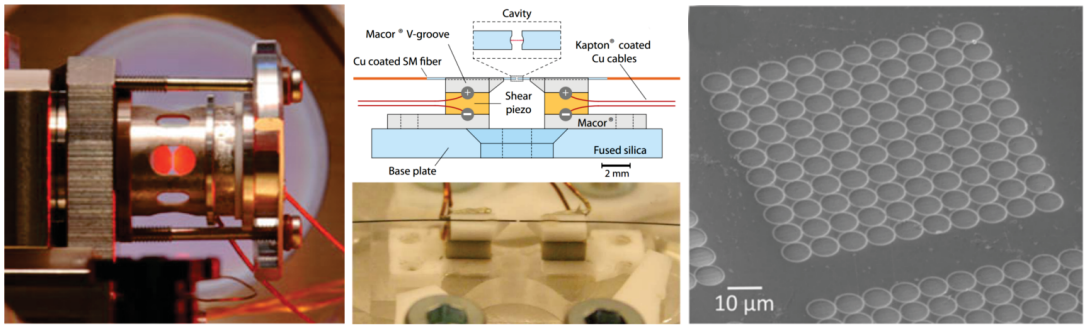

Figure 1.4: (a) Macroscopic Fabry-Perot cavity mounted within a stick slip piezo stage for fine adjustment of cavity length, mirrors are shown illuminated in red, similar to the cavity used in [57, 48]. (b) Fiber-based Fabry-Perot cavity, with additional alignment apparatus, from [58]. (c) Array of on-chip FIB-milled cavities, forming the bottom mirror of the Fabry-Perot cavities, from [59].

ure 1.4b. Similar to the macroscopic cavities, these have exhibited high finesse ($\sim$ 33 000 [58]) and open-access for trapping lasers and atomic delivery. Moreover, these cavities have estimated mode-volumes on the order of $\sim 10\lambda^3$ at a wavelength $\lambda = 780$ nm [40], among the smallest for Fabry-Perot cavities in the literature. However, in order to produce the concave end facets, CO_2 laser ablation is used in a device-by-device fashion. Following this, a pair of fibers must be carefully aligned, again in a device-by-device fashion. Despite being more compact than their macroscopic counterparts, this device-by-device alignment could prohibit scaling to more than a few cavities in a single chamber. A more scalable approach involves the use of FIB milling or CO_2 laser ablation of substrate material to produce arrays of on-chip cavities [59, 62]. Such designs have demonstrated cavity finesse on the order of $\sim$ 25 000, and provide open-access to the environment. Furthermore, as shown in Figure 1.4c, many cavities can be produced on a single chip. Unfortunately, as a result of the full wafer nature of these devices, individual tuning of cavities could prove to be difficult; a truly scalable design would require many devices on a single chip to be brought into resonance simultaneously.

This thesis describes a fully on-chip Fabry-Perot cavity fabricated using a novel guided delamination buckling procedure [63]. Devices were fabricated in a monolithic nature on a single substrate, removing the requirement of wafer-bonding or post-fabrication alignment. Furthermore, these Fabry-Perot cavities exhibit a high degree of cylindrical symmetry and low surface roughness, producing reflection limited finesse of ~ 3500 [64].

1.5 Summary of Thesis

This thesis describes work on guided delamination buckling of hollow-core Fabry-Perot microcavities, with operation wavelengths in the near-infrared regime. An experimental and theoretical exploration of these cavities was conducted, to assess their viability for applications in quantum information science, particularly cavity quantum electrodynamics. The chapter summaries are as follows:

Chapter 2 summarizes some of the theoretical background information related to this work, including Fabry-Perot cavities, and cavity quantum electrodynamics.

Chapter 3 describes the self-assembly fabrication technique, including the sputtering procedure. The morphology of the fabricated cavities is also explored. The second half of this chapter describes the optical results obtained for the fabricated microcavities.

Chapter 4 provides a theoretical exploration of the viability of utilizing such cavities for cavity quantum electrodynamics. Several simulations are presented to assess the expected behavior of atoms embedded in such devices. Furthermore, a discussion of potential means for introducing atoms into the cavity mode is provided.

Chapter 5 summarizes the work performed and provides some insight on possible future work.

Chapter 2

Theoretical Background

This chapter will provide the required theoretical background for the remaining chapters of this thesis. I will begin by describing buckled dome microcavities and the relevant theory of Fabry-Perot resonators. Next, a brief description of the theory of cavity quantum electrodynamics (CQED) will introduce the key concepts required for Chapter 4.

2.1 Fabry-Perot Microcavity

The work presented in this thesis focuses primarily on the fabrication and characterization of on-chip Fabry-Perot microcavities. These microcavities consist of two highly reflective mirrors (one planar, one curved) separated by an air gap, forming a half-symmetric optical resonator. Electromagnetic radiation which satisfies the resonance condition (the accumulation of a 2πn phase shift upon a round trip of the cavity, where n is a positive integer) is effectively stored within the cavity due to the repeated reflections off the mirrors. The ability to store electromagnetic radiation makes Fabry-Perot resonators a crucial optical element for many applications. As this storage effectively increases the interaction length, it allows the typically low interaction probabilities of freely propagating photons to be increased with every round

trip. The most notable application of this phenomena is the laser, where a single photon may excite the emission of many photons as it repeatedly traverses the optical cavity.

2.1.1 Distributed Bragg Reflectors

Mirrors are one of the most common of optical devices, used to change the propagation direction of light. Many mirrors are simply polished metallic surfaces such as aluminium or gold. Mirrors that utilize metallic surfaces exhibit high reflectance over a broad wavelength range and at nearly all incident angles. However, even a perfectly polished metal surface, (for example gold) can only provide a peak reflectance of $\sim 97\%$ over the wavelength range of $700 - 2000$ nm [65]. Despite this limited reflectance, gold-coated copper mirrors are often utilized with high-power CO_2 lasers, since substantial amounts of heat can be tolerated due to the high thermal conductivity of the metallic layers. Unfortunately, many applications require mirrors with higher reflectance and, crucially for cavity quantum electrodynamics, lower optical loss. In these situations, mirrors comprised of thin stacks of dielectric material are utilized. Such mirrors have demonstrated peak reflectance $> 99.999\%$ [66] and, due to their dielectric nature, exhibit much lower photon loss than their metallic counterparts.

Dielectric mirrors, also known as distributed Bragg reflectors, are constructed using alternating layers of high and low index materials. High reflectivity is achieved by designing the layer thicknesses such that all partially reflected rays constructively interfere at the mirror surface. Reflection at an interface between two media of index n_1 and n_2 is governed by the Fresnel equations. Assuming normal incidence and following the convention prescribed by Kasap [67], the field reflection and transmission coefficients may be expressed as:

$$r = \frac{n_1 - n_2}{n_1 + n_2}, \tag{2.1}$$

$$t = \frac{2n_1}{n_1 + n_2}. \tag{2.2}$$

Notice, upon reflection the phase shift depends on the relative difference between the index of the two media. A lower index incident medium (i.e. $n_1 < n_2$) implies a π phase shift, while a higher index incident medium implies no phase shift upon reflection. Phase shift upon transmission is always zero regardless of the relative index difference. Furthermore, the intensity reflectance is given by $R = |r|^2$, and the intensity transmittance by $T = |t|^2$.

To begin the derivation for the reflectivity of a stack of dielectric films, consider first a single layer of index n submerged in a background of index n' with $n > n'$. The incident ray is partially reflected off the top surface and acquires a π phase shift. The partially transmitted component travels a distance d (the thickness of the film), is again partially reflected acquiring zero phase shift followed by propagating the distance d, for a total propagation distance of $2d$. For the second ray to be in phase with the initially reflected ray it must accumulate a phase shift of π during its transit through the film. In other words, $kz = 4nd\pi/\lambda_0 = \pi$ is needed, where k is the wavenumber, z is the total propagation distance, and λ_0 is the free space wavelength of the electromagnetic field. Therefore, the minimum film thickness that satisfies this criterion is given by:

$$\lambda_0 = 4nd. \tag{2.3}$$

This procedure may be extended by layering materials of alternating high and low index of refraction, fulfilling the constraint defined by Eqn 2.3. The partially reflected ray produced at each dielectric interface will be in phase at the mirror surface and

constructively interfere, producing a highly reflective multilayer. This forms the basic structure of the distributed Bragg reflector, often referred to as a quarter-wave-stack and shown in Figure 2.1. Finally, a quarter-wave-stack may be designed for a target wavelength λ_{Bragg} using Eqn 2.4:

$$\lambda_{\text{Bragg}} = 4n_1d_1 = 4n_2d_2, \tag{2.4}$$

where n_1 and n_2 are the index of refraction d_1 and d_2 are the layer thicknesses of the alternating layers 1 and 2, respectively.

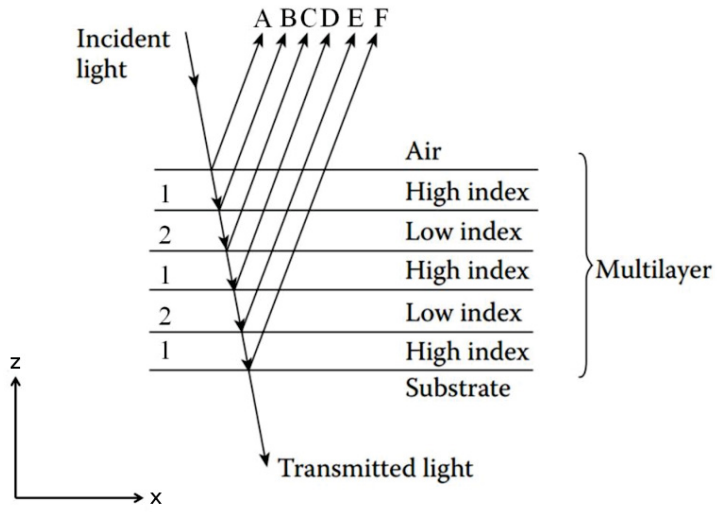

Figure 2.1: Schematic representation of a Bragg reflector comprised of a quarter-wave stack of alternating high and low index medium. Adaped from [65].

Furthermore, just as the Fresnel equations define the reflectance from a single dielectric interface, it can be shown that the peak reflectance of a Bragg reflector is given by [68]:

$$R_{\text{Bragg}} = \left[\frac{n_0(n_2)^{2N} - n_s(n_1)^{2N}}{n_0(n_2)^{2N} + n_s(n_1)^{2N}}\right], \tag{2.5}$$

where, n_0 is the index of the incident media (typically air), n_s is the index of the substrate, n_1 and n_2 are the indices of the multilayer materials, and N is the number

of periods in the Bragg reflector. As the number of periods increases, and with appropriately large index contrast, R_{Bragg} rapidly approaches unity. Experimentally, Bragg reflectors with peak reflectance over 99.999% have been reported [66].

Finally, at normal incidence the Bragg reflectors exhibit high reflectance for a narrow wavelength range near λ_{Bragg}; the width of this high reflection region may be expressed as [69]:

$$\Delta\lambda_{\text{Bragg}} = \lambda_{\text{Bragg}} \frac{4}{\pi} \arcsin\left[\frac{|n_2 - n_1|}{n_2 + n_1}\right]. \tag{2.6}$$

Thus, as seen from Eqn 2.6, the width of the highly reflective region is strictly dependent on the index contrast between the two materials utilised to fabricate the mirror. In order to achieve the required $\Delta\lambda_{\text{Bragg}}$ for a given application, an appropriately large index contrast must be used.

2.1.2 Planar Fabry-Perot Resonator

The canonical Fabry-Perot resonator takes the form of two perfectly parallel mirrors, separated by an optical medium of index n. This geometry is known as a Fabry-Perot etalon or interferometer, and is illustrated in Figure 2.2. Two adjacent rays exiting the resonator will experience an optical path difference resulting in the two rays having a difference in phase which may be expressed as:

$$\delta = 2k_z d = \frac{4n\pi d\cos\theta}{\lambda} = \frac{4n\pi\nu d\cos\theta}{c}. \tag{2.7}$$

Here, $k_z = \frac{2\pi n\cos\theta}{\lambda}$ is the component of the wavevector within the etalon normal to the interface, d is the thickness of the etalon, ν is the frequency of the incident wave, c is the speed of light, and θ is the propagation angle within the medium. As illustrated in Figure 2.2, upon every round trip a portion of the field is transmitted

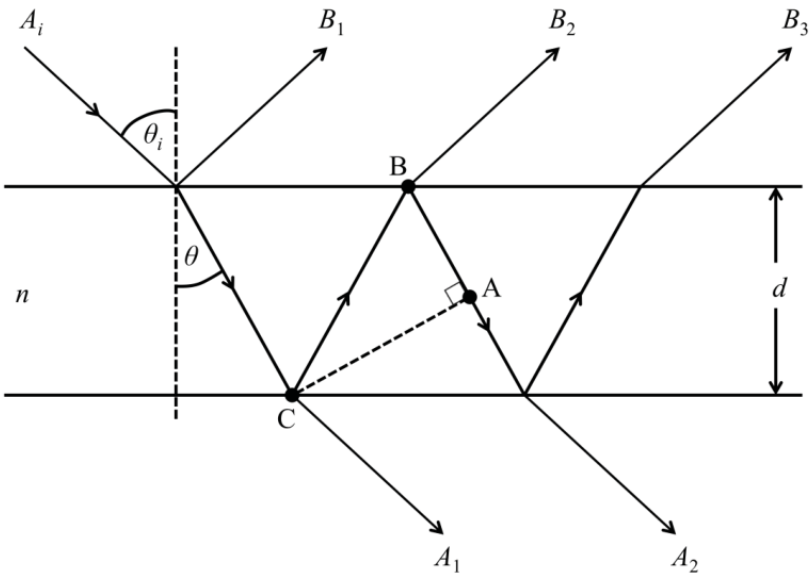

Figure 2.2: Schematic of a Fabry-Perot etalon, multiple reflections are depicted within the cavity as a result of an incident wave at angle θ_i. A_i, A_n and B_n define the amplitude coefficients of the incident, transmitted and reflected fields, respectively. Adapted from [70].

through the etalon. By summing these partial transmitted electric field components, an expression for the net transmitted field may be derived [71]:

$$\begin{aligned} E_t &= A_1 + A_2 + ... \\ &= E_0 t^2 e^{i\omega t} + E_0 t^2 r^2 e^{i(\omega t - \delta)} + E_0 t^2 r^4 e^{i(\omega t - 2\delta)} + ... \\ &= E_0 e^{i\omega t} \left[\frac{t^2}{1 - r^2 e^{-i\delta}} \right]. \end{aligned} \tag{2.8}$$

Here, r and t are the field reflection and transmission coefficients of the mirrors, respectively, and assuming the mirrors are lossless it can be shown that $t^2 = 1 - r^2$. It is often more instructive to recast these equation in terms of intensity, defining $I_0 = |E_0|^2/2$, $I_t = |E_t|^2/2$, and $I_r = |E_r|^2/2$ and multiplying Eqn 2.8 by its complex conjugate, then Eqn 2.8 can be expressed as:

$$\frac{I_t}{I_0} = \frac{(1-R)^2}{(1-R)^2 + 4R\sin^2(\delta/2)}. \tag{2.9}$$

Similarly, for the reflected components:

$$\frac{I_r}{I_0} = \frac{4R\sin^2(\delta/2)}{(1-R)^2 + 4R\sin^2(\delta/2)}. \tag{2.10}$$

Examining Eqn 2.9, it is apparent that transmission is maximized for values of $\delta = 2q\pi$, where q is a positive integer. Utilizing this fact with Eqn 2.7, the resonant frequencies are given by:

$$\nu_q = \frac{qc}{2nd\cos\theta}, \tag{2.11}$$

where ν_q is the optical frequency for a given mode with integer value q. Furthermore, the spacing between two consecutive modes $(\nu_{q+1} - \nu_q)$ is called the free spectral range of the etalon:

$$\Delta\nu = \frac{c}{2nd\cos\theta}. \tag{2.12}$$

Characterization of Fabry-Perot resonators typically can be done using two figures of merit. First, finesse $(\mathcal{F})$ is a measure of the resolving power of a Fabry-Perot interferometer. Secondly, the quality factor (Q) defines the ability of the cavity to store optical energy. The finesse of a Fabry-Perot resonator may be determined from the full-width at half-max (FWHM) of the transmission peaks defined by Eqn 2.9, specified by the point where $I_t/I_0 = 0.5$:

$$\sin^2(\delta_{1/2}/2) = \frac{(1-R)^2}{4R}. \tag{2.13}$$

For a cavity with highly reflective mirrors (i.e. $R \sim 1$) the small angle approximation may be utilized along with Eqn 2.7, and the FWHM in terms of frequency ($\Delta\nu_{1/2}$) can be approximated as:

$$\Delta\nu_{1/2} = \frac{c(1-R)}{2\pi nd\sqrt{R}} = \frac{c}{2d}\frac{1}{\mathcal{F}_{\mathcal{R}}}, \tag{2.14}$$

where $\mathcal{F}_{\mathcal{R}} \equiv \pi\sqrt{R}/(1-R)$ is the reflection finesse. If no other loss mechanisms exist within the system beyond the loss due to partially reflective mirrors, $\mathcal{F}_R$ is equal to the effective finesse of the resonator $\mathcal{F}_{eff}$. The effective finesse can be determined experimentally from the transmission spectrum using the free spectral range and the FWHM of the transmission peak:

$$\mathcal{F}_{\text{eff}} = \frac{\Delta\nu}{\Delta\nu_{1/2}}. \tag{2.15}$$

However, as a result of experimental limitations, the measured finesse is often lower than the reflection finesse. Key limiting factors include spherical defects characterized by a finesse factor $\mathcal{F}_{ds}$, surface irregularities characterized by a finesse factor $\mathcal{F}_{dg}$, and parallelism defects characterized by a finesse factor $\mathcal{F}_{dp}$ (See Figure 2.3). The combination of these define the total defect finesse $\mathcal{F}_d$:

$$\frac{1}{\mathcal{F}_d^2} = \frac{1}{\mathcal{F}_{ds}^2} + \frac{1}{\mathcal{F}_{dg}^2} + \frac{1}{\mathcal{F}_{dp}^2}. \tag{2.16}$$

The overall effective finesse may then be expressed in the form:

$$\mathcal{F}_{\text{eff}} = \left[\mathcal{F}_R^{-2} + \mathcal{F}_d^{-2}\right]^{-1/2}. \tag{2.17}$$

Finally, the quality factor (Q) is defined by the energy stored in the cavity:

$$Q = \omega\frac{(\text{Field energy stored in resonator})}{(\text{Power dissipated by resonator})}, \tag{2.18}$$

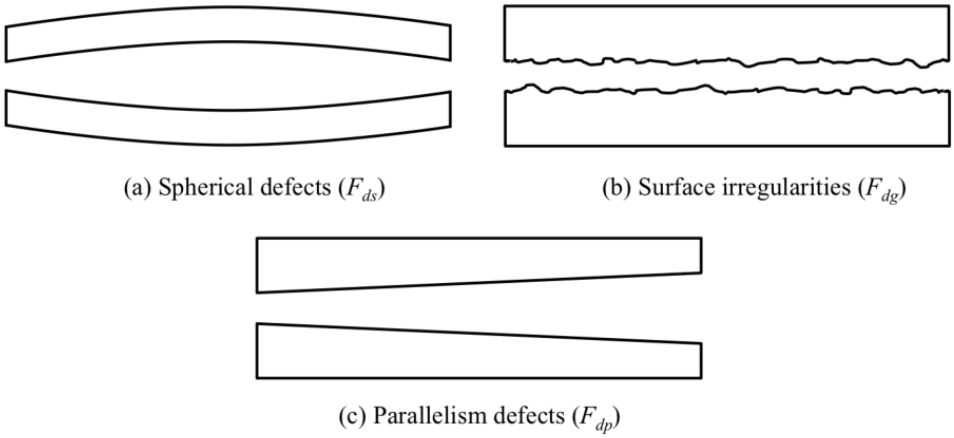

Figure 2.3: Several examples of defects that affect the finesse of a Fabry-Perot resonator.

where $\omega = 2\pi\nu_q$ is the resonant angular frequency of the mode in question. Furthermore, the quality factor may also be defined in terms of the FWHM of the transmission peak and its frequency:

$$Q = \frac{\nu_q}{\Delta\nu_{1/2}} = \frac{q\Delta\nu}{\Delta\nu_{1/2}} = q\mathcal{F}_{\text{eff}}. \tag{2.19}$$

Eqn 2.19 predicts that the quality factor increases linearly with the longitudinal mode number, q, and is directly proportional to the effective finesse of the resonator.

2.1.3 Half-Symmetric Fabry-Perot Cavity

The description above was restricted to Fabry-Perot resonators comprised of two infinite parallel mirrors, illuminated by a uniform plane wave. However, experimental limitations makes producing such conditions virtually impossible. Therefore, typically one or both of the mirrors are curved to provide horizontal confinement of the electromagnetic field (see Figure 2.4). The modes supported within such a cavity are given by the solutions to the paraxial wave equation:

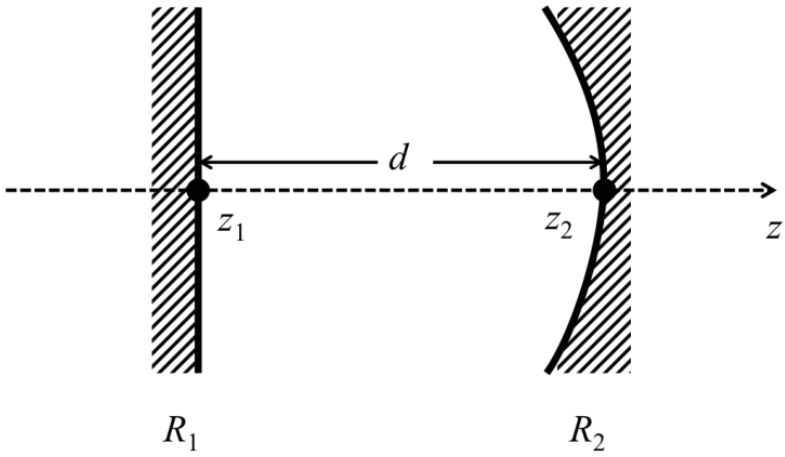

Figure 2.4: Half-symmetric Fabry-Perot resonator, one spherical mirror with radius of curvature R_2, and one planar mirror where R_1 is considered infinite.

$$\nabla^2\psi - 2ik\frac{\partial\psi}{\partial z} = 0. \tag{2.20}$$

Here, ψ defines the shape of the phase fronts of the optical mode, such that:

$$E = E_0\psi e^{-ikz}. \tag{2.21}$$

Solving Eqn 2.21 in Cartesian coordinates gives rise to a complete set of orthogonal modes known as Hermite-Gaussian modes (see Figure 2.5). The field distribution of these modes for a given transverse mode (l, m), where l and m are the x and y mode order, respectively, is given by [73]:

$$\begin{aligned} E_{l,m} &= E_0\tfrac{w}{w(z)}H_l\left(\sqrt{2}\tfrac{x}{w(z)}\right)H_m\left(\sqrt{2}\tfrac{y}{w(z)}\right) \\ &\times \exp\left[-\tfrac{x^2+y^2}{w^2(z)} - ik\tfrac{x^2+y^2}{2R(z)} - ikz + i(l+m+1)\eta\right], \end{aligned} \tag{2.22}$$

where H_l and H_m are Hermite polynomials of order l and m, respectively, and $w(z)$ is the spot size given by:

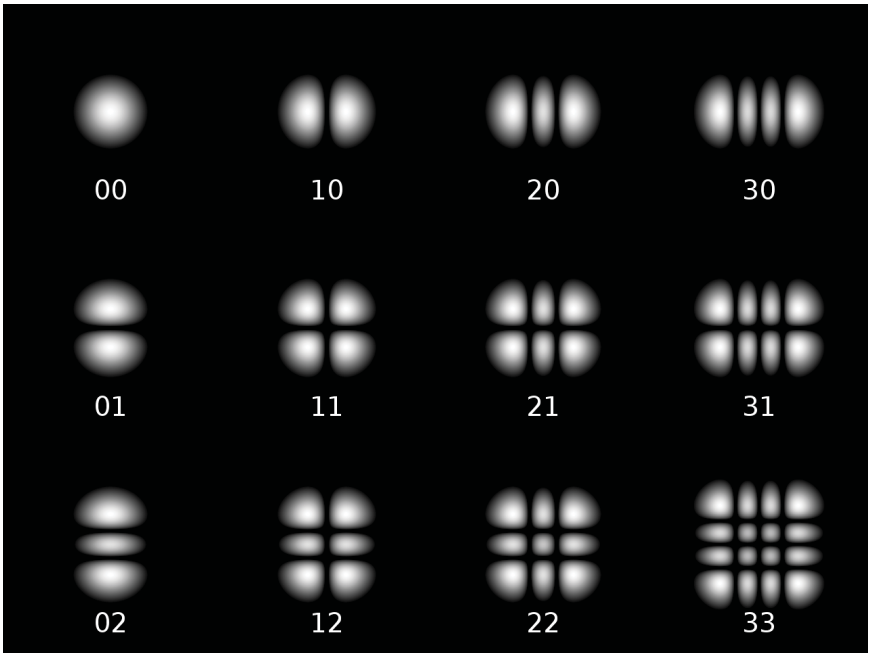

Figure 2.5: Examples of Hermite-Gaussian modes [72].

$$w(z) = w_0 \left[1 + \left(\frac{z}{z_0} \right)^2 \right]^{1/2}. \tag{2.23}$$

Here, w_0 is the minimum spot size determined by the cavity geometry given by [40]:

$$w_0 = \sqrt{\frac{\lambda}{\pi}} \left(d \frac{R_1 R_2}{R_1 + R_2} \right)^{1/4}, \tag{2.24}$$

where d is the length of the cavity, and R_1 and R_2 are the mirrors radii of curvature. In the case of a half-symmetric cavity such that $R_1 \Rightarrow \infty$, Eqn 2.24 simplifies to:

$$w_0 \approx \sqrt{\frac{\lambda}{\pi}} (d R_1)^{1/4}. \tag{2.25}$$

Furthermore, z_0 is the Rayleigh range, also known as the confocal beam parameter, (defining the position at which the beam spot increases to a size of $\sqrt{2} w_0$) and is given by:

$$z_0 = \frac{\pi w_0^2 n}{\lambda}. \tag{2.26}$$

The radius of curvature of the phase fronts $R(z)$ is given by:

$$R(z) = z\left[1 + \left(\frac{\pi w_0^2 n}{\lambda z}\right)^2\right]. \tag{2.27}$$

Finally, η is the Gouy phase shift. This phase shift is a result of the transverse spatial confinement of the focused beam introducing a spread in the transverse momenta. The effective axial wavenumber may be written as $\bar{k}_z = k_z^2/k = k - k_x^2/k - k_y^2/k$, and is associated with the overall propagation phase $\phi(z)$ through $\bar{k}_z = \partial\phi(z)/\partial z$. The first term is phase accumulated by an infinite plane wave (kz), while the second and third terms give rise to the Gouy phase, as given by Eqn 2.28 [74]:

$$\phi_G = -\frac{1}{k}\int^z [k_x^2 + k_y^2]dz. \tag{2.28}$$

This additional phase results in the frequency difference between the transverse optical modes present in the Hermite-Gaussian modes. As described by Eqn 2.22, these additional modes depend on the sum of $l+m$. The Gouy phase for Hermite-Gaussian is explicitly given by:

$$\eta = \tan^{-1}\left(\frac{z}{z_0}\right) = \tan^{-1}\left(\frac{\lambda z}{\pi w_0^2 n}\right). \tag{2.29}$$

For a given transverse electromagnetic mode (TEM_{lm} with indices (l, m)) to be resonant, it must undergo a 2π phase shift upon a round trip within the cavity. Equivalently, for a cavity of length d, a π phase shift must occur on a single pass. This condition may be expressed in the form:

$$\theta_{l,m}(z_2) - \theta_{l,m}(z_1) = q\pi, \tag{2.30}$$

where q is the integer value for the given longitudinal mode. $\theta_{l,m}(z)$ is the phase change of the wave in the direction of propagation, given by:

$$\theta_{l,m}(z) = kz - (l + m + 1)\tan^{-1}\left(\frac{z}{z_0}\right), \tag{2.31}$$

where k is the wavenumber. Neglecting the phase shift upon reflection, since it would cancel out, the resonant condition becomes:

$$k_q d - (l + m + 1)\left[\tan^{-1}\left(\frac{z_2}{z_0}\right) - \tan^{-1}\left(\frac{z_1}{z_0}\right)\right] = q\pi. \tag{2.32}$$

The difference between two adjacent longitudinal modes defines the free spectral range for the TEM_{00} mode:

$$k_{q+1} - k_q = \frac{\pi}{d}. \tag{2.33}$$

Substituting $k = \frac{2\pi\nu n}{c}$ into Eqn 2.33 gives the free spectral range in terms of frequency:

$$\Delta\nu = \frac{c}{2nd}. \tag{2.34}$$

This is the same result obtained for the planar Fabry-Perot resonator at normal incidence. However, as a result of the additional Gouy phase shift the resonant frequency of transverse Hermite-Gaussian modes also depends on the sum of $l + m$. Therefore, in a cylindrically symmetric cavity, modes of constant $l + m$ will be degenerate in frequency; this degeneracy will be broken by any asymmetry of the cavity mirror. From Eqn 2.32 for two adjacent values of $l+m$ the frequency separation of two transverse modes $\Delta\nu_{HG}$ is given by:

$$(k_{q1} - k_{q2})d = [(l + m + 1)_1 - (l + m + 1)_2]\left[\tan^{-1}\left(\frac{z_2}{z_0}\right) - \tan^{-1}\left(\frac{z_1}{z_0}\right)\right]. \tag{2.35}$$

In terms of frequency this becomes:

$$\Delta\nu_{\mathrm{HG}} = \frac{c}{2\pi nd}\Delta(l+m)\left[\tan^{-1}\left(\frac{z_2}{z_0}\right) - \tan^{-1}\left(\frac{z_1}{z_0}\right)\right], \tag{2.36}$$

where $\Delta(l+m)$ is the difference in the sum of two transverse modes. In the case where the cavity is nearly planar (i.e. $d \ll R_1, R_2$) (such as the cavities studied in chapters 3 and 4), Eqn 2.35 simplifies to:

$$\Delta\nu_{\mathrm{HG}} \approx \frac{c}{2\pi nz_0}\Delta(l+m). \tag{2.37}$$

The resonant frequency for a given Hermite-Gaussian mode ($\nu_{q,l,m}$) may be determined by simplifying Eqn 2.32:

$$\nu_{q,l,m} = \frac{c}{2nd}\left\{q + \frac{(l+m+1)}{\pi}\cos^{-1}\left[\pm\sqrt{1-\frac{d}{R_2}}\sqrt{1-\frac{d}{R_1}}\right]\right\}. \tag{2.38}$$

Furthermore, for a half-symmetric cavity when $R_1 \Rightarrow \infty$ this may be simplified to:

$$\nu_{q,l,m} = \frac{c}{2nd}\left\{q + \frac{(l+m+1)}{\pi}\cos^{-1}\left[\pm\sqrt{1-\frac{d}{R_2}}\right]\right\}. \tag{2.39}$$

Finally, the set of Hermite-Gaussian modes defined by Eqn 2.22 are part of a complete set of orthogonal solutions to the paraxial wave equation. However, this is only one of several valid sets of solutions; another commonly used set of solutions obtained in terms of cylindrical coordinates (r, θ, ϕ) are the Laguerre-Gaussian modes, in the form:

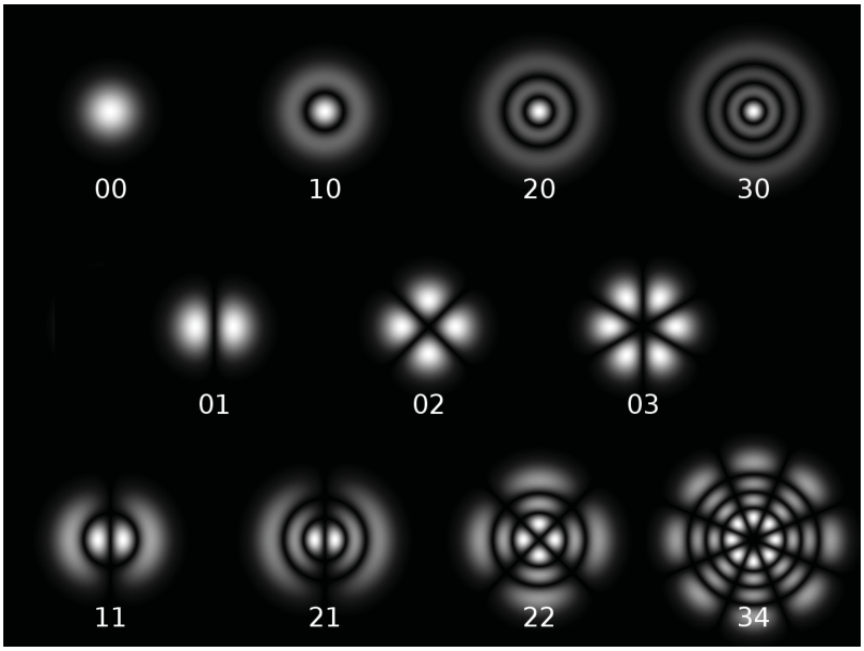

Figure 2.6: Examples of Laguerre-Gaussian modes [75].

$$\begin{aligned} E_{p,l} &= E_0 \tfrac{\sqrt{2}r}{w(z)} L_{p,l}\left(\tfrac{2r^2}{w^2(z)}\right) \\ &\times \exp\left[-\tfrac{r^2}{w^2(z)} \pm il\phi - ik\tfrac{r^2}{2R(z)} - ikz + i(2l+p+1)\eta\right], \end{aligned} \tag{2.40}$$

where $L_{p,l}$ is the associated Laguerre polynomial of order (l, p) where p and l are the mode orders for the radial and azimuthal coordinates, respectively. Due to the cylindrical nature of these modes, they tend to be favored in structures with high degrees of cylindrical symmetry such as the cavities studied in Chapters 3 and 4. However, any slight defect in the shape will allow the existence of Hermite-Gaussian modes and often favor them. For example, laser cavities typically favor Hermite-Gaussian modes as a result of slight defects or misalignment. Laguerre-Gaussian modes can be seen in Figure 2.6.

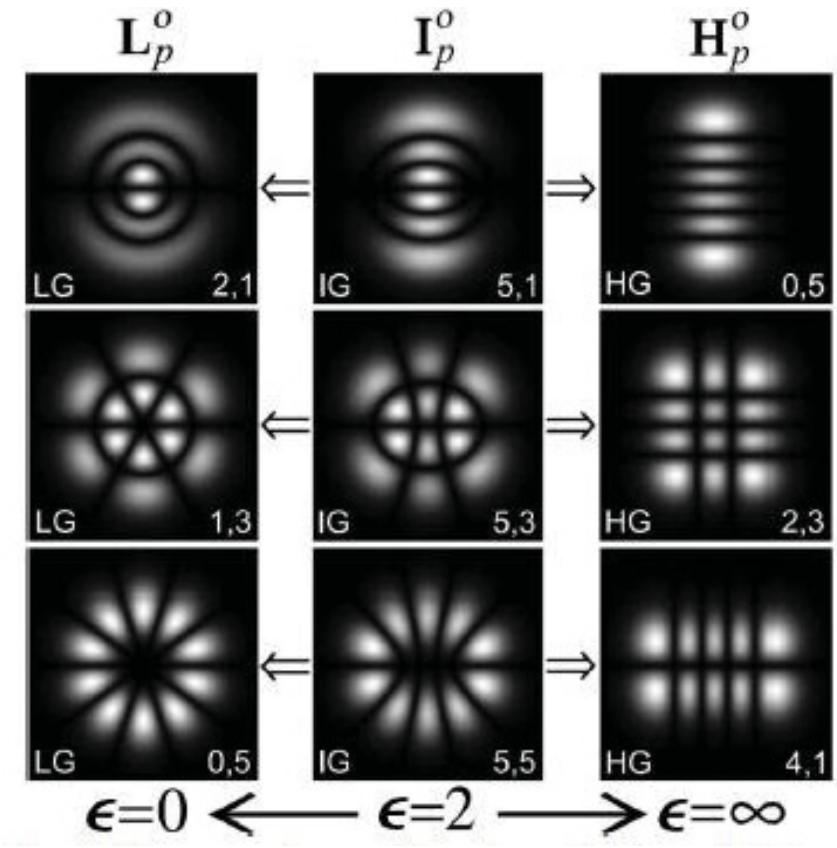

Figure 2.7: Examples of Ince-Gaussian modes [76].

A third and final set of solutions to the paraxial wave equation exist; they are a hybrid between the Hermite-Gaussian and Laguerre-Gaussian modes. Known as Ince-Gaussian modes, they arise in cases of elliptical symmetry and when the cylindrical or rectangular symmetry is slightly broken. There exist two sets of solutions in terms of odd and even Ince polynomials given by:

$$\begin{aligned} E_{\text{odd}} &= S_{\text{odd}} \tfrac{w_0}{w(z)} S_p^m(i\xi,\epsilon) S_p^m(\phi,\epsilon) \\ &\times \exp\left[-\tfrac{r^2}{w^2(z)} + ik\tfrac{r^2}{2R(z)} + ikz - i(p+l)\eta \right], \end{aligned} \tag{2.41}$$

$$\begin{aligned} E_{\text{even}} &= C_{\text{even}} \tfrac{w_0}{w(z)} C_p^m(i\xi,\epsilon) C_p^m(\phi,\epsilon) \\ &\times \exp\left[-\tfrac{r^2}{w^2(z)} + ik\tfrac{r^2}{2R(z)} + ikz - i(p+l)\eta \right], \end{aligned} \tag{2.42}$$

where S_p^m and C_p^m are the odd and even Ince polynomials of order p and degree m, respectively. S_{odd} and C_{even} are normalization constants, (ξ, ϕ) are transverse coordinates, and ϵ is an ellipticity parameter. In the limiting cases where $\epsilon = 0$ or $\epsilon = \infty$, the Ince-Gaussian modes simplify down to Laguerre or Hermite-Gaussian modes, respectively. Some examples of Ince-Gaussian modes are shown in Figure 2.7, and in a few cases were also experimentally observed (see Chapter 3).

2.2 Cavity Quantum Electrodynamics

The prototypical cavity quantum electrodynamics (CQED) system is comprised of two elements: a single two-level atomic emitter trapped within a high finesse optical cavity. Such a system may be utilized to implement the light-matter interactions required to construct a distributed quantum network [16]. This section will explore the theory behind such a system, to elucidate the investigation performed in Chapter 4 regarding the effectiveness of buckled dome microcavities as a quantum light-matter interface.

2.2.1 Quantum Electrodynamics in a Cavity

To motivate the importance of both elements for CQED, first consider a two-level atom resonantly interacting with a faint (single photon) pulse of light that has been focused to a waist w_0. A deterministic atom-photon interaction requires the absorption cross section of the atom to be much larger than the beam spot size, i.e. $\sigma_{abs} \gg A$. Here, $A = (\frac{\pi}{4})w_0^2$ is the area of the beam, and $\sigma_{abs} = \frac{3\lambda^2}{2\pi}$ where λ is the resonant optical wavelength of the atom [77, 78]. At optical wavelengths, even with diffraction limited Gaussian input beams, it follows that this condition is not achievable in free space.

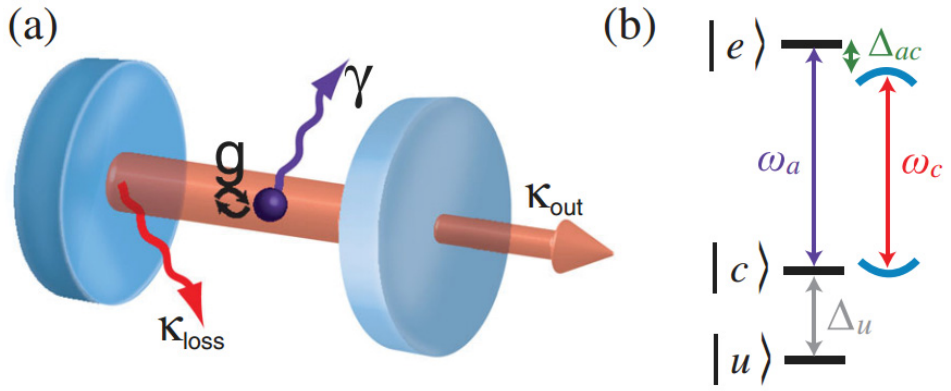

Figure 2.8: The prototypical CQED system. (a) A single three-level atom within an optical cavity, the atom and cavity exchange energy at a rate $2g$. The electric field decays from the cavity at a rate $\kappa = \kappa_{loss} + \kappa_{out}$. The atomic polarization decay rate is γ. (b) Atomic energy structure of the atom. The resonance frequency of the cavity is ω_c, the atomic transition frequency between states $|c\rangle$ and $|e\rangle$ is ω_a, and the atom-cavity detuning is Δ_{ac}. Finally, there exists a decoupled atomic state $|u\rangle$. Adapted from [17].

This situation may be augmented by placing the atom within a Fabry-Perot resonator consisting of mirrors with reflectivity R, such that a photon can bounce back and forth many times, (see Figure 2.8). The multiple passes through the cavity results in an effective increase in the absorption cross-section by the numbers of bounces, given by $\mathcal{F}/\pi$, where $\mathcal{F}$ is the finesse of the cavity defined in Eqn 2.15. Therefore, in order to have a deterministic atom-photon interaction the following condition must be fulfilled:

$$\frac{3\lambda^2}{2\pi} \times \frac{\mathcal{F}}{\pi} \gg \frac{\pi}{4} w_0^2. \tag{2.43}$$

This inequality may be recast using the rates governing the system; the cavity decay rate, κ, the polarization decay rate of the atom, γ, and the atom-cavity coupling rate, g. First, note that the single-photon, atom-cavity coupling rate, g, is determined

by the electric dipole matrix element, μ_{ce}, from the ground state $|c\rangle$ to the excited state $|e\rangle$ [17]:

$$g = \frac{\mu_{ce}E}{\hbar} = \sqrt{\frac{\mu_{ce}^2\omega}{2\epsilon_0\hbar V}} = \sqrt{\frac{3\lambda^2 c\gamma}{4\pi V}}, \tag{2.44}$$

where $\hbar$ is the reduced Planck's constant, V is the optical mode volume in the cavity, ϵ_0 is the permittivity of free space, and it has been assumed that the atom is located at a maxima of the field. Furthermore, the cavity decay rate κ and polarization decay rate γ are defined as followed:

$$\kappa = \frac{\pi c}{2d\mathcal{F}}, \tag{2.45}$$

$$\gamma = \frac{\mu_{ce}^2\omega^3}{6\pi\epsilon_0\hbar c^3}, \tag{2.46}$$

where c is the speed of light, $\omega = 2\pi\nu$ is the angular frequency of the transition, and d is the length of the cavity. Thus, Eqn 2.43 may be rewritten in terms of these rates as follows:

$$C = \frac{g^2}{2\kappa\gamma} \gg 1. \tag{2.47}$$

The parameter C is known as the cooperativity, and C^{-1} is often called the critical atom number, as it represents the number of atoms within the cavity required to significantly modify the transmission properties [79]. From this rather simplistic derivation, one can see that C should be independent of cavity length, since $\kappa \propto 1/d$, and $g \propto 1/\sqrt{d}$. This somewhat simplistic derivation gives insight into the fundamental parameters of importance for CQED; a more detailed description of the dynamics will be presented next.

2.2.2 Jaynes-Cummings Model

Again consider a single two-level atom within a high finesse optical cavity. The atom has a resonance frequency ω_a, the cavity has a resonance frequency ω_c, and the frequency difference is defined as $\Delta_{ac} = \omega_a - \omega_c$. The atom-cavity coupling is described by the dipole approximation and the Hamiltonian may be written as:

$$\begin{aligned} \mathcal{H}_{\text{Int}} &= -\bar{d} \cdot \bar{E} \Rightarrow dE(\hat{\sigma}_{ce}^{\dagger} + \hat{\sigma}_{ce})(\hat{a}^{\dagger} + \hat{a}) \\ &= \hbar g(\hat{\sigma}_{ce}^{\dagger}\hat{a}^{\dagger} + \hat{\sigma}_{ce}^{\dagger}\hat{a} + \hat{\sigma}_{ce}\hat{a}^{\dagger} + \hat{\sigma}_{ce}\hat{a}), \end{aligned} \tag{2.48}$$

where $\bar{d}$ is the atomic dipole moment, $\bar{E}$ is the electric field of a photon within the cavity, $\hat{\sigma}_{ce} = |c\rangle\langle e|$ and $\hat{\sigma}_{ce}^{\dagger} = |e\rangle\langle c|$ are the atomic lowering and raising operators, respectively, and $\hat{a}^{\dagger}$ and $\hat{a}$ are the photon creation and annihilation operators, respectively.

In the interaction picture (or Dirac picture) the terms $\hat{\sigma}_{ce}^{\dagger}\hat{a}^{\dagger}$ and $\hat{\sigma}_{ce}\hat{a}$ experience fast dynamics, such that if $g \ll \omega_a, \omega_c$ these terms may be neglected. Neglecting these terms is known as the rotating wave approximation (or secular approximation). Making this approximation the Hamiltonian for the system may be written as:

$$\mathcal{H}_{\text{JC}} = \underbrace{\hbar\omega_a \hat{a}^{\dagger}\hat{a}}_{\text{Empty Cavity}} + \underbrace{\hbar\omega_c \hat{\sigma}_{ce}^{\dagger}\hat{\sigma}_{ce}}_{\text{Bare Atom}} + \underbrace{\hbar g(\hat{\sigma}_{ce}^{\dagger}\hat{a} + \hat{\sigma}_{ce}\hat{a}^{\dagger})}_{\text{Dipole Coupling}}. \tag{2.49}$$

This Hamiltonian can be diagonalized revealing the following energy eigenstates [80]:

$$E_0 = 0, \tag{2.50}$$

$$E_{N,\pm} = N\hbar\omega_c + \frac{\hbar\Delta_{ac}}{2} \pm \frac{\hbar}{2}\sqrt{\Omega_N^2 + \Delta_{ac}^2}. \tag{2.51}$$

Here, N is a positive integer representing the total number of excitation quanta in the system, $\Omega_N = 2g\sqrt{N}$ is the N-quanta Rabi oscillation frequency. This energy

spectrum is plotted in Figure 2.9 as a function of atomic detuning, $\Delta_{ac} = \omega_a - \omega_c$, and is known as the Jaynes-Cummings ladder [81].

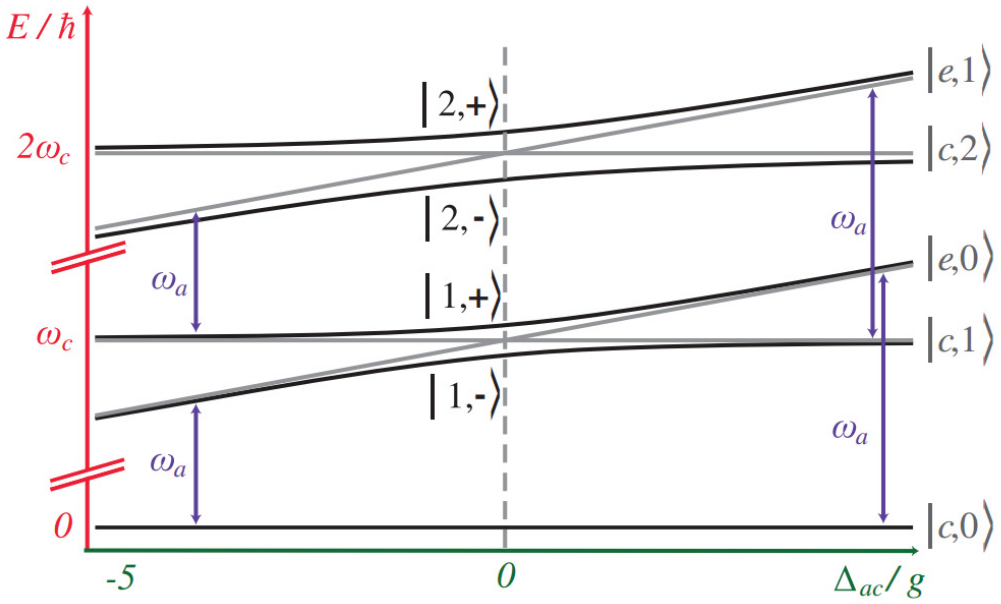

Figure 2.9: The Jaynes-Cummings ladder of coupled eigenstates (black) and uncoupled eigenstates (grey), where the cavity frequency ω_c is kept constant, and the atomic frequency ω_a is scanned over the resonance. At zero detuning the levels are separated by $2g\sqrt{N}$. Adapted from [17].

Furthermore, the eigenstates of the coupled system $|N, \pm\rangle$ are a superposition of the states $|e, N-1\rangle$ and $|c, N\rangle$. On resonance $\Delta_{ac} = 0$:

$$|N, \pm\rangle = \frac{1}{\sqrt{2}}(|e, N-1\rangle \pm |c, N\rangle), \tag{2.52}$$

This superposition of states results in key dynamics of the system. Consider the case with an atom prepared in its excited state $|e\rangle$ inside a cavity with $N-1$ photons. This state may be written as $|e, N-1\rangle = |N, +\rangle + |N, -\rangle$. Calculating the probability of the atom being in its excited state $|e\rangle$ reveals $P_{|e\rangle}(t) = \cos^2(\Omega_N t/2)$, meaning the system undergoes Rabi oscillations at the frequency $\Omega_N = 2g\sqrt{N}$. In the limit where

$N-1=0$, (i.e. initially there are no photons inside the cavity), the oscillations occur at $\Omega_1 = 2g$, which is known as the vacuum-Rabi frequency.

2.2.3 Implementations of CQED

Any experimentally realized implementation of an atom-cavity system is an open system with two main loss mechanisms. Photons may be lost at a rate $\kappa = \kappa_{\text{loss}} + \kappa_{\text{out}}$, where κ_{loss} is due to photons being scattered or absorbed by the mirrors, and κ_{out} is due to photons passing through the partially reflecting mirrors and exiting the cavity along the output mode of the resonator. The second decay channel is through the atomic polarization decay of the atom at a rate γ, which may be through the decay into an auxiliary state $|u\rangle$, or by spontaneous emission into free-space.

The dynamics of such an open atom-cavity system may be simulated using the Lindblad form of the quantum master equation [82]:

$$\dot{\rho} = \frac{1}{i\hbar}[\mathcal{H}_{Int}, \rho] + \sum_i \left[L_i \rho L_i^\dagger - \frac{1}{2}(L_i^\dagger L_i \rho + \rho L_i^\dagger L_i) \right], \tag{2.53}$$

where $\rho = |\psi\rangle\langle\psi|$ is the density matrix operator of the system. In the case of the atom-cavity system $L_1 = \sqrt{2\gamma}\hat{\sigma}_{ce}$ and $L_2 = \sqrt{2\kappa}\hat{a}$, representing the atomic and photonic loss, respectively.

Investigating the dynamics of the system using Eqn 2.53, three separate regime emerge. First, for $C \ll 1$ the dynamics of the system are nearly identical to that of the free-space case and are therefore largely uninteresting. In the case where $C \gg 1$, two distinct regimes exist: the "Purcell" or fast cavity regime for which $\kappa > g$ and any photon emission is an irreversible process, and the "strong-coupled" regime where $g > \kappa$ and energy may be reversibly exchanged between the cavity and the atom.

The strong-coupled regime is the most highly sought regime, as the reversible transfer of energy between the atom and cavity allows the engineering of many atom-

photon interactions. In this regime the atom-cavity coupling is the fastest rate in the system:

$$g > \kappa > \gamma, \tag{2.54}$$

and therefore this is the only regime for which it is possible to observe the vacuum Rabi oscillations.

Finally, the Purcell regime is characterized by $\kappa > g > \gamma$ and $C \gg 1$, such that the Rabi oscillations cannot be observed because the photon will leak from the cavity before being reabsorbed by the atom. Nevertheless, the dynamics of this regime are still strongly modified from that of the free-space system. Most notably the atomic decay rate into the cavity is strongly enhanced and may be determined by solving Eqn 2.53:

$$\gamma_c = \frac{g^2\kappa}{\kappa^2 + \Delta_{ac}^2}. \tag{2.55}$$

Remarkably, on resonance ($\Delta_{ac} = 0$), the cavity enhanced decay rate $\gamma_c = 2C\gamma$ may be much larger than the free-space decay rate γ, leading to the notion of the "one-dimensional" atom [47, 83]. This increased decay rate, most notably, may be utilized to implement highly efficient single photon sources. It can be shown that the fraction of photons emitted into the cavity mode is given by:

$$\frac{\kappa_{out}}{\kappa}\frac{\gamma_c}{\gamma + \gamma_c} = \frac{\kappa_{out}}{\kappa}\frac{2C}{1 + 2C}. \tag{2.56}$$

Therefore, for $C \gg 1$ the extraction efficiency of single photons approaches unity.

Chapter 3

Visible-Band Microcavities Fabricated via Buckling Self-Assembly of SiO_2/Ta_2O_5 Multilayers

In 1899 Alfred Perot and Charles Fabry described a method for distinguishing small differences in wavelength utilizing two silver mirrors separated by an air-gap [84]. This device is known as a Fabry-Perot interferometer, and is used for filtering and storing electromagnetic radiation. However, cavities fabricated from two planar mirrors, such as described in their initial work, suffer from several drawbacks that result in limitations to the finesse and quality factor attainable. Defects such as non-parallelism and undesirable mirror curvature cause the radiation to leak from the cavity [85]. However, it has been demonstrated that by intentionally introducing curvature to one or both mirrors, electromagnetic radiation may be better confined within the cavity [86].

Advances in fabrication techniques have allowed the recent development of many diverse high finesse optical cavities. Cavities utilizing macroscopic mirrors have recently been demonstrated to have a finesse of ∼480 000 [66, 57], and, moreover, recently reported cavities fabricated using optical fibers have reported a peak finesse of 21 000 [40]. Chip-based cavity designs fabricated utilizing CO_2-laser ablation of glass substrates [62, 87] and FIB milling [59, 88] have exhibited finesse of 25 000 and 33 000, respectively. However, these serial fabrication techniques produce devices one at a time and often require lengthy processing time to fabricate multiple devices. Many applications, including lab-on-a-chip and chip-based sensors, benefit from the parallel fabrication of multiple devices.

This chapter discusses the migration of a buckling self-assembly fabrication technique, previously utilized to produce optical cavities in the 1550 nm range, to the near-visible portion of the infrared spectrum. This technique allows the parallel fabrication of tens of devices per square centimeter, and potentially enables connectivity between cavities via hollow channels. These channels provide open-access to the hollow cavities, which is crucial for applications such as lab-on-a-chip diagnostics, chip-based dye lasers, and CQED.

3.1 Fabrication

Over the past several years, the primary focus of the DeCorby group has been on the fabrication of hollow-core microcavities and waveguides utilizing a guided delamination buckling procedure. In that time, chalcogenide waveguides [89], silicon based waveguides and cavities [63, 90], and recently waveguides for visible wavelength operation have been investigated [91]. The main goal of the present work was to further refine this procedure and to produce microcavities with resonance frequencies in the $\sim$ 780 nm range relevant to CQED [64]. Such cavities may allow the future explo-

ration of cavity quantum electrodynamics, lab-on-chip based sensing, and on-chip dye based lasers.

The basic fabrication process may be described as follows. First, a Bragg reflector is deposited onto a cleaned fused-silica wafer. A low-adhesion fluorocarbon layer is patterned using a standard lithographic lift-off procedure. A second Bragg reflector matching the initial mirror is deposited, with deposition parameters chosen such that the resulting mirror is under biaxial compressive stress. The final step is heating the sample to induce the release of the top mirror, allowing the compressive stress to drive the formation of hollow structures (see Figure 3.1).

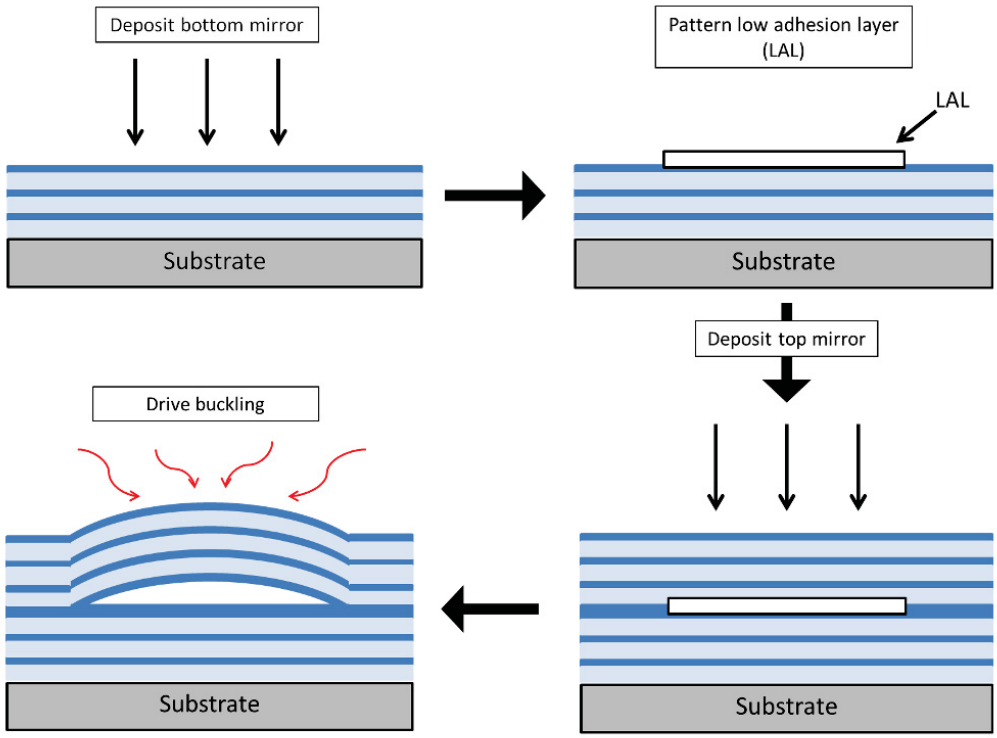

Figure 3.1: Process used for the fabrication by guided delamination buckling. A low-adhesion fluorocarbon layer is sandwiched between two identical Bragg reflectors. The top reflector exhibits high compressive stress, and is released though a heating process. The compressive stress of the top reflector drives the formation of hollow structures.

3.1.1 Thin Film Deposition

Thin film deposition methods have been extensively studied over the past several decades, providing many alternatives for the layering of optical materials [92, 93, 94]. These methods include chemical vapor deposition (CVD) [95], thermal and electron beam evaporation techniques [96], sputtering [97, 98], and many others; all have specific benefits and drawbacks. However, since both optical properties and thin-film stress were crucial for this work, sputtering was the natural choice. It allows control of both these properties through the tuning of the deposition parameters.

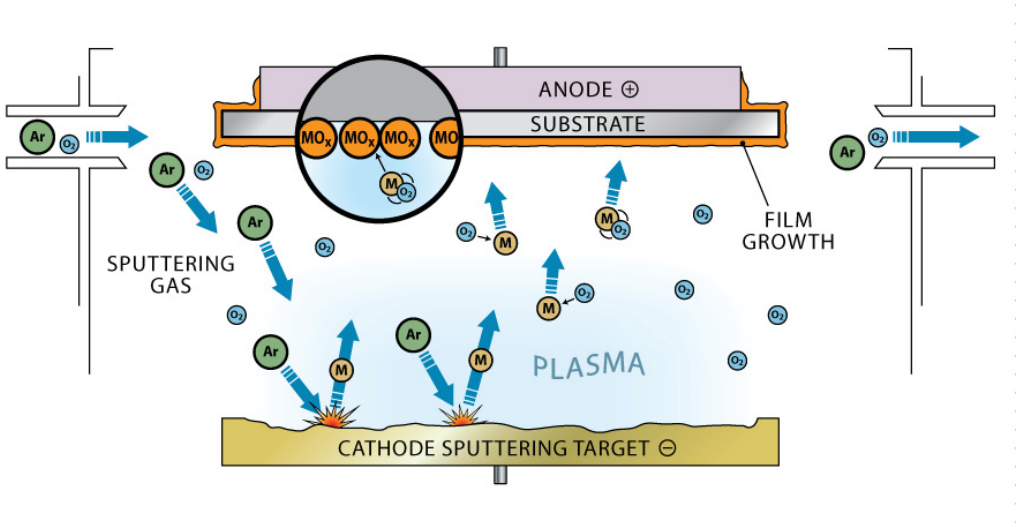

Figure 3.2: Schematic of a typical reactive sputtering system. (from [99])

A typical sputtering system is comprised of two electrodes, the target material as the cathode and the substrate as the anode, housed within a vacuum chamber (see Figure 3.2). The chamber is evacuated to remove water vapor as well as any chemically reactive gases, oxygen and nitrogen being the most notable examples. A heavy, chemically inert gas is introduced into the chamber; argon is often used as it does not chemically interact with the target or substrate material. A potential difference, typically several hundreds of volts, is applied between the cathode and anode, causing the release of electrons that are accelerated by the large electric field. These

accelerated electrons collide with the argon atoms within the chamber producing a plasma of argon ions, known as a glow discharge. The positively charged argon ions are then accelerated towards the target, colliding as well as causing the ejection of target material, and of additional secondary electrons. This process cascades, until a steady state plasma of electrons and ionized argon is produced. The liberated target atoms that had been ejected in this process condense on the substrate, forming the desired film.

This process results in the successful deposition of the desired film, however it has several limiting qualities [98]. First, this process must operate at relatively high pressures ($\sim 10 - 100$ mTorr), because the electrons travel in a direct path between the cathode and anode and thus have a low probability of colliding with argon atoms and ionizing them. Furthermore, any target atoms ejected from the target must travel through the relatively dense atmosphere inside the chamber. At the required operation pressure, the mean free path for a particle is on the order of one millimeter, and thus any target atoms will scatter many times on transit to the substrate. This scattering has a two-fold effect: first, many target atoms will scatter and not reach the substrate, reducing the deposition rate, and second (and more important), the target atoms that do reach the substrate will have lost much of their initial kinetic energy due to the multiple scattering events. Films produced from these low energy atoms exhibit relatively low density, resulting in low mechanical strength and poor optical properties.

These shortcomings have been overcome by the advent of magnetron sputtering, in which a strong magnetic field traps secondary electrons near the surface of the target [100, 101]. A ring magnet produces a magnetic field perpendicular to the electric field just above the target surface. These perpendicular fields produce an $\bar{E} \times \bar{B}$ drift that is experienced by the electrons, trapping them in a ring just above the target. This results in a higher concentration of electrons and therefore a higher

concentration of ionized argon atoms near the target surface. This highly dense ring of plasma produces a large flux of ions, forming a distinctive ring wear pattern known as a racetrack. Furthermore, since there is a much larger concentration of trapped secondary electrons, the density of argon may be reduced to maintain a stable plasma. Pressures as low as $\sim$ 1 mTorr may be utilized in some situations. The ability to reduce the pressure and concentrate the plasma near the target surface produces a mean free path for target atoms that is much longer, thus more energetic particles are able to reach the substrate. This energetic particles result in a more dense film, and such films have been shown to have improved optical and mechanical properties [102].

The process described up to this point is the standard method for depositing many metallic materials. However, it is also possible to deposit several dielectric materials such as SiO_2, Ta_2O_5, TiO_2, AlO_2, and many others, through a process called reactive sputtering. Following the basic principles above, target material is sputtered. However, an additional reactive gas (typically oxygen or nitrogen) is introduced into the sputtering chamber. As the ejected atoms condense onto the substrate, they chemically interact with the additional gas, forming the desired dielectric compound. However, this reaction does not only occur on the substrate, but also on all surfaces within the chamber, including the walls, shutter, and the target itself. As this material that forms is a dielectric, several issues arise that limit the effectiveness of the sputtering process. First and most notable is "poisoning" of the target, which is characterized by the buildup of dielectric material on the target surface. This dielectric layer results in a reduced sputtering rate, and also may affect the quality of the film produced [93]. During the sputtering procedure, ion bombardment will continually clear the dielectric buildup from the racetrack region; however, a dielectric film will continue to build up on the periphery of the target. Low energy argon ions that find their way to this film will begin to charge the top surface, essentially producing

a capacitor between the conductive target material below, and the charged plasma above. As normal operation continues, this charge will continually build up until it exceeds the breakdown voltage of the dielectric, resulting in a discharge or arc. Such arcing events often lead to large pieces of target material being ejected and damaging the substrate, or may even damage fragile targets (such as pure silicon targets [103]).

Early solutions to the issue of target poisoning included radio-frequency sputtering [104], but due to several limitations such as a low sputtering rate and scalability, the deposition of dielectrics is dominated by pulsed DC magnetron sputtering [105, 106]. A schematic of a typical target bias for a pulsed DC system is shown in Figure 3.3. The target bias is switched between normal operation (negative voltage, approximately -400 V, for time τ_{on}) and reverse bias (positive voltage, approximately 100 V, for time τ_{off}) at a frequency in the kHz range. During the normal operation "τ_{on}", a dielectric film will build up on the target and begin to charge as argon ions land on the dielectric. If the target was left in this state, charge would continue to build until an arc occurs. Prior to an arc occurring, the voltage is switched to reverse bias "τ_{off}"; during this time electrons are pulled onto the dielectric film, canceling the charge produced by the argon ions. Moreover, the dielectric film will begin to exhibit a net negative charge as more electrons build up on the surface. Upon reverting to normal operation the dielectric film has a net negative charge, whereas the racetrack region will be neutral. Therefore, argon ions will preferably sputter the dielectric film as it will have a larger bias voltage [103]. This ensures the removal of the dielectric layer and thus will ensure the target does not become poisoned. Since the electrons have a much larger mobility than the argon ions, the off time is typically much shorter than the on time. A reasonable duty cycle $\tau_{\text{on}}/(\tau_{\text{on}}+\tau_{\text{off}})$ may be as high as ninety percent; as a result, deposition rates are often comparable to that of standard DC sputtering.

A second issue resulting from reactive sputtering is the continual buildup of dielectric on the chamber surface. As the anode of most sputtering systems consists of the

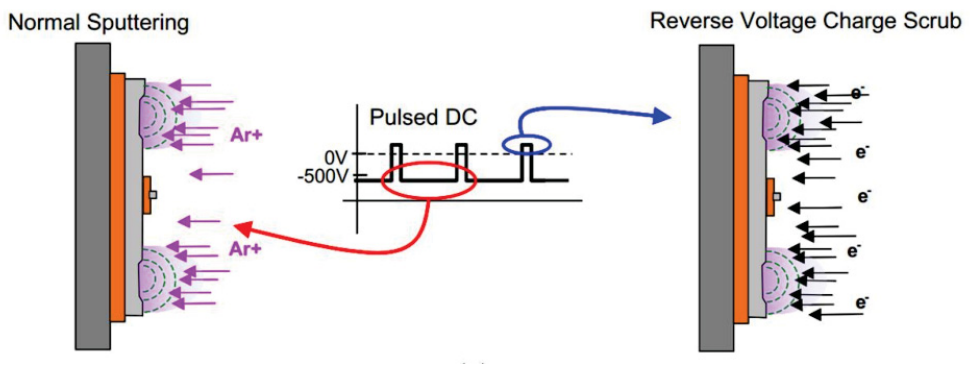

Figure 3.3: Schematic of the typical operation of a pulsed DC magnetron sputtering system (adapted from [107]). During normal operation argon ions bombard the surface of the target and sputtering occurs. During reverse bias electrons are pulled onto the surface to neutralize the charge that has built up.

internal surfaces of the system, which are held at ground relative to the target. This buildup of dielectric begins to electrically shield the anode from the target, resulting in an effect known as the disappearing anode. If dielectric films become too thick, this may result in the extinguishing of the plasma and the ending of any deposition [108]. This effect is mediated by ensuring all surfaces are cleared of the dielectric film prior to every deposition.

Depositions for this work were performed in the sputtering system shown in Figure 3.4. This system is housed in the Nanofab facility at the University of Alberta. It is a three-gun Kurt J Lesker magnetron sputtering system, capable of pulsed DC operations using an AE Pinnacle Plus power supply. Substrates were loaded on a heating chuck capable of a maximum substrate temperature of 150°C. This system used three inch targets, installed into water-cooled copper guns, which are approximately twenty centimeters from the substrate holder. Typical operation allowed a one hour pump down of the chamber to a base pressure $\sim 10^{-6}$ Torr. The chamber was subsequently back-filled with argon to a pressure of 10 mTorr.

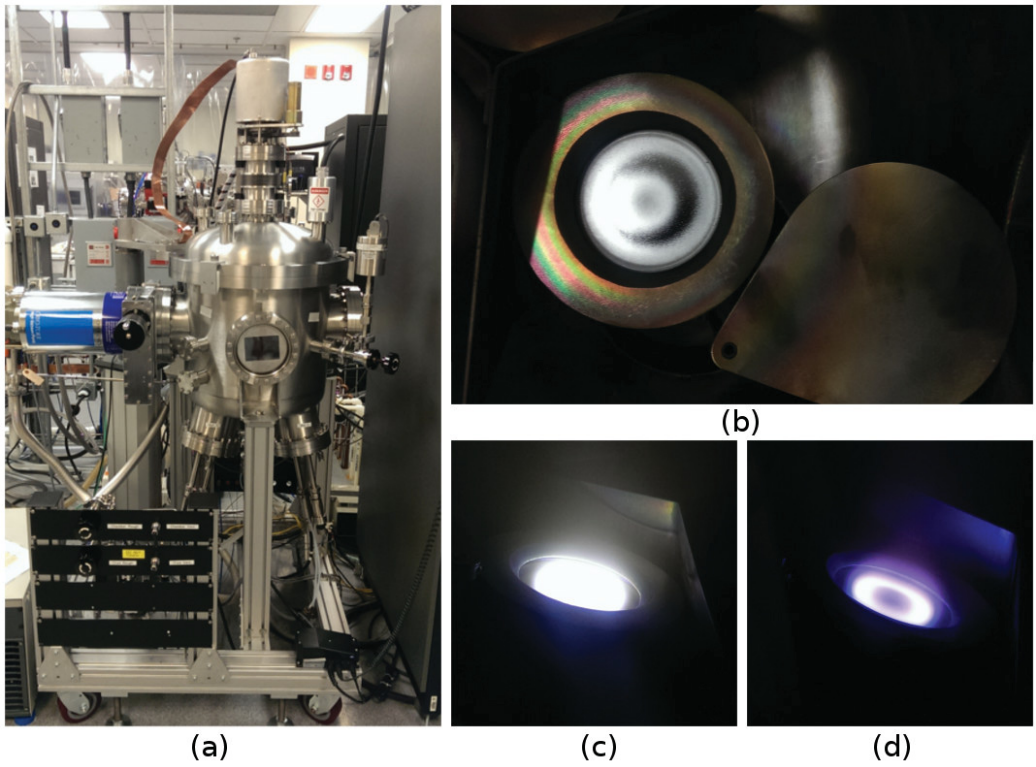

Figure 3.4: (a) The sputtering system used for all depositions in this work. (b) A loaded target within the sputtering system, the movable shutter is open to show the target. (c,d) Typical glow discharge during a deposition, the distinct ring glow seen clearly in (d) is a result of the magnetic confinement.

3.1.2 Distributed Bragg Reflector

The deposition of the Bragg reflectors required the intimate knowledge of the monolayer properties of the two materials utilized. Previous work [91] had demonstrated that SiO_2/Ta_2O_5 Bragg reflectors provided a good combination of optical and mechanical properties and were therefore an obvious choice for this work. Single films were deposited and both optical and mechanical properties of these films were examined. Optical properties were obtained using ellipsometry (J.A Woollam VASE) and mechanical data was obtained using a Flexus stress measurement system.

Silicon dioxide (SiO_2) was utilized as the low index material in this work, and in fact is one of only a few low-index materials produced via sputtering [104]. The

optimization of the deposition parameters was largely performed previously [109]; the largest difficulty had been target arcing and the eventual damage of the pure silicon target.

The test depositions were performed onto piranha cleaned n-type silicon substrates, purchased from the Nanofab. The substrates were heated to 150°C during the deposition, as this has been shown to improve the stoichiometry of silicon dioxide films [110]. Furthermore, following loading of the target and substrate, the chamber was evacuated to a base pressure of $\sim 10^{-6}$, and was back filled with argon to a pressure of 10 mTorr. Previous work [109] had observed a trade-off between mechanical stress and optical loss, and a recipe was developed with an optimal balance of these two properties. The deposition parameters are listed in Table 3.1. A relatively high target power of 200 W was used to ensure that ejected target ions had high kinetic energy, and a low oxygen flow rate of 3.2 sccm was used, compared to 4.0 sccm for the recipe optimized strictly for low loss. Finally a deposition pressure of 4.0 mTorr was used to allow the target atoms to retain as much kinetic energy as possible, while safely maintaining the plasma. The resultant optical properties, determined from the ellipsometry measurements, are plotted in Figure 3.5. At a wavelength of 780 nm, the index of refraction was found to be $n = 1.49$, with an extinction coefficient of $k = 5.98 \times 10^{-5}$.

Table 3.1: Silicon Dioxide sputtering parameters.

Film	Power (W)	Freq. (kHz)	Off-time (μs)	Ar flow (sccm)	O_2 flow (sccm)	Pressure (mTorr)	Dep. rate (nm/s)	n_{780}	k_{780}	Stress (MPa)
SiO_2	200	150	0.8	50	3.2	4.0	0.28	1.49	6×10^{-5}	-280

The issues of target arcing and fracture were largely solved previously, due in part to several key modifications to the sputtering process. While loading the target into the system, an additional aluminium spacer ring was placed to provide structural support to the edge of the target, where fracturing typically occurred. The top clamping

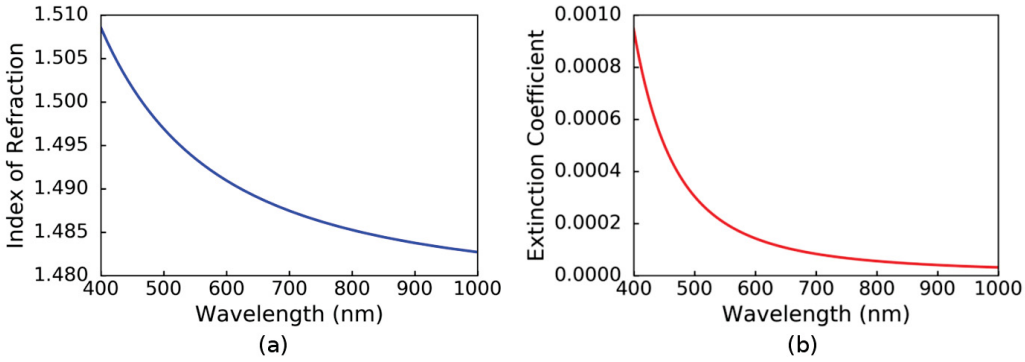

Figure 3.5: (a) Index of refraction and (b) extinction coefficient of sputtered SiO_2. Optical constants were obtained from ellipsometry via Cauchy fits.

ring was ensured to be tightened uniformly and lightly snug; over-tightening or non-uniform pressure lea to fractures preferentially occurring at the clamping points. The targets were also ramped from 0 W to the operation power of 200 W over a period of ten minutes, to reduce the thermal shock imparted on the target (a 10 minute ramp was also utilized while powering down the target). Furthermore, the ramp was performed in a purely argon environment at a high pressure of 10 mTorr, again to reduce any additional stress to the target. Finally, it was found that silicon targets that had been elastomer-bonded to a copper backing target (Kurt J Lesker) were able to better withstand repeated use. This is likely due to improved thermal contact via the metallic layer, but also partially attributable to the additional structural support from the bonding material.

Tantalum pentoxide (Ta_2O_5) was used as the high-index material for this work. It is a commonly used high-index material [101, 111] and has been previously utilized with silicon dioxide to produce high finesse cavities [40, 57]. Other materials such as titanium oxide were also examined [112, 113]; however, it was determined that tantalum pentoxide had superior optical as well as mechanical properties. Monolayers were deposited using a 99.95% pure tantalum target onto cleaned silicon wafers, just as in the case of silicon dioxide. For these depositions, the substrate was also heated

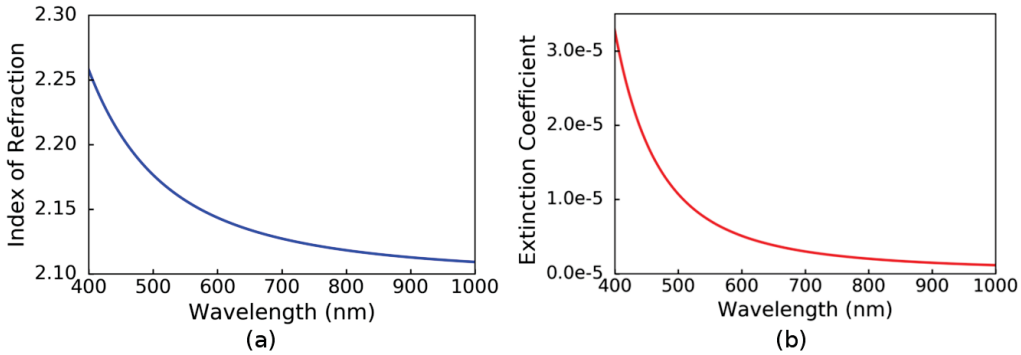

Figure 3.6: (a) Index of refraction and (b) extinction coefficient of sputtered Ta_2O_5. Optical constants were obtained from ellipsometry via Cauchy fits.

to 150°C, in spite of the fact that the increased temperature has been shown to have detrimental effects on the stoichiometry of tantalum pentoxide [114]. However, for thin layers (< 1 μm) such as those used in this work, these effects were found to be negligible. Depositions were performed with a target power of 200 W, in an oxygen-rich environment (20 sccm of oxygen and 40 sccm of argon). The full operation parameters are listed in Table 3.2, and the extracted optical parameters are shown in Figure 3.6. At a wavelength of 780 nm, the index of refraction was found to be $n = 2.12$ with an extinction coefficient $k \leq 1 \times 10^{-5}$.

Table 3.2: Tantalum pentoxide sputtering parameters.

Film	Power (W)	Freq. (kHz)	Off-time (μs)	Ar flow (sccm)	O_2 flow (sccm)	Pressure (mTorr)	Dep. rate (nm/s)	n_{780}	k_{780}	Stress (MPa)
Ta_2O_5	200	20	5.0	40	20	4.0	0.23	2.12	$< 10^{-5}$	-230

Utilizing the results from the monolayer depositions and Eqn 2.4, Bragg reflectors were designed to operate at a free-space wavelength $\lambda_0 = 780$ nm, corresponding to the D2 line of ^{87}Rb. The targeted film thicknesses (from Eqn 2.4) were 130 nm for silicon dioxide and 90 nm for tantalum pentoxide. Prior to the deposition of the final mirrors, two-period test mirrors were deposited to ensure the produced mirror had the desired characteristics. This two-period mirror was deposited on a silicon wafer, and

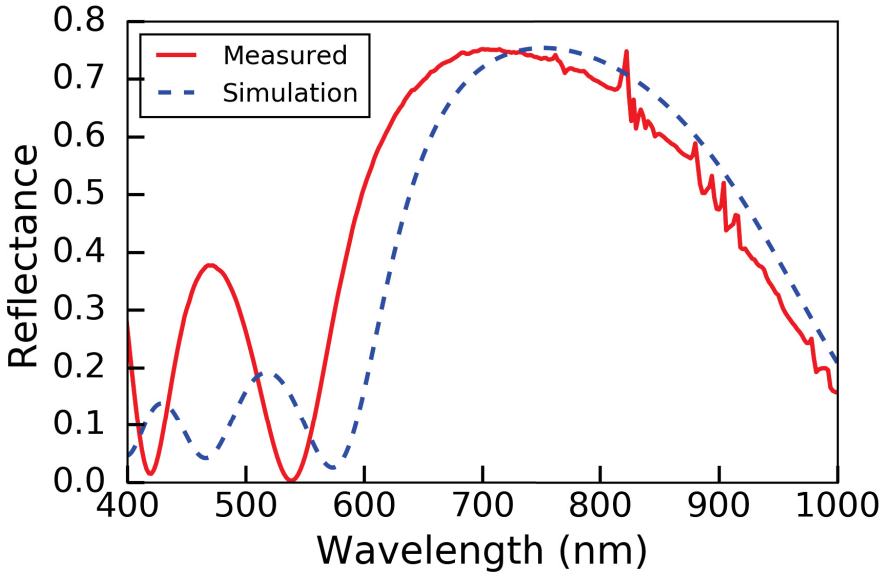

Figure 3.7: Experimentally measured mirror reflectance of a two-period SiO_2/Ta_2O_5. Simulation results assumed film thicknesses of 130 nm for SiO_2 and 90 nm for Ta_2O_5. Utilizing the measured total film thickness, it was determined the deposition rate of Ta_2O_5 was reduced compared to the bulk rate.

the reflectance is plotted in Figure 3.7, along with fits obtained from transfer-matrix simulations.

The fits revealed a decrease in the deposition rate of tantalum pentoxide compared to the rate determined from the monolayers. This may be a result of a surface interaction with the silicon dioxide interface, reducing the formation of the initial tantalum pentoxide film. However, a new deposition rate was extracted using the optical fits as well as thickness measurements obtained with a surface contact profilometer. Finally, ten and a half period (starting and ending with tantalum pentoxide) Bragg reflectors were deposited onto a cleaned fused silica wafer. The reflectance measurements and the transfer matrix fit are shown in Figure 3.8, demonstrating good agreement between the experimental measurement and the theoretical prediction. The peak reflectance of this mirror was estimated to be $R = 0.9991$, corresponding to a reflectance limited finesse $\mathcal{F} \approx 3500$ (see Section. 2.1.2). A second, nominally identical

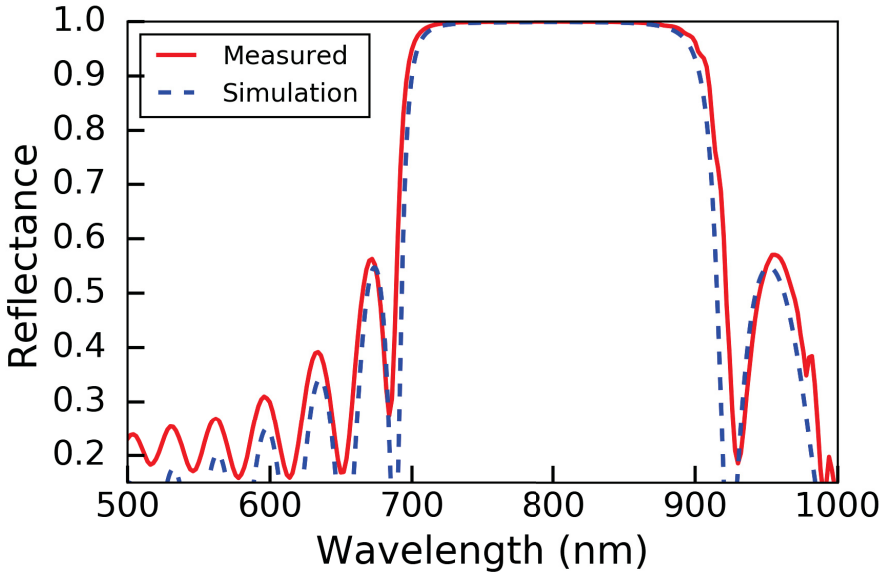

Figure 3.8: Experimentally measured reflectance of a ten-period SiO_2/Ta_2O_5 mirror. Simulation results assumed film thicknesses of 130 nm for SiO_2 and 90 nm for Ta_2O_5.

mirror was deposited following the deposition of a low adhesion layer, as described in the following section.

3.1.3 Guided Delamination Buckling Self-Assembly

In order to produce deterministic structures, the buckling of the top Bragg reflector is guided through the use of a low adhesion layer patterned onto the bottom Bragg reflector [115]. The shape of these low adhesion regions defines the type of buckled features produced, ranging from long strip waveguides, to circular dome cavities. Low adhesion between two layers has historically been produced in two ways: surface treatments [116], or thin layers such as diamond-like carbon [117] or metallic layers [118]. For the present work, a fluorocarbon based polymer was used due to its favorable properties. Namely, patterning was relatively straightforward utilizing a lithographic lift-off procedure, the fluorocarbon was found to be optically transparent

in the wavelength region of interest, and it was able to survive the pump down and substrate heating within the sputtering chamber.

Polytetrafluorethylene (PTFE) is also known by its commercial name Teflon ®, and consists of long carbon chains with CF_2 groups. It is well known that this material has a low coefficient of friction, and exhibits low surface energy, making it a natural choice for the low adhesion layer in this work [119, 120]. Moreover, the deposition of thin fluorocarbon films has been well documented in literature as it forms the passivation layer of the Bosch process [121, 122]. Furthermore, the fluorocarbon films deposited using this procedure exhibit low pin-hole density, low surface energy, and are capable of surviving high vacuum environments. Experimental optimization using a commercial plasma reactive ion etch system (ICP-RIE Alcatel AMS110) was conducted, and it was found that a ten second deposition with a 600 W coil power produced suitable films. Features are pattered using a lithographically defined mask of HPR 504 (a standard optical photo-resist), which was removed, following the deposition of the fluorocarbon layer, via an acetone sonication lift-off procedure. This was followed by an hour-long anneal on a hotplate at 100°C to smooth the top surface of the fluorocarbon layer. The features were optically examined under a microscope to ensure uniformity and smooth features, qualities that have proven to be critical for successful buckling [90] (see Figure 3.9).

A second Bragg reflector, nominally identical to the first, was deposited on top of the fluorocarbon layer. The biaxial compressive stress was determined using the Flexus stress measurements system; the top Bragg reflector was determined to have a stress of ~ 230 MPa. The wafer was diced into ~ 3 cm^2 pieces prior to buckling to allow multiple tests of buckling on pieces without dome cavities. It was determined that a slow temperature ramp $\sim$ 50 °C/min, starting at room temperature up to a final temperature of 400 °C, was optimal to sufficiently induce buckling without

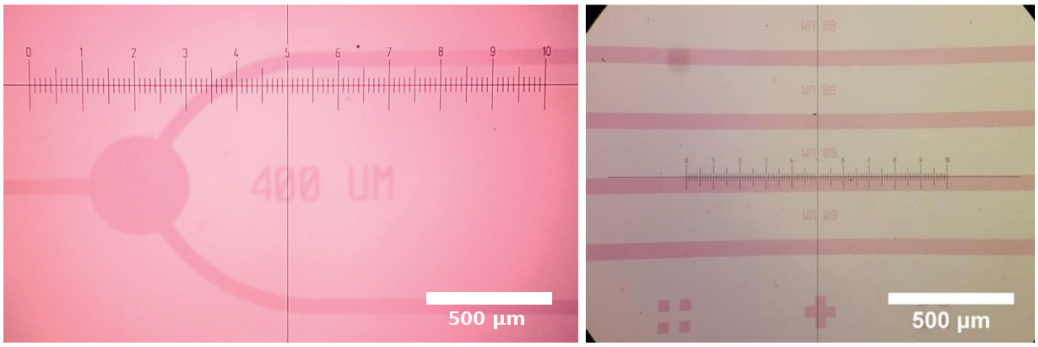

Figure 3.9: Patterned fluorocarbon low-adhesion layer. (a) Dome microcavity with intersecting waveguides and (b) straight edge waveguides.

resulting in full detachment of features. The pieces were then examined under an optical microscope to ensure complete and uniform buckling had occurred.

3.1.4 Morphology

The morphology of thin film buckles may be described using elastic buckling theory [123]. Ignoring plastic deformation of the top reflector, the critical buckling stress (σ_c), and the height of buckles may be predicted. For a circular delamination buckle, the critical buckling stress is given by $\sigma_c = 1.2235[E/(1-\nu^2](h/a)^2$, where E is the effective Young's modulus, ν is the Poisson's ratio, and h and a are the thickness and radius of the circular plate, respectively. For a given Bragg reflector, the effective Young's modulus, Poisson ratio, and thickness are all fixed, thus there is a minimum diameter D_{min} for which buckling may occur. Furthermore for $D > D_{\text{min}}$ the peak height of the circular buckle may be approximated as [123]:

$$\delta = h\left[1.9\left(\frac{\sigma}{\sigma_c} - 1\right)\right]^{1/2} \approx \left[\frac{1.9\sigma(1-\nu^2)}{1.2235E}\right]^{1/2}\frac{D}{2}, \tag{3.1}$$

where σ is the biaxial compressive stress of the top Bragg reflector. For $D \gg D_{\text{min}}$ the peak height increases approximately linearly with dome diameter, as predicted

by Eqn 3.1. However, it should be noted that this equation is only exact for $\sigma \approx \sigma_c$ and will overestimate the height for $\sigma/\sigma_c \gg 1$. Also, for $D \gg D_{\min}$, buckles tend to exhibit asymmetric shapes [123]. In this work, it was observed that for diameters greater than 400 μm, domes suffered from asymmetry. Domes of several diameters are shown in Figure 3.10; white light interference rings reveal the high degree of cylindrical symmetry for the smaller domes.

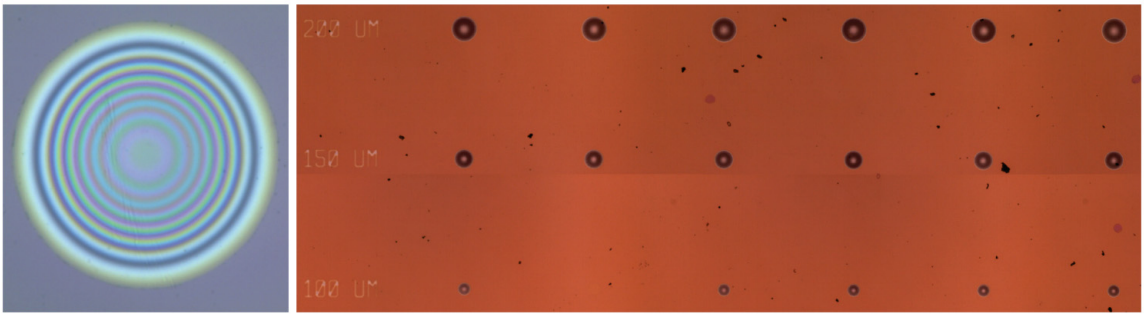

Figure 3.10: (a) Microscope image of a 100-μm base diameter dome cavity. White light interference fringes are clearly visible. (b) Microscope image of an array of dome cavities of various diameters (100, 150, and 200 μm).

The profile of the dome microcavities was measured using a non-contact optical profilometer (Zygo). A non-contact profilometer was preferred over a contact profilometer because the pressure from a scanning needle may deform the shape of the cavity. Effective film parameters for the top Bragg reflector were estimated using an effective medium approach. Young's modulus values of 40 GPa and 80 GPa, and Poisson ratio values of 0.17 and 0.20, were reported for SiO_2 and Ta_2O_5, respectively [124, 125, 126]. Effective medium parameters were approximated using an estimated composition of $\sim$ 60% SiO_2 and $\sim$ 40% Ta_2O_5, yielding parameters $E \sim 65$ GPa, $\nu \sim 0.2$, and $h \sim 2.3$ μm. From a Flexus measurement, the biaxial compressive stress of the top reflector was determined to be $\sigma \sim 230$ MPa. However, the stress at the moment of buckling was likely slightly less, as it has been shown previously that the stress tends to reduce during heating [90]. The height predictions from Eqn 3.1 were

plotted versus the experimentally measured height (averaged over $\sim$ 10 cavities) and show a good agreement, with slight deviation for large dome diameters as expected (see Figure 3.11).

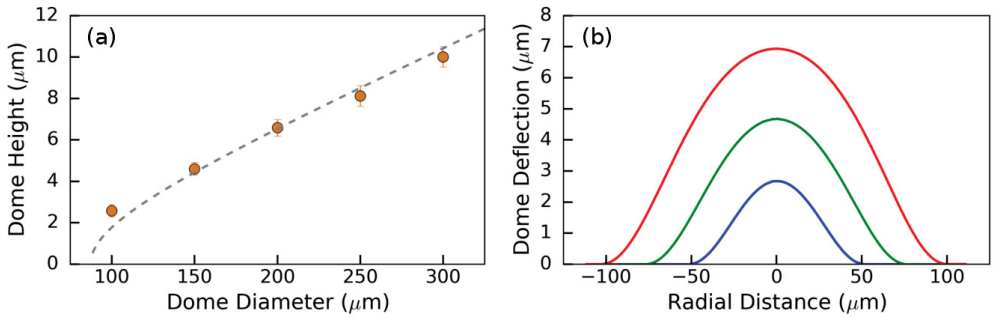

Figure 3.11: (a) Grey dotted line shows the dome height as a function of dome diameter as predicted by Eqn 3.1, using the film parameters described in the main text. The orange circles show experimentally determined heights, averaged over $\sim$10 cavities. (b) Experimentally measured (using a non-contact profilometer) profiles for 100, 150 and 200 μm base diameter cavities. The radius of curvature was determined through fitting a circular segment near the peak of the measured profiles, as described in the text.

For mode confinement, a key geometrical parameter is the radius of curvature of the top reflector. As shown in Chapter 2, the radius of curvature determines the spacing between transverse Hermite-Gaussian and Laguerre-Gaussian modes, and also the optical mode volume. A closed-form solution for the radius of curvature of buckled circular plates exists [127]. However, the experimental buckling of thin films typically involves plastic deformation at the clamped boundaries, further complicating the problem. Thus, to determine the radius of curvature, fits were performed to the data gathered from the optical profilometer. The fits were performed for a distance of $\pm$10 μm from the peak, in order to sample the portion of the mirror probed by the cavity mode. For 100, 150, and 200 μm domes, the radius of curvature was determined to be 210.0, 320.5, and 505.5 μm, respectively, and a full set of data is listed in Table 3.3.

Table 3.3: Predicted and measured optical and geometrical properties of dome microcavities of various base diameters. Note only a single 250 μm dome had optical resonances, and this specific cavity looked somewhat deformed likely resulting in its poor optical properties. Coupling Efficiency is described in Section 3.2.1.

Diameter (μm)	Average Dome Height (μm)	Measured Radius of Curvature (μm)	Predicted Mode Waist (μm)	Predicted $\Delta\lambda_T$ (nm)	Measured $\Delta\lambda_T$ (nm)	Estimated Coupling Efficiency	Average Cavity Decay (GHz)	Average Finesse	Average Mode Volume ($\lambda = 780nm$)
100	2.67	210	2.55	3.70	3.42	0.99	$2\pi \times 6.7$	3560	$35\lambda^3$
150	4.68	320	3.19	2.36	2.19	0.94	$2\pi \times 4.2$	3374	$89\lambda^3$
200	6.93	505	3.91	1.57	1.46	0.82	$2\pi \times 3.3$	3027	$191\lambda^3$
250	8.81	770	4.41	1.24	N/A	0.74	$2\pi \times 3.5$	2670	$255\lambda^3$
300	10.2	1040	4.97	0.97	0.94	0.64	$2\pi \times 2.7$	2925	$390\lambda^3$

3.2 Optical Properties

Chapter 2 introduced cavity quantum electrodynamics and explored the experimental requirements for the deterministic interaction between a single photon and a single atom within an optical cavity. First, the cavity must have a slow cavity decay rate (small κ), such that photons remain within the cavity for an extended period of time. Second, the cavity must have a small mode volume such that the atom-cavity coupling rate g is maximized. This section will explore and estimate these key parameters for the cavities described above.

3.2.1 Experimental Setup

Optical measurements were performed using the experimental setup shown in Figure 3.12. The chip was placed upon a copper heat sink, which was connected to a PID-controlled heater to enable temperature tuning. Liquid nitrogen could also be introduced in order to cool the heat sink down to cryogenic temperatures. Furthermore, the chamber could be sealed and evacuated such that measurements could be performed in vacuum. Finally, there are two glass ports that provide optical access to a device within the chamber. Optical resonances were examined by performing transmission spectroscopy using a fiber-coupled tunable diode laser (New Focus Velocity TLB6712). The laser was focused onto the microcavity using an objective lens (50×

Mitutoyo Plan APO) to a minimum spot size $\omega_l \approx 2.5$ μm. Transmitted light was captured using a second objective lens (100× Mitutoyo Plan APO SL) and directed towards a removable mirror. With the mirror in the path, the light is focused onto a ThorLabs CMOS camera and, with the mirror removed, the light is focused onto a photodiode (ThorLabs DET36A).

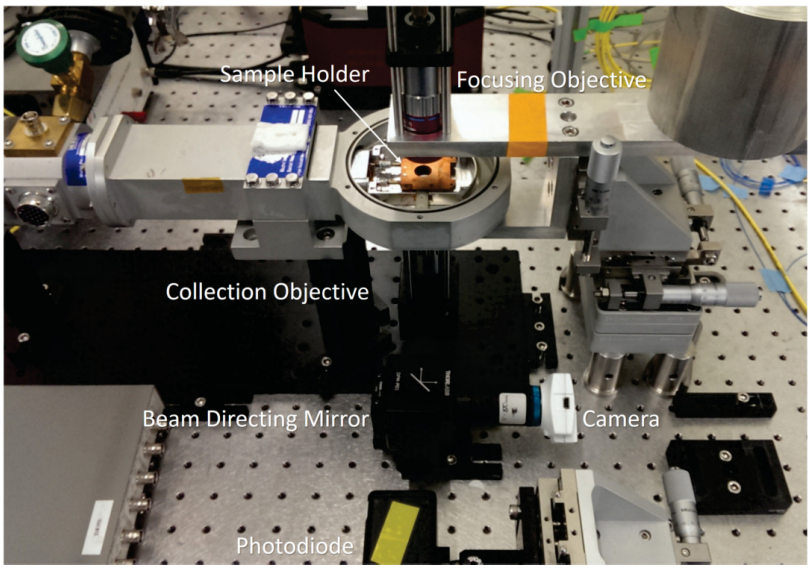

Figure 3.12: Experimental setup utilized for this work, as described in the main text.

To utilize these dome microcavities as quantum light matter interfaces requires the efficient coupling of photons into the cavity mode. The coupling efficiency may be approximated as follows [40]:

$$C_E = \left(\frac{2\omega_l \omega_0}{\omega_l^2 + \omega_0^2} \right)^2 . \tag{3.2}$$

This approximation assumes that the mode waist of the focusing optics and the cavity mode are aligned. Experimentally, coupling is maximized by slowly adjusting the top objective lens vertically until the transmitted signal is maximized, corresponding to maximal coupling. The coupling efficiency estimated by Eqn 3.2, and using the theoretically predicted mode waist for a 100 μm dome, is $C_E \approx 0.99$. However,

experimental imperfections likely reduce this significantly. The estimated coupling efficiencies for the remaining dome diameters are listed in Table 3.3.

Finally, optical measurements were made with the chamber evacuated to a base pressure of < 1 Torr. The cavities were able to survive the pump down, and during the pump down a slow drift of the resonance frequency was observed. As the environment within the chamber was removed the cavities experienced a red-shift in the optical resonance. This is possibly attributed to the cavity length increasing as a result of the reduction in atmospheric pressure on the top of the cavities. For example, the optical resonance of a particular 100 μm dome was found to shift from $\lambda_0 = 768.6$ nm to $\lambda_0 = 776.0$ nm as a result of the evacuation of the chamber. Upon returning the chamber to atmospheric conditions, the cavity resonances were observed to shift back to their original wavelength.

3.2.2 Optical Results

Buckled dome microcavities ranging in diameter from 100-300 μm were examined and optical properties were extracted. Chapter 2 explored the resonance condition and the types of modes that are supported within half-symmetric Fabry-Perot cavities. Two orthogonal sets of modes were described: Hermite-Gaussian modes $HG_{l,m}(x, y, z)$, where l and m are the integer mode orders, and Laguerre-Gaussian modes $LG_{p,l}(x, y, z)$, where p and l are the radial and azimuthal mode orders, respectively. Both Hermite-Gaussian and Laguerre-Gaussian modes were observed within these cavities, but the Laguerre-Gaussian modes were preferentially excited, suggesting a high degree of cylindrical symmetry. Nevertheless, by slightly misaligning the input laser, it was also typically possible to excite Hermite-Gaussian modes.

Using the setup shown in Figure 3.12, transmission spectra for several domes were measured. Results for a 150 μm and a 100 μm dome are shown in Figure 3.13. For both domes, the largest peak (at longer wavelength) is the fundamental optical

mode; the secondary peaks correspond to the higher-order transverse optical modes as determined by images captured by the CMOS camera. Higher-order modes with constant mode order sums:

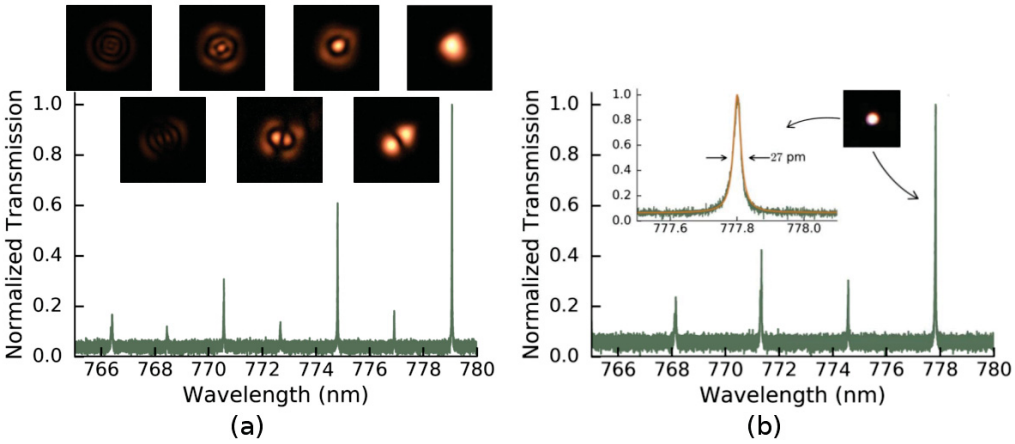

Figure 3.13: (a) Transmission spectra for a 150-μm diameter cavity, with a peak height of $\sim 4.7\mu$m. Mode images (captured using a CMOS camera) corresponding to each transmission peak are shown in the inset, (b) Transmission spectra for a 150-μm diameter cavity, with a peak height of $\sim 2.8\mu$m. The inset plot shows the fundamental resonance in greater detail.

$$g = l + m = 2p + l, \tag{3.3}$$

(i.e. constant g) are degenerate in frequency. The spacing between adjacent transverse modes, in the nearly planar limit ($R_c \gg \delta$) is given by [73]:

$$\Delta\lambda_T = \frac{\lambda^2}{2\pi z_0}\Delta g, \tag{3.4}$$

where z_0 is the Rayleigh range given by Eqn 2.26. The mode spacings predicted by Eqn 3.4, and the experimentally observed mode spacing are given in Table. 3.3, revealing good agreement. However, any slight asymmetry of the cavity will break this degeneracy between modes of constant g [88]. As an example, Figure 3.14 shows this degeneracy being split for a mode with $g = 4$, within a 150 μm cavity.

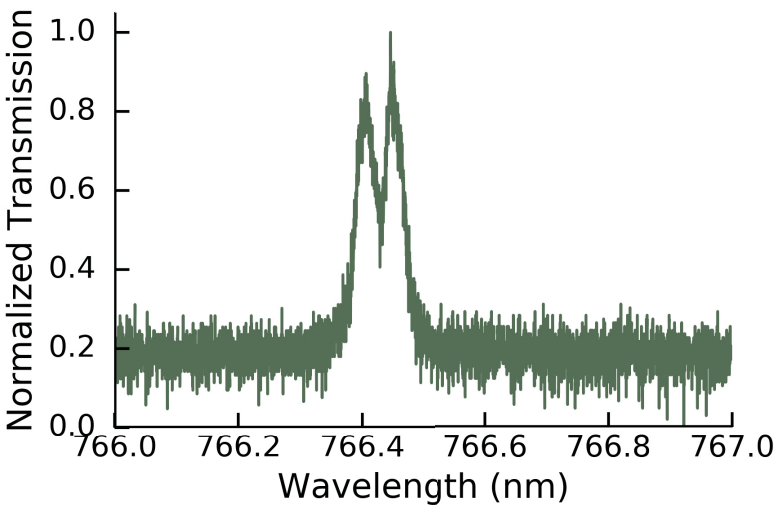

Figure 3.14: Transmission spectra for the fourth order transverse mode of a 150-μm diameter cavity. Mode splitting is clearly visible between two nominally degenerate modes.

Using the transmission spectra, it was possible to extract the line-width of the fundamental TEM_{00} optical mode for several dome diameters. The line-width is most often expressed as the half-width at half-max (HWHM) in terms of angular frequency $\kappa = \pi\nu_{1/2}$, which is known as the cavity decay rate. From the measurements described above, the cavity decay rate was determined to be $\kappa \approx 2\pi \times 6.7$ GHz for the 100 μm diameter domes and decreased to $\kappa \approx 2\pi \times 2.7$ GHz for 300 μm diameter cavities. Cavity decay rate and finesse are related by $\kappa = c\pi/2d\mathcal{F}$ [40], which may be derived from Eqn 2.14 and Eqn 2.15. Here d is the effective cavity length $d = \delta + 2d_p$, the geometrical length of the cavity is δ, and the penetration depth into the Bragg reflector is $d_p \approx (\lambda_0/2)(n_h - n_l)^{-1}$ [57]. The cavity finesse was observed to have a dependence on the dome diameter, possibly due to an increase in scattering losses in the larger cavities. Using the expression above, an effective cavity finesse of $\mathcal{F} \approx 3500$ was estimated for the 100 μm domes, and $\mathcal{F} \approx 2900$ was estimated for the 300 μm domes; these values were averaged over $5 - 10$ cavities per diameter. Note, only a single 250 μm cavity supported optical modes in the wavelength range of the laser.

These values are in good agreement with the predictions from the reflectivity of the mirrors $\mathcal{F}_R = 3500$, suggesting there exists little additional loss from surface defects within the cavities.

Finally, the optical mode volume was determined in two separate ways. Assuming a half-symmetric optical cavity, the mode volume of the TEM_{00} mode may be approximated as [40]:

$$V_m = \sqrt{\frac{\pi}{4}}\omega_0^2 d, \tag{3.5}$$

where ω_0 is the mode waist calculated using Eqn 2.25. The mode waist was estimated using the effective cavity length and the radius of curvature of the top mirror, and the values predicted were in good agreement with the experimentally observed waist size. For the smallest domes (100 μm base diameter) the optical mode volume was estimated to be $\sim 35\lambda^3$ for a wavelength of 780 nm. These results were compared with finite element COMSOL simulation of the optical mode; an example result for a 100 μm dome is shown in Figure 3.15.

The mode volume was extracted from the COMSOL simulations by performing the following integral over the electric field distribution [128]:

$$V_m = \int_V \frac{\epsilon(\bar{r})|\bar{E}(\bar{r})|^2}{\epsilon(\bar{r}_0)|\bar{E}(\bar{r}_0)|^2} d\bar{r}, \tag{3.6}$$

where $\epsilon(\bar{r})$ is the dielectric constant distribution, $\bar{E}(\bar{r})$ is the electric field distribution, and $\bar{r}_0$ is the location of the electric field maximum (i.e. an antinode of the cavity field). The resulting mode volume from this simulation was $V_m = 35.7\lambda^3$, which is in good agreement with the prediction from Eqn 3.5.

In summary, the various optical and geometrical properties estimated for various dome diameters are listed in Table. 3.3.

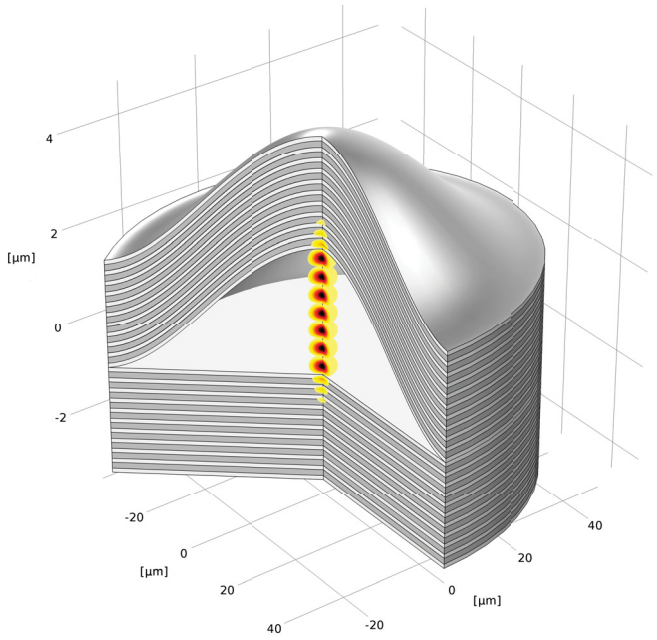

Figure 3.15: Cross-section of a finite element model of a 100 μm diameter microcavity (horizontal and vertical axes different scales) showing alternating SiO_2 (grey) and Ta_2O_5 (white) layers of the Bragg reflectors and a simulated optical mode.

3.3 Tuning

The buckling self-assembly process used to fabricate the optical cavities in this work is an inherently stochastic process. Variation in the local stress of the top reflector results in cavities that vary somewhat in height, even for the same base diameter. As a result, the resonant frequency is not predetermined by the base diameter, and the resonance frequencies have been observed to vary as a result of changes in the ambient temperature and pressure. Thus, in order to couple to the static transition frequency of atomic emitters, a method to tune and stabilize the resonance is required. For example, ^{87}Rb is a commonly used atomic emitter in cavity quantum electrodynamics experiments, and has an important transition at $\lambda = 780.24$ nm [35]. Therefore, a cavity must be tuned and locked onto this resonant wavelength on demand, and preferably on a device-by-device fashion [86].

3.3.1 Thermal Tuning

Previous work observed a drift in the resonance frequency as a result of heating caused by optical absorption [129]. This shift was a result of thermal expansion leading to an increase in cavity length, and thus a red-shift of the optical resonance. This thermal expansion was utilized as a means to tune the optical resonance through controlled heating [64]. The chips were placed upon a copper heat sink, and the chamber was evacuated to avoid thermalization by convection. A resistive heater within the copper block, controlled by a PID temperature controller, was used to increase the temperature in one degree Kelvin increments. The devices were given ten minutes to thermalize, since glass is a relatively poor conductor of heat. The resultant resonance peaks, and observed frequency shifts, are shown in Figure 3.16.

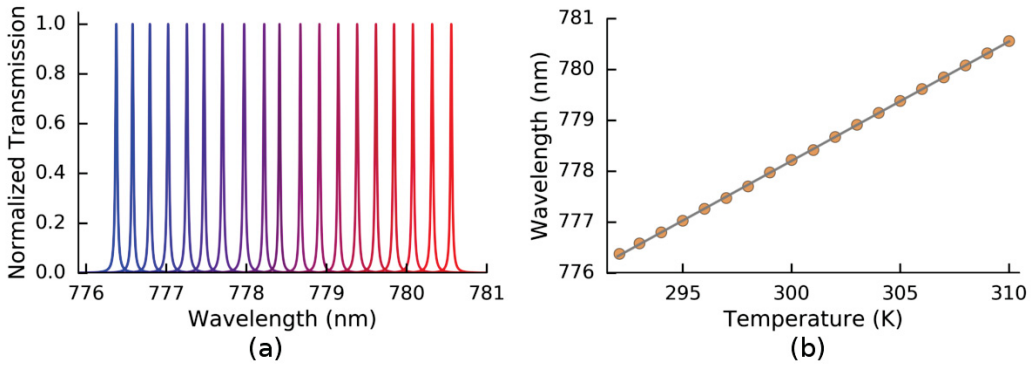

Figure 3.16: Fits of the experimental resonance peaks for the fundamental mode of a 100 μm diameter dome, at temperatures from 292 K (blue, 776.4 nm) to 310 K (red, 780.6 nm) in 1 K increments. (b) The variation of the fundamental resonance wavelength with temperature. Orange circles are experimental data points, and the grey line is a linear fit yielding a thermal tunability of $\Delta\lambda/\Delta T = 0.2346 \pm 0.0007$ nm/K. From [64].

A linear fit to the peak transmission wavelength reveals a temperature dependence of $\Delta\lambda/\Delta T = 0.2346 \pm 0.0007$ nm/K. However, the relatively slow dynamics of thermal expansion and contraction made it difficult to lock the cavity resonance to a single

wavelength for extended periods of time. Over the course of an hour the resonance wavelength varied by approximately ±50 pm about the set point.

3.3.2 Electrical Tuning

In an attempt to address the issues regarding the stable locking to a desired resonant wavelength, a second tuning approach was explored. Following a similar approach as Gierl et al. [130], electrodes were deposited below and above the dielectric stack and a bias voltage was applied to shorten the cavity via electrostatic forces. This work was performed with cavities with resonance frequencies in the infrared, however it should be straightforward to migrate this process to visible-range cavities if required. As a simplifying assumption, the complex geometry of the dome microcavity was approximated as a parallel-plate capacitor separated by the average distance of the two electrodes. Based on this, is possible to estimate the voltage required to tune the cavity by a single free spectral range. The force on a plate of a parallel plate capacitor is given by [131]:

$$F = \frac{\epsilon_0 \epsilon_r A V^2}{2d^2} = kx, \tag{3.7}$$

where ϵ_r is the effective dielectric constant between the plates, ϵ_0 is the permittivity of free space, V is the bias applied between the electrodes, A and d are the area and spacing between the electrodes, respectively, k is the spring constant of the dome microcavtiy (determined elsewhere [129]), and x is the desired distance the cavity is to be tuned. This equation may be rearranged to determine the voltage:

$$V = \sqrt{\frac{2d^2 kx}{\epsilon_0 \epsilon_r A}}. \tag{3.8}$$

For example, in order to tune the cavity by 500 nm, a voltage of approximately 165V would be required.

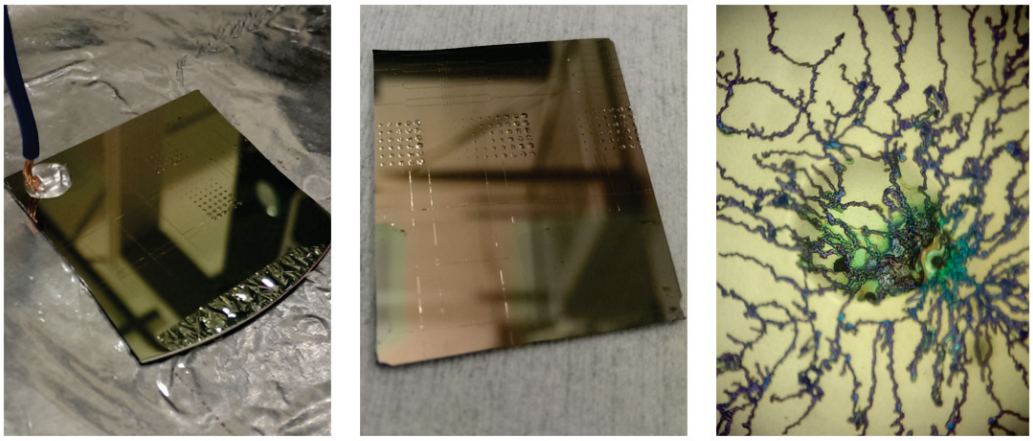

Figure 3.17: (a) Copper lead connected to bottom electrode using conductive epoxy. (b) Bare contacts, bottom contact in bottom right, and the top contact patterned on the remainder of the chip. (c) Dielectric breakdown as a result of exceeding the breakdown voltage of the Bragg reflector layers.

The fabrication of these cavities was nearly identical to the process described above. However, an additional 30 nm layer of titanium was deposited below the bottom Bragg reflector and on the top of the capping Bragg reflector. Also lower reflectance mirrors were utilized, producing broader resonance passbands. The bottom electrode was exposed using a lift-off procedure to remove a portion of the Bragg reflectors and access the bottom titanium layer, as shown in Figure 3.17b. Copper contacts were attached using conductive epoxy, providing good electrical contact to each electrode. The resistance between the top and bottom electrode was 1000-10000 Ω suggesting some leakage current was passing through the mirror layers. The bias was slowly increased from zero to one hundred volts. Note that a blue shift would be the expected result if the capacitor successfully pulled the plates closer; however, a red-shift was observed, suggesting Joule heating was dominating over the electrostatic force. A second attempt to rapidly apply the bias to see an electrostatic shift prior to the heating effects resulted in damage to the chip, as the high voltage caused electrical discharge though the dielectric layers (see Figure 3.17c).

The observed thermal tuning via Joule heating was explored further; two leads were attached to the top electrode of a second chip to allow a current to directly heat the top mirror rather than the entire chip. The resonance frequency was measured as a function of the applied voltage between the contacts and is plotted in Figure 3.18. As expected from Joule heating, the observed resonance frequency shift $\Delta\lambda$ was approximately proportional to the voltage squared, and thus the input power (see Figure 3.18b).

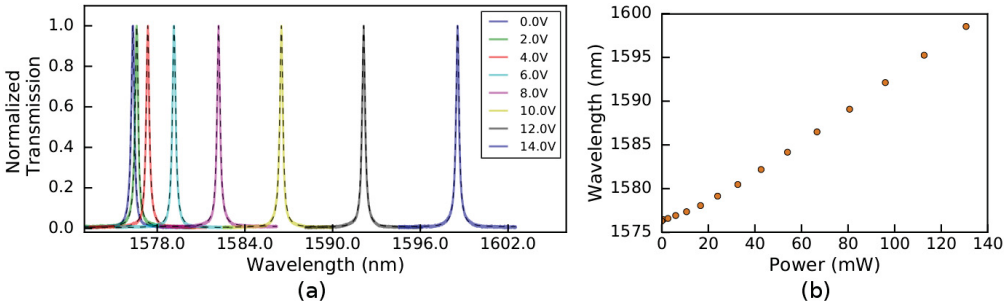

Figure 3.18: (a) Resonant wavelength of a 200-μm cavity as a function of applied voltage. The substrate of these devices was fused silica thus the additional substrate mode was suppressed compared to Figure B.1. (b) Resonant wavelength as a function of total power deposited onto the chip; power was calculated using $P = V^2/R$.

The ability to tune the optical resonance is crucial for cavity quantum electrodynamics. Furthermore, tuning individual cavities could have applications for tunable arrays of dye based lasers. Patterning electrodes that encircle individual domes could allow the on-demand tuning of multiple cavities in parallel.

Chapter 4

Cavity Quantum Electrodynamics with Dome Microcavities

The optical and geometrical properties of dome microcavities were examined in Chapter 3, and several key parameters such as the cavity decay rate κ and the optical mode volume V_m were extracted. As discussed in Chapter 2, these parameters are of particular interest for applications in cavity quantum electrodynamics. This chapter will use these extracted parameters to theoretically examine the viability of such cavities for future quantum applications.

It should be noted that the analysis in this chapter assumes a single atomic emitter, perfectly trapped at an anti-node of the cavity field. Several possible trapping methods are discussed, paving the way for future work aimed at the trapping of an atomic emitter within the optical cavity.

4.1 Cavity Quantum Electrodynamics Parameters

There exists two regimes of interest for cavity quantum electrodynamics: the *strong-coupled* regime characterized by $g > \kappa > \gamma$, and $C \gg 1$, and the *Purcell* regime characterized by $\kappa > g > \gamma$, and $C \gg 1$. The strong-coupled regime is perhaps the

most highly sought regime as it allows the reversible transfer of energy between the trapped atom and the cavity field [36]. Reversible energy transfers allows deterministic atom-photon interactions capable of coherent mapping of the polarization quantum state of a photon to the spin-state of an atom, and vice versa [49]. These coherent atom-photon interactions have made possible the development of basic quantum networks [51], the distribution of quantum entanglement between distant nodes [132], and the development of single photon quantum gates [52], all crucial elements for the future implementation of a large scale quantum network [16]. Strong-coupling has been demonstrated in several systems including single neutral atoms in high-finesse optical cavities [66], semiconductor quantum dots in a semiconductor microcavity [133], and superconducting circuits [134].

Nevertheless, systems within the Purcell regime are also of great interest for study, since they provide several important characteristics. For example, they enable an enhanced photon emission rate (of a trapped atomic emitter) into the cavity mode [83]. This enhanced emission has given rise to the notion of a one-dimensional atom, as described by Law et al. [47], since the photon emission is predominately into the cavity mode, which typically only covers a very small percentage of the solid angular space. Therefore, such devices show promise as highly efficient, on-demand single photon sources, required for the implementation of a large-scale quantum network.

Thus, initial investigations of dome microcavities should look into the two pertinent parameters; the strong-coupling parameter g/κ and the cooperativity C. As described in Chapter 2, the atom-cavity coupling rate g, and cooperativity C, can be defined as follows:

$$g = \sqrt{\frac{3\lambda^2 c\gamma}{4\pi V_m}}, \tag{4.1}$$

$$C = \frac{g^2}{2\kappa\gamma}. \tag{4.2}$$

See Chapter 2 for a more in-depth introduction to these parameters. As shown by Eqn 4.1, the atom-cavity coupling rate depends only on atomic parameters and the mode volume of the optical cavity. Therefore, for a given atom (e.g. ^{87}Rb) the coupling rate is strictly dependent on the optical mode volume of the cavity, since the polarization decay rate is constant, $\gamma = 2\pi \times 3.03$ MHz. From the values in Table 3.3, it is possible to estimate the maximum value expected for the atom-cavity coupling rate g. From this table, an average 100 μm dome is estimated to have an atom-cavity coupling rate $g \approx 2\pi \times 1.12$ GHz. This value is greater than the most optimistic predictions for macroscopic Fabry-Perot cavities [57], and among the highest predicted in the literature [40]. Table 4.1 presents the values for domes of varying base diameters, as determined from the values in Table 3.3.

Table 4.1: Atom-Cavity parameters extracted from the data within Table 3.3

Diameter (μm)	Atom-Cavity Coupling (GHz)	Cooperativity	Strong-Coupling Parameter	Extraction Efficiency
100	$2\pi \times 1.12$	32.3	0.17	0.98
150	$2\pi \times 0.70$	19.5	0.17	0.97
200	$2\pi \times 0.48$	11.6	0.15	0.96
250	$2\pi \times 0.41$	8.1	0.12	0.94
300	$2\pi \times 0.33$	7.0	0.12	0.93

Despite exhibiting high atom-cavity coupling, a more relevant parameter is the strong-coupling parameter g/κ. This effectively compares the rate at which photons irreversibly leak from the cavity (κ), with the rate of reversible transfer of energy quanta between the atom and the cavity (g). For the cavities explored in Chapter 3, a strong-coupling parameter $g/\kappa \lesssim 0.2$ was determined, placing such devices within the weakly coupled regime of cavity quantum electrodynamics. Furthermore, as seen in Figure 4.1, the strong-coupling parameter is nearly independent of the dome diam-

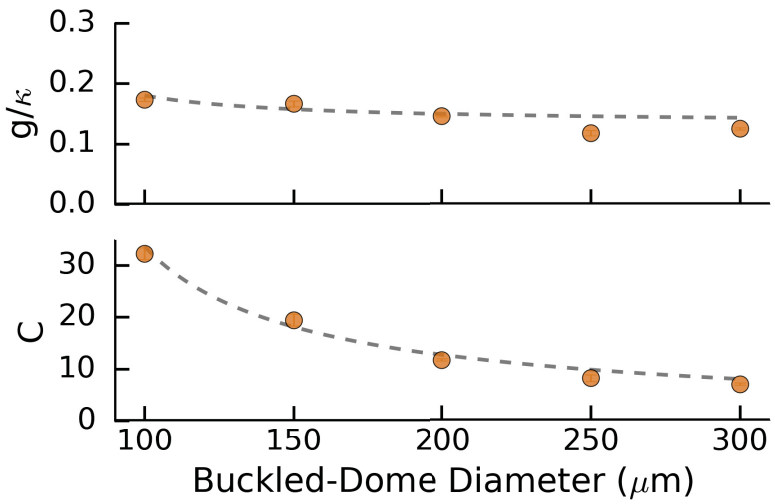

Figure 4.1: (a) Strong coupling parameter, g/κ, as a function of dome diameter. Fit (grey dashed line) derived using cavity finesse and optical profilometry measurements of dome height and radius of curvature. Deviations from the predicted zero-slope behavior are a result of the divergence from the elastic buckling model, producing a non-linear dependence between the radius of curvature and the dome diameter [129]. (b) Experimental cooperativity as a function of dome diameter. Fit as described in (a). Error bars, from the statistical uncertainty in κ and measurement uncertainty in R_c, are smaller than the symbol size. From [64].

eter, and therefore of the cavity length. The slight decrease with increasing diameter can be attributed to the reduced finesse observed in larger cavities. This is in contrast with the typical behavior observed in macroscopic cavities, where an increasing strong-coupling parameter with increasing cavity length has been reported [40]. It is interesting to consider the dependence of the strong-coupling parameter as a function of dome diameter. It can be shown that [64]:

$$\frac{g}{\kappa} \propto \frac{d}{\sqrt{V_m}}, \tag{4.3}$$

where $V_m \propto R_c^{1/2} d^{3/2}$, R_c is the radius of curvature of the cavity, and d is the cavity length. Furthermore, it has been shown previously based on elastic buckling theory (see Eqn 3.1) that the cavity length d is proportional to the base diameter D of

the dome cavity. Moreover, assuming that the buckled cavities are simply circular segments with peak height δ and base diameter D, to first order it may be shown that $R_c \propto D$ [63]. Given these approximations, Eqn 4.3 predicts that the strong-coupling parameter (to first order) is independent of the base diameter of the cavity. As shown in Figure 4.1, this is approximately true, with only a slight decrease for the largest cavities.

The second key parameter is the atom-cavity cooperativity C, as defined in Eqn. 4.2. Note that, in this expression, γ and κ are the half-width of the respective decay rates. The form presented by Law et al. [47] ($C = g^2/\kappa\gamma$), produces identical results, as in that case the atomic polarization decay rate γ is defined as the full-width value. These slightly different definitions are not always clearly distinguished in the literature. For consistency with most recent publications, the form used by Reiserer et al. [17] was adopted here, which defines γ as the half-width at half-max, $\gamma = 2\pi \times 3.03$ MHz. From Table 4.1, the average cooperativity for the 100μm cavities was determined to be $C = 32.3$. Thus, these cavities fall well inside the Purcell regime, shown in Figure 4.1. For comparison cooperativities of $C = 25$ and $C = 145$ have been reported for macroscopic [135] and fiber-based cavities [136], respectively. Furthermore, extending the analysis in reference [47], Cui et al. [137] were able to show that in the strong-coupled regime (they also extended their findings to the Purcell regime), the single photon extraction efficiency (or quantum efficiency) may be defined as:

$$\eta_q = \frac{g^2}{g^2 + \kappa\gamma}\frac{\kappa}{\kappa + \gamma} = \frac{2C}{2C + 1}\frac{\kappa}{\kappa + \gamma}. \tag{4.4}$$

From Eqn 4.4, the estimated extraction efficiency for the 100 μm cavities is found to be 0.98; the estimated extraction efficiencies for the other dome diameters are also listed in Table 4.1.

Notably, these results were obtained utilizing cavities fabricated with ten-period Bragg reflectors and exhibiting a modest reflection-limited finesse of 3500. In order to achieve strong coupling, and assuming the morphology of future cavities is similar to the current cavities, a minimum finesse of 21 000 would be required. This estimation was determined using the model employed for fitting the data in Figure 4.1. However, due to experimental uncertainties in the atom-cavity coupling rate, this should be considered as an absolute minimum requirement. This model also predicts a peak cooperativity $C = 210$ for a cavity finesse of 21 000, which would be among the highest reported to date [136]. Improved finesse may be achieved by utilizing a fifteen to eighteen period Bragg reflector in order to increase the mirror reflectance. Recent work on fiber-based cavities have reported an experimental finesse of 33 000 [58], and macroscopic cavities have reported finesse as high as 480 000 [57]. Note that both systems utilized SiO_2/Ta_2O_5 Bragg reflectors, as in the present work. However, the sputtering system used in this work tends to produce sub-optimal films after approximately eight periods, likely due to dielectric buildup within the chamber. Thus, it would be difficult to deposit films with the precision required to produce high quality, many-period Bragg reflectors with the equipment used to date. Future work might benefit from externally purchased depositions.

4.1.1 Atom-Cavity Simulations

The present work was focused mainly on the fabrication and characterization of Fabry-Perot cavities; coupling to an atomic species is left for future work. Nevertheless, simulations may provide insight to guide future experimental endeavors and provide context to the results described above. Below, an investigation using input-output theory [82, 138] was conducted to examine the transmission and reflection properties of the atom-cavity system. Second, single photon emission was examined using the quantum master equation [139].

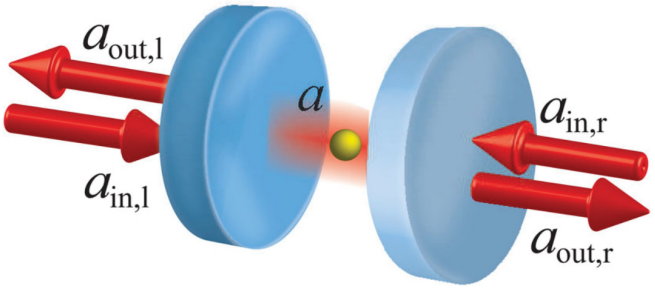

Figure 4.2: Cavity annihilation operators describing input-output theory, from [17].

The cavity decay rate κ is typically seen as an irreversible loss. However, experimental investigations of atom-cavity systems utilize this decay as a means to probe the system. An example is found in the framework of input-output theory which can be used to examine the response of the system to a weak coherent external drive [140, 141, 142]. For the cavities studied in this work, the cavity decay rate through the left and right mirror may be written as κ_l and κ_r, respectively, where we assume $\kappa_l = \kappa_r = \kappa/2$, since the two mirrors are nominally identical. The field operators for the incident electromagnetic field are given by $a_{in,l}$ ($a_{in,r}$), and for the outgoing field by $a_{out,l}$ ($a_{out,r}$), for the left (right) mirror, as shown in Figure 4.2. Here, a is the photon annihilation operator. In the Heisenberg picture of quantum mechanics (time-dependent operators) the relationship between the input and output modes is given by [143]:

$$a_{out,r}(t) + a_{in,r}(t) = \sqrt{2\kappa_r}a(t), \tag{4.5}$$

$$a_{out,l}(t) + a_{in,l}(t) = \sqrt{2\kappa_l}a(t), \tag{4.6}$$

where $a(t)$ is the intracavity field operator. Experimentally, the cavity will be driven from a single side (for example the left) and, in order to not saturate the atomic

emitter, the drive is assumed to be sufficiently weak such that (on average) less than one photon is within the cavity at all times. The dynamics of the atom-cavity system may be derived from the quantum master equation (Eqn 2.53), and the relationship $d/dt\langle\hat{A}\rangle = \mathrm{Tr}(\hat{A}\dot{\rho})$, and are as follows:

$$\langle\dot{a}\rangle = -\frac{i}{\hbar}\langle[a, \mathcal{H}_{JC}]\rangle - \kappa\langle a\rangle + \sqrt{2\kappa_l}\langle a_{in,l}\rangle(t), \tag{4.7}$$

$$\langle\dot{\sigma}_{ce}\rangle = -\frac{i}{\hbar}\langle[\sigma_{ce}, \mathcal{H}_{JC}]\rangle - \gamma\langle\sigma_{ce}\rangle \tag{4.8}$$

Here, $\langle A\rangle$ is the expectation value of an arbitrary operator A, $\mathcal{H}_{\mathrm{JC}}$ is the Jaynes-Cummings Hamiltonian given in Eqn. 2.48, γ is the atomic polarization decay rate, and σ_{ce} is the atomic lowering operator. These equations may be integrated numerically to solve for the dynamics of the system. However, for the special case of weak driving with a short pulse, an exact solution has been determined [144]. This solution provides an expression for the transmission and reflection coefficients as a function of the cavity (atomic) detuning, $\Delta_{c(a)} = \omega - \omega_{c(a)}$. Here, ω is the driving frequency, and $\omega_{c(a)}$ is the resonant frequency of the cavity (atom). The reflection and transmission coefficients may be written as follows:

$$r(\omega) = 1 - \frac{2\kappa_l(i\Delta_a + \gamma)}{(i\Delta_c + \kappa)(i\Delta_a + \gamma) + g^2}, \tag{4.9}$$

$$t(\omega) = \frac{2\sqrt{\kappa_l\kappa_r}(i\Delta_a + \gamma)}{(i\Delta_c + \kappa)(i\Delta_a + \gamma) + g^2}, \tag{4.10}$$

where g is the atom-cavity coupling rate, and the intensity reflectance and transmittance is given by $R(\omega) = |r(\omega)|^2$ and $T(\omega) = |t(\omega)|^2$, respectively.

For the 100 μm diameter cavities discussed in Section 3.2.2 the predicted transmission and reflection is shown in Figure 4.3, demonstrating the difference between

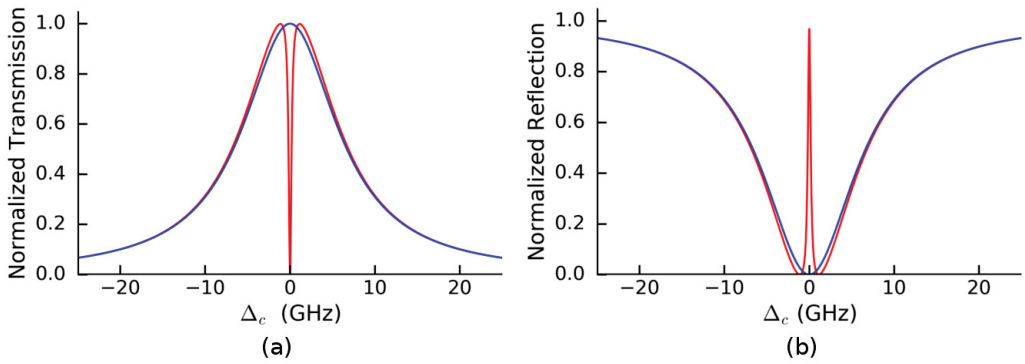

Figure 4.3: (a) Transmission spectra for an empty cavity with $\kappa = 2\pi \times 6.7$ GHz (blue), and for the same cavity coupled to a single atomic emitter with an atom-cavity coupling rate $g = 2\pi \times 1.12$ GHz (red). (b) Reflection spectra from the same cavity.

an empty cavity and the atom-cavity system. Figure 4.3 shows that even in the Purcell regime, a single atom strongly modifies the optical properties of a cavity. Future investigations of these cavities should look for this dip in transmission around zero detuning; the width of the transmission dip is dependent on the atom-cavity coupling rate. However, it should be noted that the splitting also depends on the number of atoms within the mode; thus, the atom-cavity coupling rate cannot simply be extracted from this plot without knowledge of the average number of atoms trapped within the cavity [66].

Finally, Reiserer and Rempe [17] suggested that the best-suited application for a cavity within the Purcell regime would be an on-demand single-photon source, due to the enhanced atomic decay rate into the cavity. To date, most single-photon sources rely on spontaneous emission events [145], or parametric down conversion [146]. Unfortunately, these processes are inherently random and thus are unable to produce photons "on-demand" as required for many quantum-network schemes [140]. A more advanced approach proposed by Law et al. [47] and further studied by Kuhn et al. [48, 147] uses a single atom coupled to an optical cavity to generate on-demand single photons. Furthermore, the cavity provides a preferential optical mode for

photon emission, such that the emitted photons will be automatically coupled into a well-defined direction.

This protocol utilizes a Λ-type three-level atom exhibiting two long-lived ground states, $|u\rangle$ and $|g\rangle$; the energy level diagram is shown in Figure 4.4. Typically these are hyperfine levels of the atomic ground state, and the third state is an electronically excited state $|e\rangle$. The photonic mode is described by the Fock state formalism with eigenstates $|0\rangle$ and $|1\rangle$, representing zero and one photon within the cavity, respectively. The cavity is tuned in resonance with the atomic transition frequency between the states $|e\rangle$ and $|g\rangle$, but must be far off-resonance with the transition $|e\rangle$ to $|u\rangle$. If ^{87}Rb is utilized, the hyperfine spacing between the ground states is 6.8 GHz, and therefore the cavity decay rate κ must be much less than this splitting. Unfortunately, even for the highest quality factor cavities studied here, the line-width is comparable to this splitting. Therefore, the development of higher finesse cavities will be paramount for future experimentation. Regardless, ignoring the inevitable additional coupling, the efficiency of single photon emission can be examined using the master equation approach [147].

To initialize the single photon generation scheme, the atom is prepared into the state $|u, 0\rangle$. The emission of the photon is induced using a classical trigger pulse, which has a free-space Rabi frequency, Ω_T, and is tuned to the transition frequency between $|u, 0\rangle$ and $|e, 0\rangle$. So long as this pulse rises sufficiently slowly, adiabatic passage of the atom from the state $|u, 0\rangle$ to $|g, 1\rangle$ will occur. The photon generated in this process will be emitted from the cavity through the partially reflecting mirrors. To ensure the photon emission from a pre-determined mirror, asymmetric cavities are typically utilized (with one mirror having higher reflectance), to promote leakage through the less reflective mirror.

A full description of this photon generation scheme is given in [147]; a brief description will be provided here. Assuming both the cavity and the trigger pulse

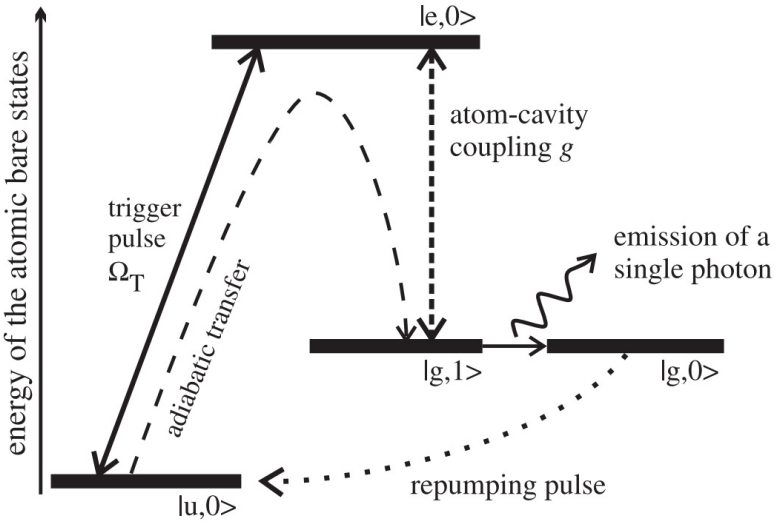

Figure 4.4: Atomic energy levels of a Λ-type atomic emitter. States $|e,0\rangle$ and $|g,1\rangle$ couple via an optical cavity, states $|e,0\rangle$ and $|u,0\rangle$ are coupled via a classical trigger pulse (From [147]).

are resonant with the desired transition, the interaction Hamiltonian in the basis of uncoupled states $\{|u,0\rangle, |e,0\rangle, |g,1\rangle\}$ is given by:

$$\mathcal{H} = -\frac{\hbar}{2}\begin{pmatrix} 0 & \Omega_T & 0 \\ \Omega_T^* & 0 & 2g \\ 0 & 2g^* & 0 \end{pmatrix}. \tag{4.11}$$

This Hamiltonian may be diagonalized into a new set of eigenstates (or dressed states) of the system as follows:

$$|a^0\rangle = \cos\Theta|u,0\rangle - \sin\Theta|g,1\rangle, \tag{4.12}$$

$$|a^+\rangle = \cos\Phi\sin\Theta|u,0\rangle - \sin\Phi|e,0\rangle + \cos\Phi\cos\Theta|g,1\rangle, \tag{4.13}$$

$$|a^-\rangle = \sin\Phi\sin\Theta|u,0\rangle + \cos\Phi|e,0\rangle + \sin\Phi\cos\Theta|g,1\rangle. \tag{4.14}$$

The mixing angles are defined as:

$$\tan\Theta = \frac{\Omega_T}{2g}, \tag{4.15}$$

$$\tan\Phi = \frac{\sqrt{4g^2+\Omega_T^2}}{\sqrt{4g^2+\Omega_T^2+\Delta^2}-\Delta}, \tag{4.16}$$

where Δ is the common detuning of the cavity and the trigger pulse, which is assumed to be zero for these simulations. When the trigger pulse is applied, the Hamiltonian and therefore the dressed states $\{|a^o\rangle, |a^+\rangle, |a^-\rangle\}$ evolve as a function of time. Given this evolution is sufficiently slow, the system will remain within its instantaneous eigenstate as prescribed by the adiabatic theorem [148].

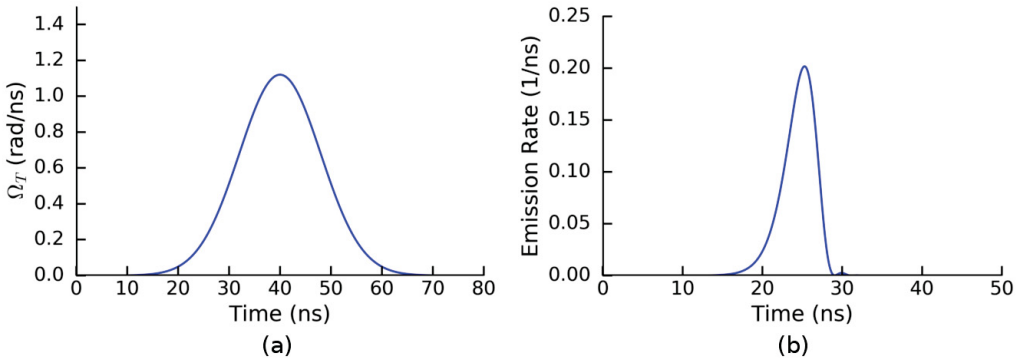

Figure 4.5: Numerical simulation of single-photon emission from a microcavity. (a) Time evolution of the trigger pulse $\Omega_T(t)$ utilized in the simulation. (b) Time evolution of the photon emission rate out of the cavity. The time integral of the emission rate reveals an emission probability of 97%.

The initial state of the system (prior to the trigger pulse) is characterized by a non-zero g and $\Omega_T = 0$, thus the mixing angle is $\tan\Theta = 0$. Therefore, an atom prepared in the state $|u, 0\rangle$ is equivalently in the dressed state $|a^0\rangle$. As the trigger pulse is applied, such that $\Omega_T \gg 2g$, the mixing angle evolves to $\tan\Theta \gg 1$, and thus the atom is transferred to the state $|g, 1\rangle$. In other words, the atom is adiabatically transferred between the two ground states without populating the excited state. The

photon that is generated in this process will then leak from the cavity and the system ends in the uncoupled state $|g,0\rangle$. This process has improved efficiency over the case in which the atom is simply excited to the state $|e,0\rangle$, since an atom in this state will spontaneously decay into one of the two ground states. If it happens to decay into the state $|u,0\rangle$, the emitted photon will be lost, since this transition is not coupled to the cavity mode, thereby reducing the efficiency of the single-photon source.

The time evolution of this system may be modeled using the quantum master equation given in Eqn. 2.53; for the system shown in Figure 4.5 it takes the form:

$$\frac{d}{dt}\rho = -\frac{i}{\hbar}[\mathcal{H},\rho] - \frac{1}{2}(\gamma_i+\gamma_j)\rho_{ij} + \delta_{ij}\sum_k \rho_{kk}A_{ki}, \tag{4.17}$$

where δ_{ij} is the Kronecker delta function, $\rho = |\psi\rangle\langle\psi|$ is the density matrix, $|\psi\rangle = (|U\rangle, |E\rangle, |G\rangle)$ is the state-vector of the bare atomic states, $\gamma_E = \gamma$, $\gamma_G = 2\kappa$, $\gamma_U = 0$, and A_{ik} are the Einstein coefficients. It is assumed that $A_{EU} = 1/2\gamma$ and that all others are equal to zero. The terms ρ_{ij} represents loss and damping of the system, whereas ρ_{kk} takes into account spontaneous emission. The photon emission rate is given by $2\kappa\rho_{GG}$, since once the system is in the state $|g,1\rangle$ the photon will leak from the cavity at a rate 2κ.

Consider the parameters determined in Section 4.1 for an average 100 μm cavity; $g = 2\pi\times 1.12$ GHz, $\kappa = 2\pi\times 6.7$ GHz, and $\gamma = 2\pi\times 3.0$ MHz. The Rabi frequency and shape of the trigger pulse is shown in Figure 4.5a, and the emission rate resulting from the application of said trigger is shown in Figure 4.5b. The probability of emitting a photon is given by the time-integral $P_{emiss} = \int 2\kappa\rho_{GG}dt$. Emission probability as a function of cavity line-width is plotted in Figure 4.6, and it can be seen that for $\kappa \approx 2g$ the emission probability is maximized, however for $\kappa > 2g$ the extraction efficiency is approximately constant. Furthermore, for the specific devices studied in this work, the emission probability is predicted to be $P_{emiss} \approx 0.97$, which is in good agreement with the estimation from Eqn 4.4 (see p.66). Furthermore, in regards

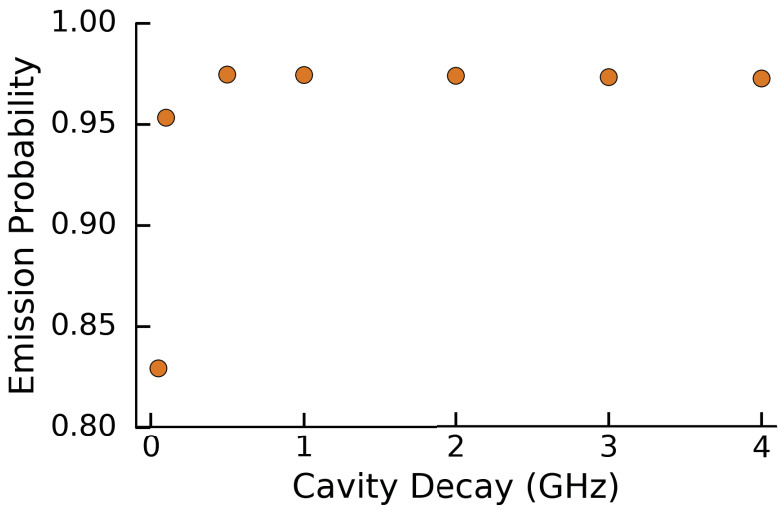

Figure 4.6: Emission probability determined using the quantum master equation simulation as a function of cavity decay rate κ. Atom-Cavity coupling rate was assumed to be $g = 2\pi \times 1.1$ GHz for these simulations. Emission probability sharply falls off for small cavity decay rate, as additional loss mechanisms start to dominate. For $\kappa > g/2$ extraction efficiency is approximately constant. Optimal operation regime would be $\kappa \approx g$, as extraction efficiency is maximized, while strong-coupling would also be achieved.

to the previously mentioned unwanted coupling to both hyperfine ground states, experimental uncertainly in the location of the trapped atom will likely result in a reduced atom-cavity coupling rate, likely to several hundreds of megahertz. Therefore, in order to maximize extraction efficiency, a cavity line-width on the order of 100 MHz should be a major goal for future work, in which case this unwanted coupling will become less of an issue. Moreover, as mentioned previously, in order to utilize these devices as single photon sources, atoms need to be injected and trapped within the cavity. Motivated by this several potential methods to provide open-access to the hollow cavities are discussed in the following section.

4.2 Open-Access

The experimental observations and applications described above can only be explored once an atomic species is introduced and preferably trapped within the cavity mode. The fabrication procedure described in Chapter 2 produces inherently closed cavities. However, the process may be augmented to provide open-access to the hollow cavity. Two approaches were investigated: first, FIB-milling was used to remove small portions of the top reflector, and second, fluorocarbon strips that intersected the cavities were deposited, allowing the simultaneous fabrication of hollow channels intersecting the hollow cavities.

4.2.1 FIB Milling

Focused ion beam (FIB) milling is a technique commonly used within the semiconductor industry for high precision material removal [149]. A FIB setup is similar to a scanning electron microscope. However, instead of accelerating electrons, a FIB uses a high energy stream of ions, typically gallium. The milling process results from the sputtering of the substrate by the flux of high-energy ions. This stream of ions may be guided with nanometer precision, accurately removing the desired areas on the substrate.

The FIB used in this work is housed at the National Institute for Nanotechnology (NINT) at the University of Alberta, and milling was performed with the assistance of Dr. Douglas Vick. The chip was initially investigated using a built-in scanning electron microscope to locate the desired devices, and in order to align the FIB. However, it was observed that a charge was building up on the dielectric chip, making it difficult to focus and resulting in a drift of the ion beam due to electrostatic repulsion. To avoid this issue, the chip was coated in $\sim$ 10 nm of carbon and attached to the chuck using conductive tape. This coating was thin enough to not be detrimental

to the optical resonances of the dome microcavities. Several cavities were optically tested and then selected to be milled. This provided a baseline optical measurement to compare following FIB processing. Open-access was provided by milling through the top mirror; several different hole shapes were milled as shown in Figure 4.7.

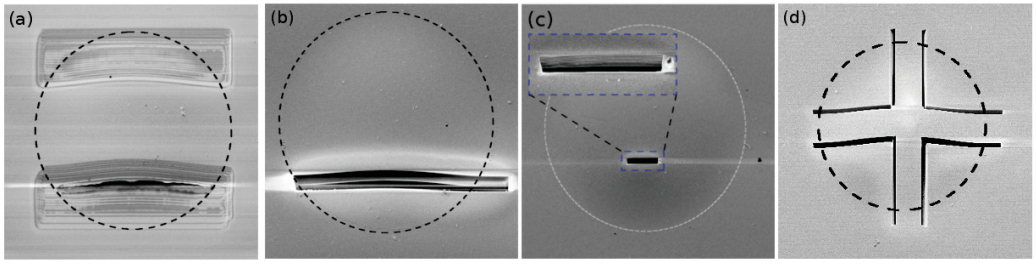

Figure 4.7: SEM images of several cavities provided with open-access via FIB-milling. In each case, the cavity is outlined to improve visibility.

Following the milling procedure, the cavities were again tested optically, to assess the effect of milling on the optical resonances. Several of the cavities had completely lost their optical resonances following the milling, likely due to the proximity of milling to the optical mode region, or due to build up of gallium on the reflectors. The cavity shown in Figure 4.7c retained optical resonances; however, the fundamental optical resonance was highly non-linear, even for low input power (< 1 μW), as shown in Figure 4.8a. This non-linearity is possibly attributable to optical absorption arising from gallium buildup on the Bragg reflectors. Interestingly, the optical resonance for the cavity in Figure 4.7a was largely unaffected, as shown in Figure 4.8b. However, its resonance wavelength was red-shifted by ~ 10 nm following the FIB milling. The optical resonance of this particular cavity was likely unaffected because the milling was relatively far from the location of the optical mode.

Despite the moderate success of the FIB milling process, it has several drawbacks. Open-access was provided to the cavities, and in some cases the optical properties were minimally affected. However, this procedure requires device-by-device fabrication, and one of the key motivations for the buckling approach is to avoid such

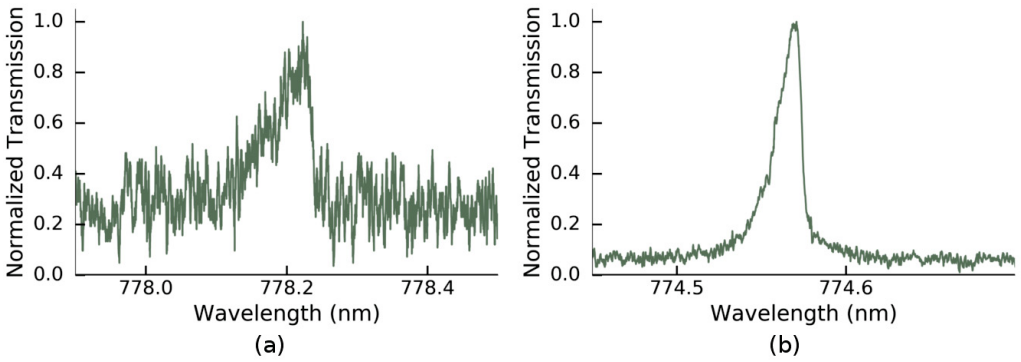

Figure 4.8: (a) Transmission spectra for the cavity shown in Figure. 4.7c. The non-linearity is possibly due to heating caused by optical absorption by implanted gallium. (b) Transmission spectra for the cavity shown in Figure. 4.7a, showing slightly non-linear behavior. However, the line-width was nearly identical to the pre-FIB measurement.

serial fabrication processing and instead utilize parallel fabrication of many devices simultaneously. Furthermore, in order to use these cavities as quantum interfaces; single atoms need to be trapped within the region of the optical mode. In early demonstrations [38], atoms were pre-cooled using a magneto-optical trap and allowed to fall through an optical cavity. Unfortunately, this transit only allows for interaction times on the order of 10 μs, barely long enough to examine the dynamics. Furthermore, the random nature of the atomic paths and arrival times makes this process non-deterministic. Additionally, as the atoms pass through the cavity, they still have relatively high kinetic energy and are subject to motion-induced dephasing and a time-dependent atom-cavity coupling rate $g(t)$. These issues have been resolved using additional trapping lasers in the form of standing wave dipole traps [150]. However, due to the geometry, it would be difficult to introduce trapping fields perpendicular to the cavity mode through the holes provided via FIB milling. Thus, preliminary investigation of a secondary potential method for trapping was made, involving on-chip hollow-core waveguides.

4.2.2 On-Chip Hollow Waveguides

As described above, an effective quantum light-matter interface should be capable of trapping an atomic species within the cavity mode region for a sufficiently long time. The first state-insensitive, neutral atom trap utilized within a cavity was a far-off resonance dipole trap (FORT) implemented via a standing wave along the cavity axis [151]. However, this approach was shown to be extremely susceptible to fluctuations of the optical intensity, causing heating and eventual loss of the trapped atomic species [152]. The intensity fluctuations were shown to be partly a result of acoustic vibrations of the cavity mirrors. Dome microcavities would be especially susceptible to such instability as the top reflector has been shown to support relatively high quality factor mechanical modes [129].

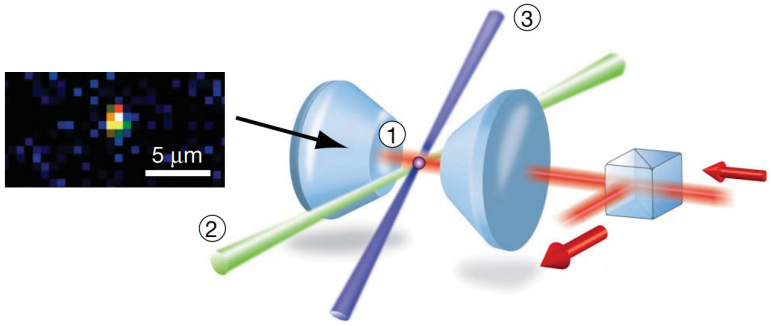

Figure 4.9: Single atom trapping using cavity-independent standing-wave dipole traps. (1) Single atom. (2) Far-detuned standing-wave dipole trap. (3) Classical trigger pulse. Inset, a fluorescence image of a trapped atom. Modified from [49].

This problem was circumvented recently by utilizing cavity-independent FORT; in this case, standing-wave traps were implemented perpendicular to the cavity mode, as shown in Figure 4.9. This method has demonstrated the trapping of neutral atoms for as long as one minute, likely limited only by collisions with room-temperature gas molecules [49, 150]. Furthermore, this method allows changing the position of the atom along the trap axis with sub-micron accuracy by shifting the standing wave [153]. As discussed above, the geometrical confinement would make such trapping

difficult for a cavities opened using FIB-milling. However, it may be possible to utilize on-chip waveguides to support such standing wave dipole traps.

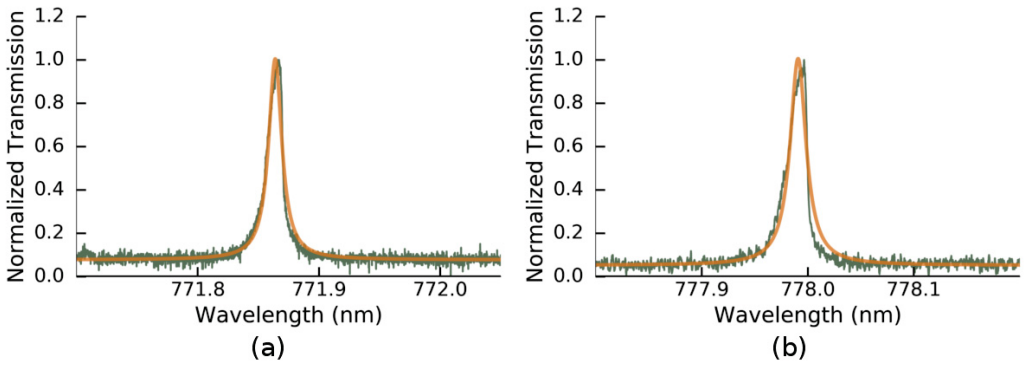

Figure 4.10: Transmission spectra for 200 μm cavities. (a) Cavity with no intersecting waveguides; measured quality factor of $\sim$55 000. (b) Cavity with intersecting waveguides; measured quality factor of $\sim$45 000.

Previous work has demonstrated low-loss hollow-core waveguides fabricated using an identical guided delamination procedure [91]. Intersecting such waveguides with dome microcavities might provide a means to produce a standing wave that crosses perpendicular to the cavity mode. Devices were fabricated with intersecting waveguides, as shown in Figure. 4.11. Unfortunately, the waveguides were not tall enough to support even the fundamental optical mode and thus could not be tested. To further investigate the optical properties of waveguides intersecting cavities, a new photo-lithography mask would need to be produced with $60-80$ μm wide waveguides [91]. In any case, the fabricated cavities were examined and were found to support optical modes with properties nearly identical to cavities without waveguides (see Figure 4.10). Since the optical mode lives at the center of the cavity, modifications of the dome periphery has minimal impact on the central part of the dome where the fundamental mode resides. Loading and examining atomic species is left for future work, but a hypothetical experimental setup may look as follows. A magneto-optical trap may be used to pre-cool a cloud of rubidium atoms, and a small number of atoms

may be dropped near the input facet of one of the waveguides. The atoms could be caught using a standing-wave dipole trap, and transported via the waveguide using an optical conveyor belt setup, as described in [154]. The atoms could then be examined while held within the optical cavity mode. This experimental setup will require many experimental advancements in both fabrication and design and implementation of the optics.

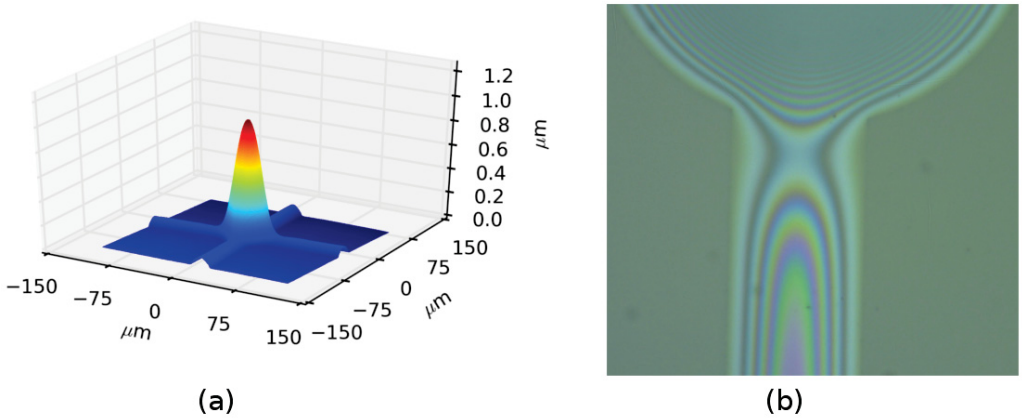

Figure 4.11: (a) Optical profilometer reconstruction of a 50μm cavity intersected by a pair of perpendicular 30 μm wide waveguides. (b) Microscope image of a 200 μm cavity intersected by a single 60 μm wide waveguide.

Chapter 5

Conclusions and Future Work

5.1 Summary

The primary focus of this thesis was to adapt the hollow microcavity buckling technique described in Ref. [63], for operation in the $\sim$ 780 nm wavelength range. This range may allow coupling to important transitions of alkali metal atoms such as rubidium, and has the added benefit of being compatible with many laser dyes [2] and fluorescent biological molecules [155], providing much scope for future work.

Chapter 3 outlined the fabrication technique utilized to construct the hollow cavities. A brief introduction to the sputter deposition procedure was provided, and the optical and mechanical properties of the thin film silicon dioxide and tantalum pentoxide films were described. The morphology of the dome microcavities of various diameters (ranging from 100 to 300 μm) was compared with predictions from elastic buckling theory, and good agreement was found. Optical transmission spectroscopy was performed to determine the optical quality factor and finesse. The measured finesse of the dome cavities was as high as 3560, which is in good agreement with the prediction of 3500 based on the estimated mirror reflectance. Furthermore, as a result of the high-degree of cylindrical symmetry, Laguerre-Gaussian modes were preferen-

tially excited even for high longitudinal mode orders. Hermite-Gaussian modes could also be observed by shifting the laser focus slightly. Finally, several tuning methods were explored to allow the wavelength to be shifted and locked to a desired wavelength on demand.

Chapter 4 utilized the optical characteristics determined in Chapter 3 to examine the viability of dome microcavities for cavity quantum electrodynamics. The atom-cavity coupling rate g was estimated using the optical mode volume. For the 100 μm diameter cavities, $g = 2\pi \times 1.12$ GHz was estimated, among the highest predicted to date in the literature. Discussions with Dr. Rempe from the Max Planck Institute for quantum optics [156] suggested operation in this regime could explore dynamics never before seen in an atom-cavity system, especially if the system is moved towards the ultra-strong coupled regime $g/\kappa \gg 1$. However, the specific cavities fabricated in this work exhibited a strong-coupling parameter $g/\kappa \lesssim 0.2$, and a cooperativity of ≈ 32, placing these devices in the Purcell regime of cavity quantum electrodynamics. These estimations were used to simulate the spectral properties of an atom-cavity system, as well as the single-photon generation probability. Finally, potential atomic delivery mechanisms were explored, by considering means to provide open access to the hollow cavity core. Two methods were attempted; first, FIB milling was used to remove portions of the top mirror showed has some success; however, a more promising direction might be the integration of hollow-core waveguides that intersect the hollow cavity.

Guided delamination buckling provides a novel fabrication technique for low mode volume, on-chip optical cavities. This monolithic process allows the production of tens of devices per square centimeter in parallel. Furthermore, the process was able to produce high quality factor cavities operating near the visible spectrum and exhibiting smooth reproducible features defined via standard lithographic and deposition techniques.

5.2 Future Work

The integration of hollow-core waveguides with the dome cavities might provide a direct means to introduce a liquid or gaseous analyte into the hollow cavity core. Previous attempts at microfluidic integration had limited success [157], however this was possibly due to the thin fluorocarbon layer coating the inner surfaces of the hollow structures. The hydrophobic nature of this fluorocarbon layer resists the introduction of water into the waveguides. If a method can be developed to remove this fluorocarbon layer following the delamination process, it may be easier to introduce fluids into these hollow structures. Unfortunately, teflon is non-reactive to most etchants, and harsh chemicals would likely damage the waveguide structures. However, it has been shown that the fluorocarbon used in this work begins to rapidly deteriorate when exposed to elevated temperatures, at a rate of ~ 1 nm/min at a temperature of 200°C. By cleaving a sample such that an open facet exists, annealing at an elevated temperature for an extended period of time should remove the fluorocarbon layer, leaving the bare tantalum pentoxide surfaces. The removal of the thin teflon coating should make microfluidics experiments somewhat easier to conduct.

Further exploration of cavity quantum electrodynamics has been discussed through-out the entirety of the thesis, but a brief summary will be given here. First, since strong-coupling is a highly sought goal, decreasing the line width of future cavities should be a primary goal. Linewidths on the order of 100 MHz are needed; thus, mirror reflectance must be greatly increased. In principle, this could be accomplished by increasing the number of periods in the Bragg reflectors. Work by Hood et al. [57] used cavities with eighteen and a half period mirrors, and achieved a cavity finesse of 480 000. Surprisingly, this value was greater than the predicted value determined from their transfer matrix simulations. Unfortunately, attempts to deposit mirrors with more than ten periods using the sputtering system in the NanoFab were unsuccessful, due to stability issues arising from a dielectric

film build-up within the chamber. Preliminary work suggested it may be possible to deposit a ten period mirror, and then have the chamber cleaned or deposit a thick layer of titanium followed by the deposition of the remaining eight periods. However, it would be preferable to deposit the entire mirror without having to break vacuum on the chamber, in order to avoid contamination on the substrate. Improvements to the finesse of future cavities may allow the investigation of a strong-coupled atom cavity system, opening many interesting research opportunities.

Finally, the introduction of atomic species should be another primary focus, to allow the production of a quantum light-matter interface. The most promising method for on-chip atom trapping involves the use of hollow-core waveguides. New cavities with intersecting waveguides would need to be produced, with taller waveguides to allow the investigation of the optical properties of waveguides intersecting a hollow cavity. Furthermore, it may be instructive to explore the use of standing waves within a straight waveguide in an attempt to control the location of an atom within the hollow-waveguide. Moreover, it may even be possible to use a single red-detuned trapping laser guided by the waveguide in concert with gravity, in order to catch a pre-cooled atom and guide them down a waveguide to the location of the cavity mode. The ultimate goal should be the repeatable and reliable loading of single atoms into the cavity, allowing a further exploration of cavity quantum electrodynamics.

Bibliography

[1] P Abgrall and AM Gue. Lab-on-chip technologies: making a microfluidic network and coupling it into a complete microsystema review. *Journal of Micromechanics and Microengineering*, 17(5):R15, 2007.

[2] Zhenyu Li, Zhaoyu Zhang, Teresa Emery, Axel Scherer, and Demetri Psaltis. Single mode optofluidic distributed feedback dye laser. *Optics Express*, 14(2):696–701, 2006.

[3] Holger Schmidt and Aaron R Hawkins. The photonic integration of non-solid media using optofluidics. *Nature photonics*, 5(10):598–604, 2011.

[4] Andrew Steane. Quantum computing. *Reports on Progress in Physics*, 61(2):117, 1998.

[5] Charles H Bennett, Ethan Bernstein, Gilles Brassard, and Umesh Vazirani. Strengths and weaknesses of quantum computing. *SIAM journal on Computing*, 26(5):1510–1523, 1997.

[6] Georges Ifrah, Edward Frank Harding, David Bellos, Sophie Wood, et al. *The universal history of computing: From the abacus to quantum computing*. John Wiley & Sons, Inc., 2000.

[7] Pieter Kok, William J Munro, Kae Nemoto, Timothy C Ralph, Jonathan P Dowling, and Gerard J Milburn. Linear optical quantum computing with photonic qubits. *Reviews of Modern Physics*, 79(1):135, 2007.

[8] Mika Hirvensalo. *Quantum computing*. Springer, 2013.

[9] MW Johnson, MHS Amin, S Gildert, T Lanting, F Hamze, N Dickson, R Harris, AJ Berkley, J Johansson, P Bunyk, et al. Quantum annealing with manufactured spins. *Nature*, 473(7346):194–198, 2011.

[10] Mohammad H Amin, Evgeny Andriyash, Jason Rolfe, Bohdan Kulchytskyy, and Roger Melko. Quantum boltzmann machine. *arXiv preprint arXiv:1601.02036*, 2016.

[11] Mohammad H Amin. Searching for quantum speedup in quasistatic quantum annealers. *Physical Review A*, 92(5):052323, 2015.

[12] Lieven MK Vandersypen, Matthias Steffen, Gregory Breyta, Costantino S Yannoni, Mark H Sherwood, and Isaac L Chuang. Experimental realization of shor's quantum factoring algorithm using nuclear magnetic resonance. *Nature*, 414(6866):883–887, 2001.

[13] Peter W Shor. Polynomial-time algorithms for prime factorization and discrete logarithms on a quantum computer. *SIAM review*, 41(2):303–332, 1999.

[14] Lov K Grover. A fast quantum mechanical algorithm for database search. In *Proceedings of the twenty-eighth annual ACM symposium on Theory of computing*, pages 212–219. ACM, 1996.

[15] S Somaroo, CH Tseng, TF Havel, Raymond Laflamme, and David G Cory. Quantum simulations on a quantum computer. *Physical review letters*, 82(26):5381, 1999.

[16] H Jeff Kimble. The quantum internet. *Nature*, 453(7198):1023–1030, 2008.

[17] Andreas Reiserer and Gerhard Rempe. Cavity-based quantum networks with single atoms and optical photons. *Rev. Mod. Phys.*, 87:1379–1418, Dec 2015.

[18] Dean Copsey, Mark Oskin, Francois Impens, Tzvetan Metodiev, Andrew Cross, Frederic T Chong, Isaac L Chuang, and John Kubiatowicz. Toward a scalable, silicon-based quantum computing architecture. *IEEE Journal of selected topics in quantum electronics*, 9(6):1552–1569, 2003.

[19] Akira Furusawa, Jens Lykke Sørensen, Samuel L Braunstein, Christopher A Fuchs, H Jeff Kimble, and Eugene S Polzik. Unconditional quantum teleportation. *Science*, 282(5389):706–709, 1998.

[20] Dik Bouwmeester, Jian-Wei Pan, Klaus Mattle, Manfred Eibl, Harald Weinfurter, and Anton Zeilinger. Experimental quantum teleportation. *Nature*, 390(6660):575–579, 1997.

[21] Peter W Shor and John Preskill. Simple proof of security of the bb84 quantum key distribution protocol. *Physical review letters*, 85(2):441, 2000.

[22] Lieven MK Vandersypen and Isaac L Chuang. Nmr techniques for quantum control and computation. *Reviews of modern physics*, 76(4):1037, 2005.

[23] Rainer Blatt and David Wineland. Entangled states of trapped atomic ions. *Nature*, 453(7198):1008–1015, 2008.

[24] L DiCarlo, JM Chow, JM Gambetta, Lev S Bishop, BR Johnson, DI Schuster, J Majer, A Blais, L Frunzio, SM Girvin, et al. Demonstration of two-qubit algorithms with a superconducting quantum processor. *Nature*, 460(7252):240–244, 2009.

[25] Stephanie Simmons, Richard M Brown, Helge Riemann, Nikolai V Abrosimov, Peter Becker, Hans-Joachim Pohl, Mike LW Thewalt, Kohei M Itoh, and John JL Morton. Entanglement in a solid-state spin ensemble. *Nature*, 470(7332):69–72, 2011.

[26] Mark Saffman, TG Walker, and Klaus Mølmer. Quantum information with rydberg atoms. *Reviews of Modern Physics*, 82(3):2313, 2010.

[27] PJJ O'Malley, R Babbush, ID Kivlichan, J Romero, JR McClean, R Barends, J Kelly, P Roushan, A Tranter, N Ding, et al. Scalable quantum simulation of molecular energies. *arXiv preprint arXiv:1512.06860*, 2015.

[28] John M Martinis. Qubit metrology for building a fault-tolerant quantum computer. *arXiv preprint arXiv:1510.01406*, 2015.

[29] Daniel Loss and David P DiVincenzo. Quantum computation with quantum dots. *Physical Review A*, 57(1):120, 1998.

[30] Jarryd J Pla, Kuan Y Tan, Juan P Dehollain, Wee H Lim, John JL Morton, David N Jamieson, Andrew S Dzurak, and Andrea Morello. A single-atom electron spin qubit in silicon. *Nature*, 489(7417):541–545, 2012.

[31] Julio T Barreiro, Philipp Schindler, Otfried Gühne, Thomas Monz, Michael Chwalla, Christian F Roos, Markus Hennrich, and Rainer Blatt. Experimental multiparticle entanglement dynamics induced by decoherence. *Nature Physics*, 6(12):943–946, 2010.

[32] DWave quantum computer. `http://www.dwavesys.com/`. Accessed: 2016-11-12.

[33] Arne Laucht, Rachpon Kalra, Stephanie Simmons, Juan P Dehollain, Juha T Muhonen, Fahd A Mohiyaddin, Solomon Freer, Fay E Hudson, Kohei M Itoh, David N Jamieson, et al. A dressed spin qubit in silicon. *arXiv preprint arXiv:1603.04800*, 2016.

[34] J Kelly, R Barends, AG Fowler, A Megrant, E Jeffrey, TC White, D Sank, JY Mutus, B Campbell, Yu Chen, et al. State preservation by repetitive error detection in a superconducting quantum circuit. *Nature*, 519(7541):66–69, 2015.

[35] Daniel A Steck. Rubidium 87 d line data, 2001.

[36] Tatjana Wilk, Simon C Webster, Axel Kuhn, and Gerhard Rempe. Single-atom single-photon quantum interface. *Science*, 317(5837):488–490, 2007.

[37] Manuel Uphoff, Manuel Brekenfeld, Gerhard Rempe, and Stephan Ritter. An integrated quantum repeater at telecom wavelength with single atoms in optical fiber cavities. *Applied Physics B*, 122(3):1–15, 2016.

[38] CJ Hood, MS Chapman, TW Lynn, and HJ Kimble. Real-time cavity qed with single atoms. *Physical review letters*, 80(19):4157, 1998.

[39] Hideo Mabuchi, Jun Ye, and H Jeff Kimble. Full observation of single-atom dynamics in cavity qed. *Applied Physics B*, 68(6):1095–1108, 1999.

[40] David Hunger, Tilo Steinmetz, Yves Colombe, Christian Deutsch, Theodor W Hänsch, and Jakob Reichel. A fiber fabry–perot cavity with high finesse. *New Journal of Physics*, 12(6):065038, 2010.

[41] Kerry J Vahala. Optical microcavities. *Nature*, 424(6950):839–846, 2003.

[42] Christian Junge, Danny OShea, Jürgen Volz, and Arno Rauschenbeutel. Strong coupling between single atoms and nontransversal photons. *Physical review letters*, 110(21):213604, 2013.

[43] TG Tiecke, Jeffrey Douglas Thompson, Nathalie Pulmones de Leon, LR Liu, V Vuletić, and Mikhail D Lukin. Nanophotonic quantum phase switch with a single atom. *Nature*, 508(7495):241–244, 2014.

[44] Jonathan D. Hood, Akihisa Goban, Ana Asenjo-Garcia, Mingwu Lu, Su-Peng Yu, Darrick E. Chang, and H. J. Kimble. Atomatom interactions around the band edge of a photonic crystal waveguide. *Proceedings of the National Academy of Sciences*, 113(38):10507–10512, 2016.

[45] SM Spillane, TJ Kippenberg, KJ Vahala, KW Goh, E Wilcut, and HJ Kimble. Ultrahigh-q toroidal microresonators for cavity quantum electrodynamics. *Physical Review A*, 71(1):013817, 2005.

[46] H Jeff Kimble, Mario Dagenais, and Leonard Mandel. Photon antibunching in resonance fluorescence. *Physical Review Letters*, 39(11):691, 1977.

[47] CK Law and HJ Kimble. Deterministic generation of a bit-stream of single-photon pulses. *Journal of Modern Optics*, 44(11-12):2067–2074, 1997.

[48] Axel Kuhn, Markus Hennrich, and Gerhard Rempe. Deterministic single-photon source for distributed quantum networking. *Physical review letters*, 89(6):067901, 2002.

[49] Holger P Specht, Christian Nölleke, Andreas Reiserer, Manuel Uphoff, Eden Figueroa, Stephan Ritter, and Gerhard Rempe. A single-atom quantum memory. *Nature*, 473(7346):190–193, 2011.

[50] Bernhard Weber, Holger P Specht, Tobias Müller, Jörg Bochmann, Martin Mücke, David L Moehring, and Gerhard Rempe. Photon-photon entanglement with a single trapped atom. *Physical review letters*, 102(3):030501, 2009.

[51] Stephan Ritter, Christian Nölleke, Carolin Hahn, Andreas Reiserer, Andreas Neuzner, Manuel Uphoff, Martin Mücke, Eden Figueroa, Joerg Bochmann, and Gerhard Rempe. An elementary quantum network of single atoms in optical cavities. *Nature*, 484(7393):195–200, 2012.

[52] Bastian Hacker, Stephan Welte, Gerhard Rempe, and Stephan Ritter. A photon-photon quantum gate based on a single atom in an optical resonator. *arXiv preprint arXiv:1605.05261*, 2016.

[53] Raju Valivarthi, Marcel Puigibert, Qiang Zhou, Gabriel H Aguilar, Varun B Verma, Francesco Marsili, Matthew D Shaw, Sae Woo Nam, Daniel Oblak, et al. Quantum teleportation across a metropolitan fibre network. *arXiv preprint arXiv:1605.08814*, 2016.

[54] A Goban, C-L Hung, S-P Yu, JD Hood, JA Muniz, JH Lee, MJ Martin, AC McClung, KS Choi, DE Chang, et al. Atom–light interactions in photonic crystals. *Nature communications*, 5, 2014.

[55] Andreas Muller, Edward B Flagg, John R Lawall, and Glenn S Solomon. Ultrahigh-finesse, low-mode-volume fabry–perot microcavity. *Optics letters*, 35(13):2293–2295, 2010.

[56] Christian Derntl, Michael Schneider, Johannes Schalko, Achim Bittner, Jörg Schmiedmayer, Ulrich Schmid, and Michael Trupke. Arrays of open, independently tunable microcavities. *Optics express*, 22(18):22111–22120, 2014.

[57] Christina J Hood, HJ Kimble, and Jun Ye. Characterization of high-finesse mirrors: Loss, phase shifts, and mode structure in an optical cavity. *Physical Review A*, 64(3):033804, 2001.

[58] Jose Gallego, Sutapa Ghosh, Seyed Khalil Alavi, Wolfgang Alt, Miguel Martinez-Dorantes, Dieter Meschede, and Lothar Ratschbacher. High-finesse fiber fabry–perot cavities: stabilization and mode matching analysis. *Applied Physics B*, 122(3):1–14, 2016.

[59] Claire Vallance, Aurelien AP Trichet, Dean James, Philip R Dolan, and Jason M Smith. Open-access microcavities for chemical sensing. *Nanotechnology*, 27(27):274003, 2016.

[60] Konstantin Ott, Sebastien Garcia, Ralf Kohlhaas, Klemens Schüppert, Peter Rosenbusch, Romain Long, and Jakob Reichel. Millimeter-long fiber fabry-perot cavities. *Optics express*, 24(9):9839–9853, 2016.

[61] Johannes FS Brachmann, Hanno Kaupp, Theodor W Hänsch, and David Hunger. Photothermal effects in ultra-precisely stabilized tunable microcavities. *Optics Express*, 24(18):21205–21215, 2016.

[62] Daniel Najer, Martina Renggli, Daniel Riedel, Sebastian Starosielec, and Richard J Warburton. Fabrication of mirror templates in silica with micron-sized radii of curvature. *arXiv preprint arXiv:1608.04527*, 2016.

[63] TW Allen, Josh Silverstone, N Ponnampalam, T Olsen, A Meldrum, and RG DeCorby. High-finesse cavities fabricated by buckling self-assembly of a-si/sio 2 multilayers. *Optics express*, 19(20):18903–18909, 2011.

[64] CA Potts, A Melnyk, H Ramp, MH Bitarafan, D Vick, LJ LeBlanc, JP Davis, and RG DeCorby. Tunable open-access microcavities for on-chip cavity quantum electrodynamics. *Applied Physics Letters*, 108(4):041103, 2016.

[65] H Angus Macleod. *Thin-film optical filters*. CRC press, 2001.

[66] RJ Thompson, G Rempe, and HJ Kimble. Observation of normal-mode splitting for an atom in an optical cavity. *Physical Review Letters*, 68(8):1132, 1992.

[67] Safa O Kasap. Optoelectronics and photonics: Principles and practices. 2001.

[68] CJR Sheppard. Approximate calculation of the reflection coefficient from a stratified medium. *Pure and Applied Optics: Journal of the European Optical Society Part A*, 4(5):665, 1995.

[69] Pochi Yeh. *Optical waves in layered media*, volume 61. Wiley-Interscience, 2005.

[70] Bahaa EA Saleh, Malvin Carl Teich, and Bahaa E Saleh. *Fundamentals of photonics*, volume 22. Wiley New York, 1991.

[71] Eugene Hecht. Optics, 4th. *International edition, Addison-Wesley, San Francisco*, 3, 2002.

[72] Hermite-gaussian. `http://www.optique-ingenieur.org/en/courses/OPI_ang_M01_C03/co/Contenu_13.html`. Accessed: 2016-11-12.

[73] Amnon Yariv. *Optical electronics*. Oxford University Press, USA, 1990.

[74] Simin Feng and Herbert G Winful. Physical origin of the gouy phase shift. *Optics letters*, 26(8):485–487, 2001.

[75] Laguerre-gaussian. `http://www.optique-ingenieur.org/en/courses/OPI_ang_M01_C03/co/Contenu_14.html`. Accessed: 2016-11-12.

[76] Ince-gaussian. `http://www.zemax.com/os/resources/learn/knowledgebase/modeling-high-order-laser-beams-in-zemax`. Accessed: 2016-11-12.

[77] SJ Van Enk and HJ Kimble. Single atom in free space as a quantum aperture. *Physical Review A*, 61(5):051802, 2000.

[78] Meng Khoon Tey, Zilong Chen, Syed Abdullah Aljunid, Brenda Chng, Florian Huber, Gleb Maslennikov, and Christian Kurtsiefer. Strong interaction between light and a single trapped atom without the need for a cavity. *Nature Physics*, 4(12):924–927, 2008.

[79] G Rempe, RJ Thompson, RJ Brecha, WD Lee, and HJ Kimble. Optical bistability and photon statistics in cavity quantum electrodynamics. *Physical Review Letters*, 67(13):1727, 1991.

[80] Serge Haroche and Jean-Michel Raimond. *Exploring the quantum: atoms, cavities, and photons*. Oxford university press, 2006.

[81] Edwin T Jaynes and Frederick W Cummings. Comparison of quantum and semiclassical radiation theories with application to the beam maser. *Proceedings of the IEEE*, 51(1):89–109, 1963.

[82] Crispin W Gardiner and Hermann Haken. *Quantum noise*, volume 26. Springer Berlin, 1991.

[83] QA Turchette, RJ Thompson, and HJ Kimble. One-dimensional atoms. *Applied physics B-lasers and optics*, 60(2-3):S1–S10, 1995.

[84] Charles Fabry and Alfred Perot. Theorie et applications dune nouvelle methode de spectroscopie interferentielle. *Ann. Chim. Phys*, 16(7):115, 1899.

[85] E Jesper Eklund and Andrei M Shkel. Factors affecting the performance of micromachined sensors based on fabry–perot interferometry. *Journal of Micromechanics and Microengineering*, 15(9):1770, 2005.

[86] P Tayebati, P Wang, M Azimi, L Maflah, and D Vakhshoori. Microelectromechanical tunable filter with stable half symmetric cavity. *Electronics Letters*, 34(20):1967–1968, 1998.

[87] Lukas Greuter, Sebastian Starosielec, Daniel Najer, Arne Ludwig, Luc Duempelmann, Dominik Rohner, and Richard J. Warburton. A small mode volume tunable microcavity: Development and characterization. *Applied Physics Letters*, 105(12), 2014.

[88] Philip R. Dolan, Gareth M. Hughes, Fabio Grazioso, Brian R. Patton, and Jason M. Smith. Femtoliter tunable optical cavity arrays. *Opt. Lett.*, 35(21):3556–3558, Nov 2010.

[89] Ray G DeCorby, Nakeeran Ponnampalam, Mahesh M Pai, Hue T Nguyen, Prabhat K Dwivedi, Thomas J Clement, Chris J Haugen, Jim N McMullin, and Safa O Kasap. High index contrast waveguides in chalcogenide glass and polymer. *IEEE Journal of selected topics in quantum electronics*, 11(2):539–546, 2005.

[90] E Epp, N Ponnampalam, W Newman, B Drobot, JN McMullin, AF Meldrum, and RG DeCorby. Hollow bragg waveguides fabricated by controlled buckling of si/sio 2 multilayers. *Optics express*, 18(24):24917–24925, 2010.

[91] A Melnyk, CA Potts, TW Allen, and RG DeCorby. Visible-range hollow waveguides by guided buckling of ta 2 o 5/sio 2 multilayers. *Applied optics*, 55(13):3645–3649, 2016.

[92] Werner Kern. *Thin film processes II*, volume 2. Academic press, 2012.

[93] Krishna Seshan. *Handbook of thin film deposition*. William Andrew, 2012.

[94] John E Mahan. Physical vapor deposition of thin films. *Physical Vapor Deposition of Thin Films, by John E. Mahan, pp. 336. ISBN 0-471-33001-9. Wiley-VCH, January 2000.*, page 336, 2000.

[95] Mark J Hampden-Smith and Toivo T Kodas. Chemical vapor deposition of metals: Part 1. an overview of cvd processes. *Chemical Vapor Deposition*, 1(1):8–23, 1995.

[96] J Singh and DE Wolfe. Review nano and macro-structured component fabrication by electron beam-physical vapor deposition (eb-pvd). *Journal of materials Science*, 40(1):1–26, 2005.

[97] DW Hoffman. Perspective on stresses in magnetron-sputtered thin films. *Journal of Vacuum Science & Technology A*, 12(4):953–961, 1994.

[98] PJ Kelly and RD Arnell. Magnetron sputtering: a review of recent developments and applications. *Vacuum*, 56(3):159–172, 2000.

[99] Sputtering process. `http://lnf-wiki.eecs.umich.edu/wiki/Sputter_deposition`. Accessed: 2016-11-12.

[100] Lambert Ben Freund and Subra Suresh. *Thin film materials: stress, defect formation and surface evolution*. Cambridge University Press, 2004.

[101] Angela Piegari and François Flory. *Optical thin films and coatings: From materials to applications*. Elsevier, 2013.

[102] G Bräuer, B Szyszka, Michael Vergöhl, and R Bandorf. Magnetron sputtering–milestones of 30 years. *Vacuum*, 84(12):1354–1359, 2010.

[103] André Anders. Physics of arcing, and implications to sputter deposition. *Thin Solid Films*, 502(1):22–28, 2006.

[104] G Bräuer, J Szczyrbowski, and G Teschner. New approaches for reactive sputtering of dielectric materials on large scale substrates. *Journal of non-crystalline solids*, 218:19–24, 1997.

[105] J Sellers. Asymmetric bipolar pulsed dc: the enabling technology for reactive pvd. *Surface and coatings technology*, 98(1):1245–1250, 1998.

[106] Diederik Depla, Stijn Mahieu, et al. *Reactive sputter deposition*. Springer, 2008.

[107] William D Sproul, David J Christie, and Dan C Carter. Control of reactive sputtering processes. *Thin solid films*, 491(1):1–17, 2005.

[108] Jeff C Sellers. The disappearing anode myth: strategies and solutions for reactive pvd from single magnetrons. *Surface and Coatings Technology*, 94:184–188, 1997.

[109] Aaron Melnyk. Fabrication of visible range hollow bragg waveguides. Master's thesis, University of Alberta, 4 2016.

[110] S-I Jun, TE McKnight, AV Melechko, ML Simpson, and PD Rack. Characterisation of reactively sputtered silicon oxide for thin-film transistor fabrication. *Electronics Letters*, 41(14):822–823, 2005.

[111] Jolanta E Klemberg-Sapieha, Jörg Oberste-Berghaus, Ludvik Martinu, Richard Blacker, Ian Stevenson, George Sadkhin, Dale Morton, Scott McEldowney, Robert Klinger, Phil J Martin, et al. Mechanical characteristics of optical coatings prepared by various techniques: a comparative study. *Applied optics*, 43(13):2670–2679, 2004.

[112] J-Y Kim, E Barnat, EJ Rymaszewski, and T-M Lu. Frequency-dependent pulsed direct current magnetron sputtering of titanium oxide films. *Journal of Vacuum Science & Technology A*, 19(2):429–434, 2001.

[113] PS Henderson, PJ Kelly, RD Arnell, H Bäcker, and JW Bradley. Investigation into the properties of titanium based films deposited using pulsed magnetron sputtering. *Surface and Coatings Technology*, 174:779–783, 2003.

[114] Pushkar Jain, Jasbir S Juneja, Vinay Bhagwat, Eugene J Rymaszewski, Toh-Ming Lu, and Timothy S Cale. Effects of substrate temperature on properties of pulsed dc reactively sputtered tantalum oxide films. *Journal of Vacuum Science & Technology A*, 23(3):512–519, 2005.

[115] M-W Moon, K-R Lee, Kyu-Hwan Oh, and John W Hutchinson. Buckle delamination on patterned substrates. *Acta Materialia*, 52(10):3151–3159, 2004.

[116] HS Khoo, TW Huang, YF Chen, MH Chen, TH Hsu, and FG Tseng. Improved hydrophobicity of vapor coated chlorosilane self assembled monolayers using evaporative drying of solvent and annealing. In *TRANSDUCERS 2007-2007 International Solid-State Sensors, Actuators and Microsystems Conference*, pages 1629–1632. IEEE, 2007.

[117] Bharat Bhushan, Huiwen Liu, and Stephen M Hsu. Adhesion and friction studies of silicon and hydrophobic and low friction films and investigation of scale effects. *Journal of tribology*, 126(3):583–590, 2004.

[118] RG DeCorby, N Ponnampalam, HT Nguyen, MM Pai, and TJ Clement. Guided self-assembly of integrated hollow bragg waveguides. *Optics express*, 15(7):3902–3915, 2007.

[119] Arun Kumar Gnanappa, Cian O'Murchu, Orla Slattery, Frank Peters, Balázs Aszalós-Kiss, and Syed AM Tofail. Effect of annealing on hydrophobic stability of plasma deposited fluoropolymer coatings. *Polymer Degradation and Stability*, 93(12):2119–2126, 2008.

[120] Yuta Suzuki, Haojie Fu, Yoshio Abe, and Midori Kawamura. Effects of substrate temperature on structure and mechanical properties of sputter deposited fluorocarbon thin films. *Vacuum*, 87:218–221, 2013.

[121] AA Ayón, D-Z Chen, R Khanna, R Braff, HH Sawin, and MA Schmidt. A novel integrated mems process using fluorocarbon films deposited with a deep reactive ion etching (drie) tool. In *MRS Proceedings*, volume 605, page 141. Cambridge Univ Press, 1999.

[122] Yan Xin Zhuang and Aric Menon. Wettability and thermal stability of fluorocarbon films deposited by deep reactive ion etching. *Journal of Vacuum Science & Technology A*, 23(3):434–439, 2005.

[123] JW Hutchinson, MD Thouless, and EG Liniger. Growth and configurational stability of circular, buckling-driven film delaminations. *Acta metallurgica et materialia*, 40(2):295–308, 1992.

[124] Chuen-Lin Tien, Cheng-Chung Lee, Kie-Pin Chuang, and Cheng-Chung Jaing. Simultaneous determination of the thermal expansion coefficient and the elastic modulus of ta2o5 thin film using phase shifting interferometry. *Journal of Modern Optics*, 47(10):1681–1691, 2000.

[125] DRM Crooks, G Cagnoli, MM Fejer, G Harry, J Hough, BT Khuri-Yakub, S Penn, R Route, S Rowan, PH Sneddon, et al. Experimental measurements of mechanical dissipation associated with dielectric coatings formed using sio2, ta2o5 and al2o3. *Classical and Quantum Gravity*, 23(15):4953, 2006.

[126] William D Nix. Mechanical properties of thin films. *Metallurgical transactions A*, 20(11):2217–2245, 1989.

[127] Y Yu, IA Ashcroft, and G Swallowe. An experimental investigation of residual stresses in an epoxy–steel laminate. *International journal of adhesion and adhesives*, 26(7):511–519, 2006.

[128] Oskar Painter, RK Lee, Axel Scherer, A Yariv, JD O'brien, PD Dapkus, and I Kim. Two-dimensional photonic band-gap defect mode laser. *Science*, 284(5421):1819–1821, 1999.

[129] MH Bitarafan, H Ramp, TW Allen, C Potts, X Rojas, AJR MacDonald, JP Davis, and RG DeCorby. Thermomechanical characterization of on-chip buckled dome fabry–perot microcavities. *JOSA B*, 32(6):1214–1220, 2015.

[130] Christian Gierl, Karolina Zogal, Hooman A Davani, and Peter Meissner. Electro thermal and electro statical actuation of a surface micromachined tunable fabry-pérot filter. In *CLEO: Applications and Technology*, page JTuI73. Optical Society of America, 2011.

[131] David Jeffrey Griffiths and Reed College. *Introduction to electrodynamics*, volume 3. prentice Hall Upper Saddle River, NJ, 1999.

[132] Christian Nölleke, Andreas Neuzner, Andreas Reiserer, Carolin Hahn, Gerhard Rempe, and Stephan Ritter. Efficient teleportation between remote single-atom quantum memories. *Physical review letters*, 110(14):140403, 2013.

[133] JP Reithmaier, G Sek, A Löffler, C Hofmann, S Kuhn, S Reitzenstein, LV Keldysh, VD Kulakovskii, TL Reinecke, and A Forchel. Strong coupling in a single quantum dot–semiconductor microcavity system. *Nature*, 432(7014):197–200, 2004.

[134] Andreas Wallraff, David I Schuster, Alexandre Blais, L Frunzio, R-S Huang, J Majer, S Kumar, Steven M Girvin, and Robert J Schoelkopf. Strong coupling of a single photon to a superconducting qubit using circuit quantum electrodynamics. *Nature*, 431(7005):162–167, 2004.

[135] JA Sauer, KM Fortier, MS Chang, CD Hamley, and MS Chapman. Cavity qed with optically transported atoms. *Physical Review A*, 69(5):051804, 2004.

[136] Yves Colombe, Tilo Steinmetz, Guilhem Dubois, Felix Linke, David Hunger, and Jakob Reichel. Strong atom–field coupling for bose–einstein condensates in an optical cavity on a chip. *Nature*, 450(7167):272–276, 2007.

[137] Guoqiang Cui and MG Raymer. Emission spectra and quantum efficiency of single-photon sources in the cavity-qed strong-coupling regime. *Physical Review A*, 73(5):053807, 2006.

[138] HJ Carmichael. Quantum trajectory theory for cascaded open systems. *Physical review letters*, 70(15):2273, 1993.

[139] CW Gardiner and MJ Collett. Input and output in damped quantum systems: Quantum stochastic differential equations and the master equation. *Physical Review A*, 31(6):3761, 1985.

[140] Juan Ignacio Cirac, Peter Zoller, H Jeff Kimble, and Hideo Mabuchi. Quantum state transfer and entanglement distribution among distant nodes in a quantum network. *Physical Review Letters*, 78(16):3221, 1997.

[141] Howard J Carmichael and Marlan O Scully. Statistical methods in quantum optics 1: Master equations and fokker-planck equations. *Physics Today*, 53(3):78, 2000.

[142] Daniel F Walls and Gerard J Milburn. *Quantum optics*. Springer Science & Business Media, 2007.

[143] G. S. Agarwal. *Quantum optics*. Cambridge University Press, Cambridge, England, 2013.

[144] CY Hu, A Young, JL OBrien, WJ Munro, and JsG Rarity. Giant optical faraday rotation induced by a single-electron spin in a quantum dot: applications to entangling remote spins via a single photon. *Physical Review B*, 78(8):085307, 2008.

[145] Matthew Pelton, Charles Santori, Jelena Vucković, Bingyang Zhang, Glenn S Solomon, Jocelyn Plant, and Yoshihisa Yamamoto. Efficient source of single photons: a single quantum dot in a micropost microcavity. *Physical review letters*, 89(23):233602, 2002.

[146] Brahim Lounis and Michel Orrit. Single-photon sources. *Reports on Progress in Physics*, 68(5):1129, 2005.

[147] A. Kuhn, M. Hennrich, T. Bondo, and G. Rempe. Controlled generation of single photons from a strongly coupled atom-cavity system. *Applied Physics B*, 69(5):373–377, 1999.

[148] Andris Ambainis and Oded Regev. An elementary proof of the quantum adiabatic theorem. Technical report, 2004.

[149] LA Giannuzzi and FA Stevie. A review of focused ion beam milling techniques for tem specimen preparation. *Micron*, 30(3):197–204, 1999.

[150] Stefan Nußmann, Karim Murr, Markus Hijlkema, Bernhard Weber, Axel Kuhn, and Gerhard Rempe. Vacuum-stimulated cooling of single atoms in three dimensions. *Nature Physics*, 1(2):122–125, 2005.

[151] J Ye, DW Vernooy, and HJ Kimble. Trapping of single atoms in cavity qed. *Physical Review Letters*, 83(24):4987, 1999.

[152] J McKeever, JR Buck, AD Boozer, A Kuzmich, H-C Nägerl, DM Stamper-Kurn, and HJ Kimble. State-insensitive cooling and trapping of single atoms in an optical cavity. *Physical review letters*, 90(13):133602, 2003.

[153] Stefan Nußmann, Markus Hijlkema, Bernhard Weber, Felix Rohde, Gerhard Rempe, and Axel Kuhn. Submicron positioning of single atoms in a microcavity. *Physical review letters*, 95(17):173602, 2005.

[154] Kevin M Fortier, Soo Y Kim, Michael J Gibbons, Peyman Ahmadi, and Michael S Chapman. Deterministic loading of individual atoms to a high-finesse optical cavity. *Physical review letters*, 98(23):233601, 2007.

[155] Mark M Wang, Eugene Tu, Daniel E Raymond, Joon Mo Yang, Haichuan Zhang, Norbert Hagen, Bob Dees, Elinore M Mercer, Anita H Forster, Ilona Kariv, et al. Microfluidic sorting of mammalian cells by optical force switching. *Nature biotechnology*, 23(1):83–87, 2005.

[156] Dr. Gerhard Rempe. personal communication.

[157] Brian Drobot. Tapered air-core bragg waveguide spectrometers for fluorescence detection in lab-on-a-chip devices. Master's thesis, University of Alberta, 6 2014.

[158] C Doolin, PH Kim, BD Hauer, AJR MacDonald, and JP Davis. Multidimensional optomechanical cantilevers for high-frequency force sensing. *New Journal of Physics*, 16(3):035001, 2014.

[159] Matt Eichenfield, Ryan Camacho, Jasper Chan, Kerry J Vahala, and Oskar Painter. A picogram-and nanometre-scale photonic-crystal optomechanical cavity. *Nature*, 459(7246):550–555, 2009.

[160] Ivan Favero and Khaled Karrai. Optomechanics of deformable optical cavities. *Nature Photonics*, 3(4):201–205, 2009.

[161] Fanglu Lu, Forrest G Sedgwick, Vadim Karagodsky, Christopher Chase, and Connie J Chang-Hasnain. Planar high-numerical-aperture low-loss focusing reflectors and lenses using subwavelength high contrast gratings. *Optics express*, 18(12):12606–12614, 2010.

[162] Connie J Chang-Hasnain and Weijian Yang. High-contrast gratings for integrated optoelectronics. *Advances in Optics and Photonics*, 4(3):379–440, 2012.

[163] Vadim Karagodsky and Connie J Chang-Hasnain. Physics of near-wavelength high contrast gratings. *Optics express*, 20(10):10888–10895, 2012.

[164] Xu Chen, Clément Chardin, Kevin Makles, Charles Caër, Sheon Chua, Rémy Braive, Isabelle Robert-Philip, Tristan Briant, Pierre-Francois Cohadon, Antoine Heidmann, et al. High-finesse fabry-perot cavities with bidimensional si _3 n _4 photonic-crystal slabs. *arXiv preprint arXiv:1603.07200*, 2016.

[165] Victor Liu and Shanhui Fan. S^4 : A free electromagnetic solver for layered periodic structures. *Computer Physics Communications*, 183(10):2233 – 2244, 2012.

Appendix A

Silicon Nitride Membrane Devices

A secondary project was the development of a new type of Fabry-Perot cavity consisting of a Bragg reflector and a thin two dimensional photonic crystal mirror. This cavity has two potential advantages over the dome cavities presented in the main body of this thesis. First, high stress silicon nitride membranes have been shown previously to exhibit high quality factor mechanical modes crucial for optomechanics [158, 159]. Secondly, the periodic array of holes in the photonic crystal mirror will provide open access for the delivery of atomic species. However, challenges with atomic trapping, described in Chapter 4, would still exist and need to be solved. This appendix describes the development process of the planar photonic crystal mirror and Fabry-Perot cavity, mainly focused on the simulations but also describing initial fabrication attempts.

A.1 Two-Dimensional Photonic Crystal Mirror

The primary motivation for this work was the development of a Fabry-Perot cavity with a mechanically compliant top mirror. Bragg reflectors like the ones utilized in the main body of this thesis are relatively thick, ~ 2.5 μm for a ten-period mirror. As a result, dome microcavities were found to have poor mechanical resonances,

exhibiting mechanical quality factors of ~ 100 [129]. Also due to the large mass of the mechanical element, the zero point motion is small: an undesirable property for optomechanics [160]. However, the low optical mode volume of the dome microcavities resulted in a high optomechanical coupling rate $g_0 \approx 2\pi \times 30$ kHz (Unfortunately, the nomenclature is identical to that of cavity quantum electrodynamics). Thus augmenting the design to include a lighter, more mechanically compliant top mirror could produce an excellent optomechanical sensing device.

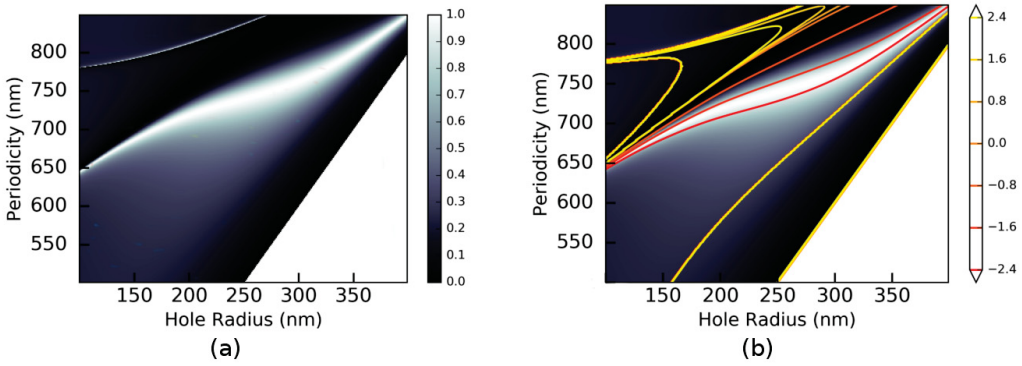

Figure A.1: (a) Simulated reflectance of a 150 nm thick triangular two-dimensional photonic crystal mirror under plane-wave monochromatic 780 nm illumination. The unspecified region in the bottom-right of this plot represents parameters for which the hole diameter is greater than the lattice periodicity, and thus could not be fabricated. (b) Contours of constant phase upon reflection are shown; these contours tends to follow lines of constant reflectance. To develop a focusing mirror the phase upon reflection must be varied as a function of position, while maintaining high reflectance, as described in [161].

The mirror design was originally based on the high contrast grating design described in Ref. [162, 163] for infrared on-chip mirrors. These mirrors operate on the principle of Fano-resonances characterized by the interaction of a continuum state interacting with a discrete set of states. The impinging radiation field sets up a standing wave mode within the planar periodic structure. Fine tuning the mirror parameters allows the standing wave to destructively interfere with the transmitted field, resulting in high reflectivity for normally incident light. As silicon is highly

lossy in the visible, silicon nitride was used as the high index media, and the grating design was replaced with a periodic array of holes as described in Ref. [164].

A triangular lattice of periodic holes was determined to provide the optimal mirror properties, such as high-broadband reflectivity, and features sizes that are straightforward to fabricate. Simulations were performed using rigorous coupled-wave analysis (RCWA), using an open-source language: S4 [165]. Plane-wave monochromatic illumination was assumed, impinging on an infinite periodic array at normal incidence for all simulations performed. Figure A.1a shows the reflectivity of a 150 nm thick silicon nitride photonic crystal mirror as a function of hole radius and periodicity for 780 nm illumination. The regions of high reflection follow smooth curves providing several choices of parameters that would produce a highly reflective membrane. Utilizing this fact, it has been shown that by spatially varying the phase upon reflection, the reflected field may be focused to a point, mimicking a curved surface [161]. The phase upon reflection was again determined using RCWA; lines of constant phase are shown in Figure A.1b. Unfortunately the lines of constant phase follow the lines of constant reflectivity, rendering focusing difficult while maintaining high reflectivity.

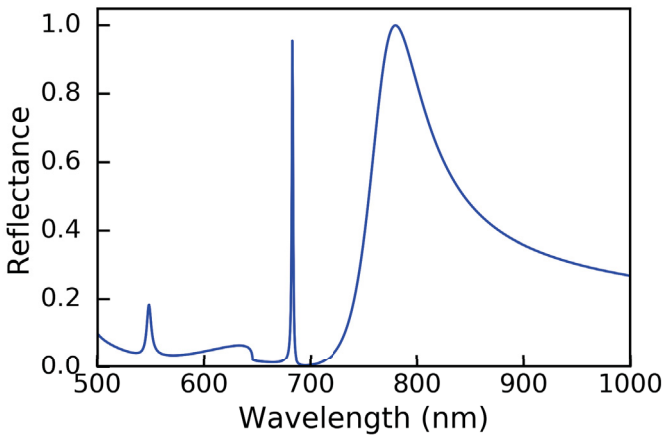

Figure A.2: Simulated reflectance as a function of wavelength for a 150nm thick photonic crystal mirror. The mirror in this simulation was designed with a hole radius of 256 nm and a hole periodicity of 742 nm.

Finally, the previous simulations were performed using a fixed hole pattern. Reflection as a function of wavelength was investigated for a hole radius of 256nm and a hole periodicity of 742 nm, shown in Figure A.2.

A.2 Photonic Crystal Fabry-Perot Cavity

The ultimate goal was to develop an on-chip Fabry-Perot cavity using the two dimensional photonic crystal mirror as the top reflector. Thus the entire structure was simulated to examine the transmission properties as a function of wavelength. The cavity was constructed from a Bragg reflector (similar to those used in the main portion of the thesis), followed by an air gap, and capped off by the photonic crystal mirror. Simulated transmission spectra for several structures with differing numbers of Bragg layers is shown in Figure. A.3. Moreover, it appears as if the quality factor is limited by the reflectivity of the bottom Bragg reflector; however, fabrication error will certainly also play a part, as the top photonic crystal will not be perfectly periodic as it is in these simulations.

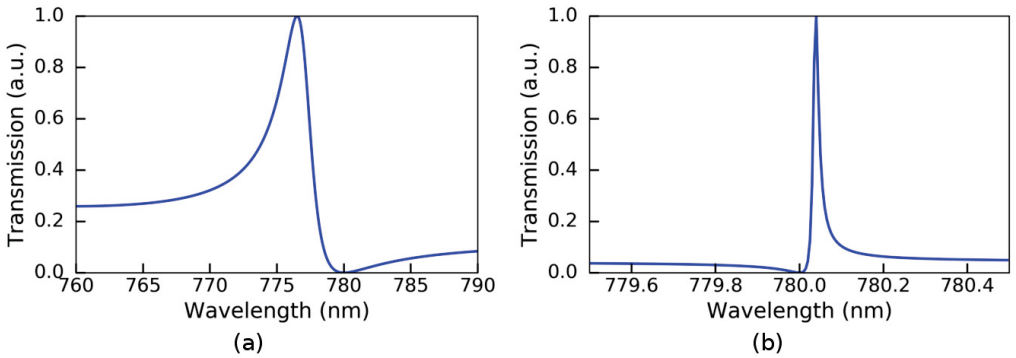

Figure A.3: (a) Simulated transmission spectrum for a Fabry-Perot cavity with an air gap of 1.08 μm and a three-period Bragg reflector. (b) Transmission spectrum for a Fabry-Perot cavity with an air gap of 1.472 μm and a ten period Bragg reflector.

Furthermore, the electric field was simulated, showing a high field intensity located within the photonic crystal mirror, and a standing wave within the Fabry-Perot cavity, as shown in Figure A.4.

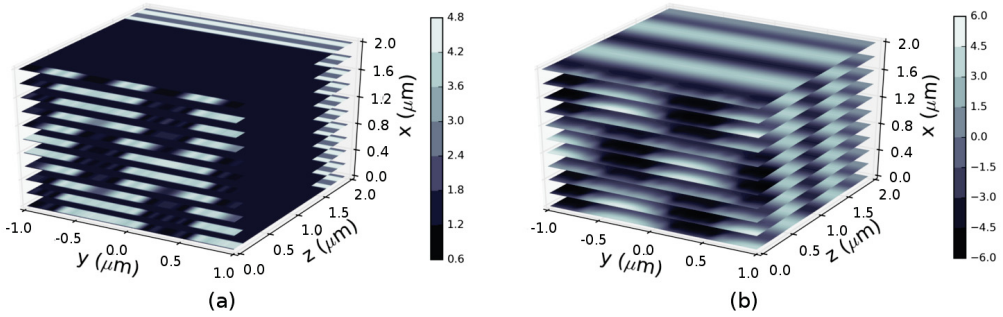

Figure A.4: (a) Dielectric constant distribution of the photonic crystal Fabry-Perot cavity simulation. The photonic crystal mirror is located at $z = 0$ μm, followed by an air gap, the Bragg reflector starts at $z = 1.5$ μm. The non-uniformity in the silicon nitride mirror is a result of the inverse Fourier transform used in the output of the dielectric constant. (b) On resonance electric field (arbitrary units) distribution for the cavity in Figure A.3.

A.3 Fabrication

The fabrication started with the deposition of a Bragg reflector onto a fused silica wafer, identical to the bottom mirror described in Chapter 3. Following this a ~ 4 μm sacrificial silicon layer was deposited, with thickness determined via the simulations described above. Silicon nitride was then deposited using the Trion PECVD located within the Nanofab facility, with a targeted thickness of 150 nm. Unfortunately the silicon nitride layer was not uniform, likely due to charging effects caused by the fused silica substrate, since the test layers deposited on pure silicon substrates exhibited excellent uniformity. As a result, it was difficult to ensure the device layer thickness was correct. The silicon nitride layers deposited in the current PEVCD system exhibit high compressive stress. In order to achieve tensile stress, the wafer was annealed at

500°C for thirty minutes resulting in a tensile stress of ~ 1 GPa. During the annealing process, the Bragg reflector fractured, causing cracking throughout the device layers, likely a result of differential thermal expansion between the thin film layers the silica substrate. A second sample was prepared using a three period Bragg reflector, which was able to survive the annealing process. In future attempts this issue may be avoided by utilizing the new PECVD chamber that is being installed, at the nanofab and which has the capability of modifying the film stress during the deposition.

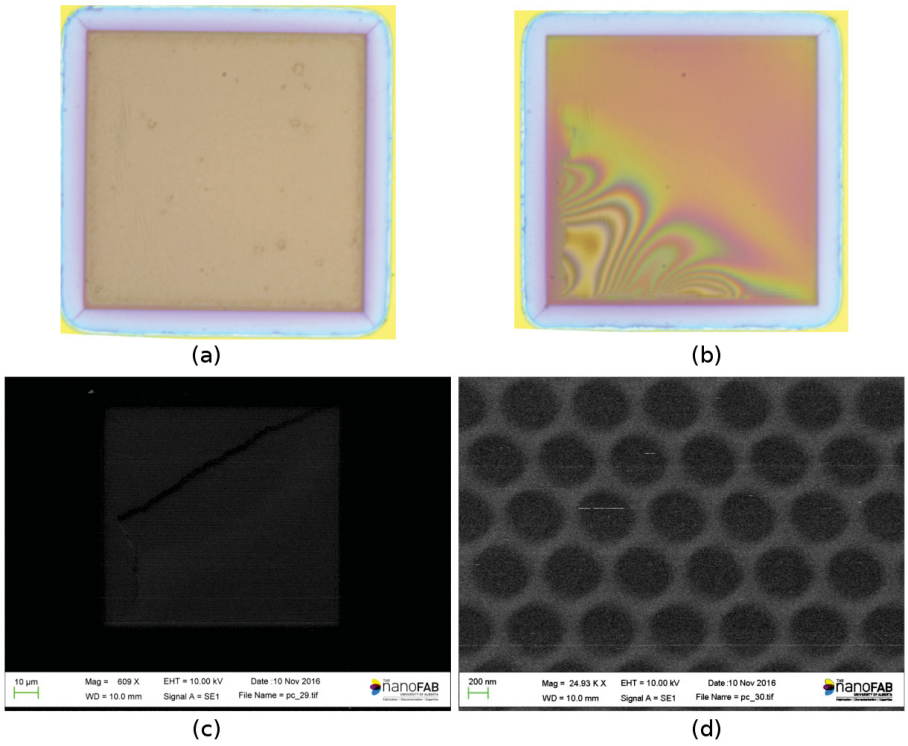

Figure A.5: (a,b) Microscope images of photonic crystal cavities. The photonic crystal in (b) broke and a portion fell resulting in white-light interference between the top mirror and the bottom Bragg reflector. (c,d) SEM micrographs of the photonic crystal cavities, it was determined the hole diameters were larger than designed as a result of the reactive ion etch utilized.

The wafer was diced into 1.0×0.5 mm pieces, the photonic crystal was defined using electron beam lithography, and a 130 second reactive ion etch was used to etch the periodic array of holes into the silicon nitride. The silicon sacrificial layer was removed using five, sixty second gaseous xenon difluoride etch steps, which eliminated

the need for critical point drying, and also has improved selectivity to silicon over the more standard potassium hydroxide wet etch. Several of the cavities are shown in Figure A.5; several of the mirrors cracked, however the ones that did survive appeared red under white light illumination, which is promising as they were designed to be reflective in the red portion of the spectrum.

Finally, transmission scans were performed using the setup described in Chapter 3. A baseline scan was taken on a part of the chip that was not etched in any way, shown in Figure A.6a. A scan through a cavity is shown in Figure A.6b. Note for this scan the focus and laser power were not modified compared with the baseline scan. Also, polarization had little effect on the transmission through the cavity. It can be seen that the net transmission through the cavity is reduced relative to the background scan, this may be a result of the mirror reflectance, however it may also simply be an increase in scattering. It may be instructive to measure the cavities using a broadband white light source to determine the spectrum over a wavelength range greater than that of the tunable laser, however due to time constraints this was left for future work.

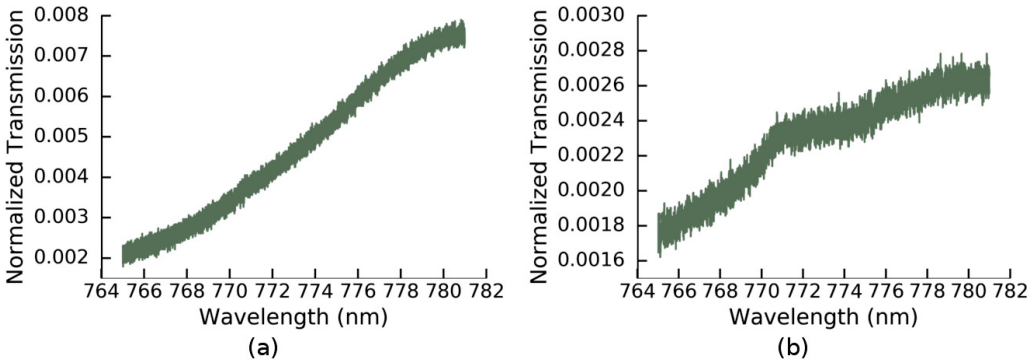

Figure A.6: (a) Background transmission through a portion of the chip not etched. (b) Transmission though one of the photonic crystal cavities, the net power transmitted is decreased compared with the background transmission. This may be a result of increased reflection from the mirror surface, or simply a result of increased scattering. Unfortunately, no resonance behavior was observed.

Appendix B

Substrate Fabry-Perot Resonance

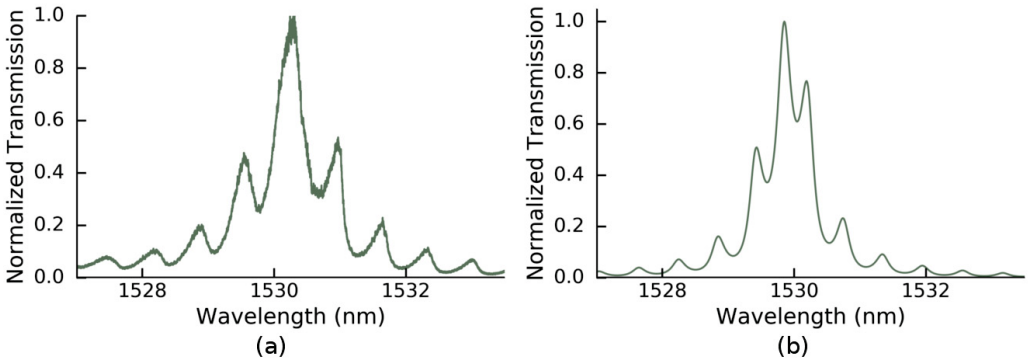

Figure B.1: (a) Transmission spectra for a 200-μm cavity on the chip shown in Figure. 3.16a; a periodic modulation of the cavity transmission is seen along with the Lorentzian resonance. (b) Transfer matrix simulation of this resonance showing a similar behavior of periodic modulation along with the cavity Lorentzian.

The initial cavities produced for the electrical tuning experiments discussed in Section 3.3.1 were fabricated on a doubly polished silicon wafer. As discussed in the main text, these cavities were purposely made with lower reflectance mirrors to produce a broad passband. Initial transmission spectra revealed a secondary modulation in the transmission superimposed on the Lorentzian peak, as shown in Figure B.1a. Previous experiments using higher quality factor cavities observed a periodic flashing while imaging transmission with a camera; however, the transmission spectra obtained did

not produce this secondary modulation [63]. The modulation was determined to be a result of a secondary Fabry-Perot mode within the silicon substrate. Transfer matrix simulations were used to reproduce the experimental results, shown in Figure B.1b. The behavior was not observed in previous cavities, likely since the line-width was much narrower than the free spectral range of the secondary mode.

Appendix C

Source Code

Master Equation simulation used in Section 4.1.1 using the parameters for a 100 μm cavity.

```
%pylab inline
import subprocess
import prettyplotlib as ppl

#Initialize the time step dt.
dt = 1e-13
tau = arange(0,80e-9,dt)
#Generate the Gaussian trigger pulse.
Omega = 2*pi*1.12e9 * exp(-(tau-40e-9)**2/(2*(8e-9)**2))

#Atomic Polarization Decay Rate
gamma = 2*pi*3e6
#Atom-Cavity Coupling Rate
g = 2*pi*1.12e9
#Cavity Decay Rate
kappa = 2*pi*6.7e9
#Initializing the Lindblad operator matrix
Gam = matrix([[0,gamma/2,kappa],[gamma/2,gamma/2,gamma/2 + kappa],[kappa,gamma/2
+ kappa, 2*kappa]])

#Setting the initial condition of the system to be in the ground state —u,0¿
rholast = rho0
rhotot = zeros(((len(tau),3,3)), dtype=complex)
P0 = zeros(len(tau))
P1 = zeros(len(tau))
P2 = zeros(len(tau))
```

```
#Loop that runs the time-evolution of the density matrix operator
for ii,jj in enumerate(tau):
    Hi = -0.5*matrix([[0,Omega[ii],0],[Omega[ii],0,2*g],[0,2*g,0]])
    H = Hi
    Gammarho = multiply(Gam,rholast)
    rhonew = rholast + (-1j*(H*rholast-rholast*H) - Gammarho)*dt
    rhotot[ii][:][:] = rholast
    rhocheck = rholast
    P0[ii] = real(trace(rho0*rholast*rho0))
    P1[ii] = real(trace(rho1*rholast*rho1))
    P2[ii] = real(trace(rho2*rholast*rho2))
    rholast = rhonew

#Calculating the emission rate, assuming  2% scattering loss
Emiss = 1.95*kappa*P2/(1e6)
Emissa = 1.95*kappa*P2

#Calculating the emission probability
Prob = trapz(Emissa,tau)
```

S4 Simulations used in Appendix A, for cavity transmission.

```
S = S4.NewSimulation()
S:SetLattice(0.742,0, 0.371,0.642591)
S:SetNumG(100)
S:AddMaterial("SiN", 4.0,0) – real and imag parts of dielectric constant
S:AddMaterial("SiO2", 2.207,0) – real and imag parts of dielectric constant
S:AddMaterial("Ta2O5", 4.5689,0) – real and imag parts of dielectric constant
S:AddMaterial("Vacuum", 1,0)
S:AddLayer('AirAbove', 0 , 'Vacuum')
S:AddLayer('Slab', 0.150 , 'SiN')
S:SetLayerPatternCircle('Slab', 'Vacuum', 0.5565,0.3212954, 0.256)
S:AddLayer('AirGap', 1.4724, 'Vacuum')
S:AddLayer('OneHigh', 0.089 , 'Ta2O5')
S:AddLayer('OneLow', 0.128 , 'SiO2')
S:AddLayer('TwoHigh', 0.089 , 'Ta2O5')
S:AddLayer('TwoLow', 0.128 , 'SiO2')
S:AddLayer('ThreeHigh', 0.089 , 'Ta2O5')
S:AddLayer('ThreeLow', 0.128 , 'SiO2')
S:AddLayer('FourHigh', 0.089 , 'Ta2O5')
S:AddLayer('FourLow', 0.128 , 'SiO2')
S:AddLayer('FiveHigh', 0.089 , 'Ta2O5')
S:AddLayer('FiveLow', 0.128 , 'SiO2')
S:AddLayer('SixHigh', 0.089 , 'Ta2O5')
```

```
S:AddLayer('SixLow', 0.128 , 'SiO2')
S:AddLayer('SevenHigh', 0.089 , 'Ta2O5')
S:AddLayer('SevenLow', 0.128 , 'SiO2')
S:AddLayer('EightHigh', 0.089 , 'Ta2O5')
S:AddLayer('EightLow', 0.128 , 'SiO2')
S:AddLayer('NineHigh', 0.089 , 'Ta2O5')
S:AddLayer('NineLow', 0.128 , 'SiO2')
S:AddLayer('TenHigh', 0.089 , 'Ta2O5')
S:AddLayer('TenLow', 0.128 , 'SiO2')
S:AddLayer('ElevenHigh', 0.089 , 'Ta2O5')
S:AddLayer('Substrate', 0 , 'SiO2')
–S:AddLayerCopy('AirBelow', 0, 'AirAbove')
S:SetExcitationPlanewave(
    0,0, – incidence angles
    1,0, – s-polarization amplitude and phase (in degrees)
    0,0) – p-polarization amplitude and phase
–S:UsePolarizationDecomposition()
for lam=0.7795,0.7805,0.000005 do
    freq = 1/lam
    S:SetFrequency(freq)
    forward,backward = S:GetPoyntingFlux('AirAbove', 0)
    forward = S:GetPoyntingFlux('Substrate', 0)
    print (lam .. '' .. forward .. '' .. backward)
    io.stdout:flush()
end
```

S4 Simulations used in Appendix A, for cavity electric field distribution.

```
S = S4.NewSimulation()
S:SetLattice(0.742,0, 0.371,0.642591)
S:SetNumG(100)
S:AddMaterial("SiN", 4.0,0) – real and imag parts of dielectric constant
S:AddMaterial("SiO2", 2.207,0) – real and imag parts of dielectric constant
S:AddMaterial("Ta2O5", 4.5689,0) – real and imag parts of dielectric constant
S:AddMaterial("Vacuum", 1,0)
S:AddLayer('AirAbove', 0 , 'Vacuum')
S:AddLayer('Slab', 0.150 , 'SiN')
S:SetLayerPatternCircle('Slab', 'Vacuum', 0.5565,0.3212954, 0.256)
S:AddLayer('AirGap', 1.4724, 'Vacuum')
S:AddLayer('OneHigh', 0.089 , 'Ta2O5')
S:AddLayer('OneLow', 0.128 , 'SiO2')
S:AddLayer('TwoHigh', 0.089 , 'Ta2O5')
S:AddLayer('TwoLow', 0.128 , 'SiO2')
```

```
S:AddLayer('ThreeHigh', 0.089 , 'Ta2O5')
S:AddLayer('ThreeLow', 0.128 , 'SiO2')
S:AddLayer('FourHigh', 0.089 , 'Ta2O5')
S:AddLayer('FourLow', 0.128 , 'SiO2')
S:AddLayer('FiveHigh', 0.089 , 'Ta2O5')
S:AddLayer('FiveLow', 0.128 , 'SiO2')
S:AddLayer('SixHigh', 0.089 , 'Ta2O5')
S:AddLayer('SixLow', 0.128 , 'SiO2')
S:AddLayer('SevenHigh', 0.089 , 'Ta2O5')
S:AddLayer('SevenLow', 0.128 , 'SiO2')
S:AddLayer('EightHigh', 0.089 , 'Ta2O5')
S:AddLayer('EightLow', 0.128 , 'SiO2')
S:AddLayer('NineHigh', 0.089 , 'Ta2O5')
S:AddLayer('NineLow', 0.128 , 'SiO2')
S:AddLayer('TenHigh', 0.089 , 'Ta2O5')
S:AddLayer('TenLow', 0.128 , 'SiO2')
S:AddLayer('ElevenHigh', 0.089 , 'Ta2O5')
S:AddLayer('Substrate', 0 , 'SiO2')
–S:AddLayerCopy('AirBelow', 0, 'AirAbove')
S:SetExcitationPlanewave( 0,0, – incidence angles 1,0, – s-polarization amplitude and
phase (in degrees) 0,0) – p-polarization amplitude and phase
–S:UsePolarizationDecomposition()
lam = 0.780039
freq = 1/lam
S:SetFrequency(freq)
    for x=-1.0,1.0,0.02 do
    for y=-1.0,1.0,0.02 do
    for z = 0.0,2.0,0.02 do
    Exr, Eyr, Ezr, Exi, Eyi, Ezi = S:GetEField(x, y, z)
    er,ei = S:GetEpsilon(x,y,z)
    print (x .. '\t' .. y .. '\t' .. z .. '\t' .. Exr .. '\t' .. Exi .. '\t' .. Eyr .. '\t' .. Eyi
    .. '\t' .. Ezr .. '\t' .. Ezi .. '\t' .. er .. '\t' .. ei)
    io.stdout:flush()
    end
    end
end
```